THE ROLE OF THE N-END RULE PATHWAY IN MAMMALIAN DEVELOPMENT AND INNATE IMMUNITY

by

Sung Tae Kim

Bachelor of Science, Seoul National University, 2003

Master of Medical Science, Yonsei University, 2005

Submitted to the Graduate Faculty of

School of Pharmacy in partial fulfillment

of the requirements for the degree of

Doctor of Philosophy in Pharmaceutical Sciences

University of Pittsburgh

2018

UNIVERSITY OF PITTSBURGH

SCHOOL OF PHARMACY

This dissertation was presented

by

Sung Tae Kim

It was defended on

July 23, 2018

and approved by

Yong J. Lee, Ph.D., Professor, Surgery, School of Medicine

Song Li, M.D., Ph.D., Professor, Pharmaceutical Sciences

Yong Wan, Ph.D., Professor, Reproductive Science in Medicine and Pharmacology, Feinberg School of Medicine, Northwestern University

Xiang-Qun (Sean) Xie, M.D., Ph.D., EMBA, Professor, Pharmaceutical Sciences

Dissertation Advisor: **Yong Tae Kwon**, Ph.D., Professor, Biomedical Sciences, College of Medicine, Seoul National University

THE ROLE OF THE N-END RULE PATHWAY IN MAMMALIAN DEVELOPMENT AND INNATE IMMUNITY

Sung Tae Kim, PhD

University of Pittsburgh, 2018

The N-end rule pathway is a proteolytic system in which single N-terminal amino acids of proteins act as a class of degrons (N-degrons) that determine the half-lives of proteins. We have previously identified a family of mammals N-recognins whose conserved UBR boxes bind N-degrons to facilitate substrate ubiquitination, leading to proteolysis via the ubiquitin proteasome system or autophagy. Amongst these N-recognins, UBR4 binds to both type-1 and type-2 residues without known ubiquitylation domain. N-terminal Arg is one of the principal degrons that it can be generated through post-translational conjugation of L-Arg from Arg-tRNA^{Arg} to N-terminal Asp or Glu, which is mediated by *ATE1*-encoded Arg-tRNA transferases. In this dissertation study, we addressed the roles of UBR4 in mammalian development and ATE1 in innate immune response, respectively.

First, we generated UBR4-deficient mice in which the UBR box of *UBR4* was deleted and characterized the null phenotypes. UBR4-deficient mice exhibit severe embryonic lethality and pleiotropic abnormalities, including accumulated autophagic vacuoles in the yolk sac endoderm. UBR4 also modulates early endosomal maturation and the trafficking through the interaction with Ca^{2+}-bound calmodulin. *UBR4*$^{-/-}$ embryos have multiple developmental defects including neurogenesis and cardiovascular system, which is at least in part attributed to the impairment in cell adhesion and depletion of cell surface proteins. Collectively, these data reveal that the N-recognin UBR4 plays important roles in multiple developmental processes associated with angiogenesis, neurogenesis and cardiovascular system. The developmental processes are most

commonly involved in non-proteolytic processes such as endosomal maturation, trafficking and cellular adhesion.

We show that cytosolic foreign DNA induces N-terminal arginylation of ER chaperons, which is required for host defense system for IFN-β mediated gene induction and IRF3 phosphorylation. Cytosolic dsDNA facilitates relocation of ATE1 to the ER, on which ATE1 is colocalized with STING. Interference of Nt-arginylation that is important for host defense induces the production of virion. Our results suggest that N-terminal arginylation is essential for cellular immune response against foreign DNA and viral infections.

This work provides meaningful evidences demonstrating that the N-end rule pathway plays a pivotal role in mammalian development and innate immunity beside proteolytic function.

TABLE OF CONTENTS

LIST OF TABLES

LIST OF FIGURES

PREFACE

Dedicated to my deceased parents, Jong Taek Kim and Keum Soon Kim. At this moment, I miss you so much. My sisters Ms. Sun mee and Ju mee deserve heartfelt gratitude for their sacrifice and supports for me. I also want to thank my beloved wife So Yeon Kim and cute daughter Claire Jiwoo Kim.

I would like to express my deep gratitude to my mentor and advisor, Dr. Yong Tae Kwon, whom I have had a great opportunity to work with. Since 2009, his faithful support allows me to pursue my research interest and finish this long journey. He is a strong role model through his tireless passion for research and mentoring students. It was also my great experience to know and work with so many people in the Dr. Kwon's lab.

I would also like to thank to my committee including Drs. Yong J. Lee, Song Li, Yong Wan, and Xiang-Qun Xie for their guidance and constructive advises during the doctoral training.

Lastly, please accept my sincere appreciation for fellows, staffs, faculties, and students in the Center of Pharmacogenetics and School of Pharmacy.

ABBREVIATIONS

Ala:	alanine
ANOVA:	analysis of variance
Arg:	arginine
ATE1:	arginyl-tRNA protein transferase 1
BiP:	binding immunoglobulin protein
BSA:	bovine serum albumin
CRT:	calreticulin
Cys:	cysteine
EE:	early endosome
EEA1:	early endosome antigen 1
EGF:	epidermal growth factor
EGFR:	epidermal growth factor receptor
Ed:	visceral endoderm
ER:	endoplasmic reticulum
ERGIC:	ER-Golgi intermediate compartment;
EV:	endocytic vesicle
GAPDH:	glyceraldehyde 3-phosphate dehydrogenase

Golgi:	Golgi apparatus
His:	histidine
HRP:	horseradish peroxidase
Ile:	isoleucine
INF:	interferon
IP:	immunoprecipitation
IRF3:	interferon regulatory factor 3
LC3:	microtubule-associated protein 1 light chain 3
LE:	late endosome
Leu:	leucine
LIR:	LC3-interacting region
Lys:	lysine
Md:	extraembryonic mesoderm
MEF:	mouse embryonic fibroblast
Met:	methionine
MVB:	multivesicular body
Nt-Arg:	N-terminal residue arginine
Nt-Asn:	N-terminal residue asparagine
Nt-Cys:	N-terminal residue cysteine
Nt-Gln:	N-terminal residue glutamine
Nt-Met:	N-terminal residue methionine
PBS:	phosphate-buffered saline solution
PDI:	protein disulfide isomerase

PFA:	paraformaldehyde
Phe:	phenylalanine
PI3P:	phosphatidylinositol 3-phosphate
Poly(dA:dT):	poly(deoxyadenylic-deoxythymidylic) acid sodium salt
PTM:	post-translational modifications
RAB5:	ras-related protein 5
RAB7:	ras-related protein 7
R-BiP:	arginylated BiP
SDS-PAGE:	sodium dodecyl sulfate polyacrylamide gel electrophoresis
siRNA:	small interfering RNA
STING:	stimulator of interferon genes
TBK1:	TANK-binding kinase 1
TUNEL:	terminal deoxynucleotidyl transferase dUTP nick end labeling
Trp:	tryptophan
Tyr:	tyrosine
Ub:	ubiquitin
UBA:	Ub associated domain
UPS:	ubiquitin proteasome system
YS:	yolk sac

1.0 INTRODUCTION AND BACKGROUND

1.1 THE N-END RULE PATHWAY

A substantial fraction of newly synthesized proteins (30%) is continuously being degraded to amino acids within minutes of synthesis [1]. Enough capacity to degrade non-functional, damaged, or toxic proteins is vital for cell survival and maintaining homeostasis. To ensure the rapid turnover and degradation, cells remain the remarkably high abundance of proteasome (constituting 1% of total cellular protein). In addition, approximately 600 genes encoding proteases or protease-like proteins have been identified in human, and proteases are estimated to comprise 1.7% of the human genome, which is one of the largest human enzyme families [2]. Many polypeptides expose new N-terminal residues during their life cycles through proteolytic cleavages, yet their functions and mechanisms have received little attention in various biological fields relative to internal residues. Recent studies reveal an emerging role of the protein N-termini in proteolysis. The relationship between the identity of the proteins N-termini and their half-life is defined by a rule, called the N-end rule [3, 4].

In mammals, the substrates of N-recognins include positively charged (Arg, Lys, and His; type 1) and bulky hydrophobic (Phe, Tyr, Trp, Leu, and Ile; type-2) residues (Figure 1A) [5-8]. They can be exposed when polypeptides are cleaved at the N-terminal Met (Nt-Met) residue by Met amino peptidases or at the internal residues by endopeptidases, such as caspases, separases, and signal peptide peptidases [9, 10]. N-terminal Arg (Nt-Arg) is one of the principal degrons that can be conditionally generated through post-translational conjugation of L-Arg from Arg-tRNA^{Arg} to Nt-Asp or Nt-Glu. This tRNA-dependent post-translational modification (PTM) is mediated by

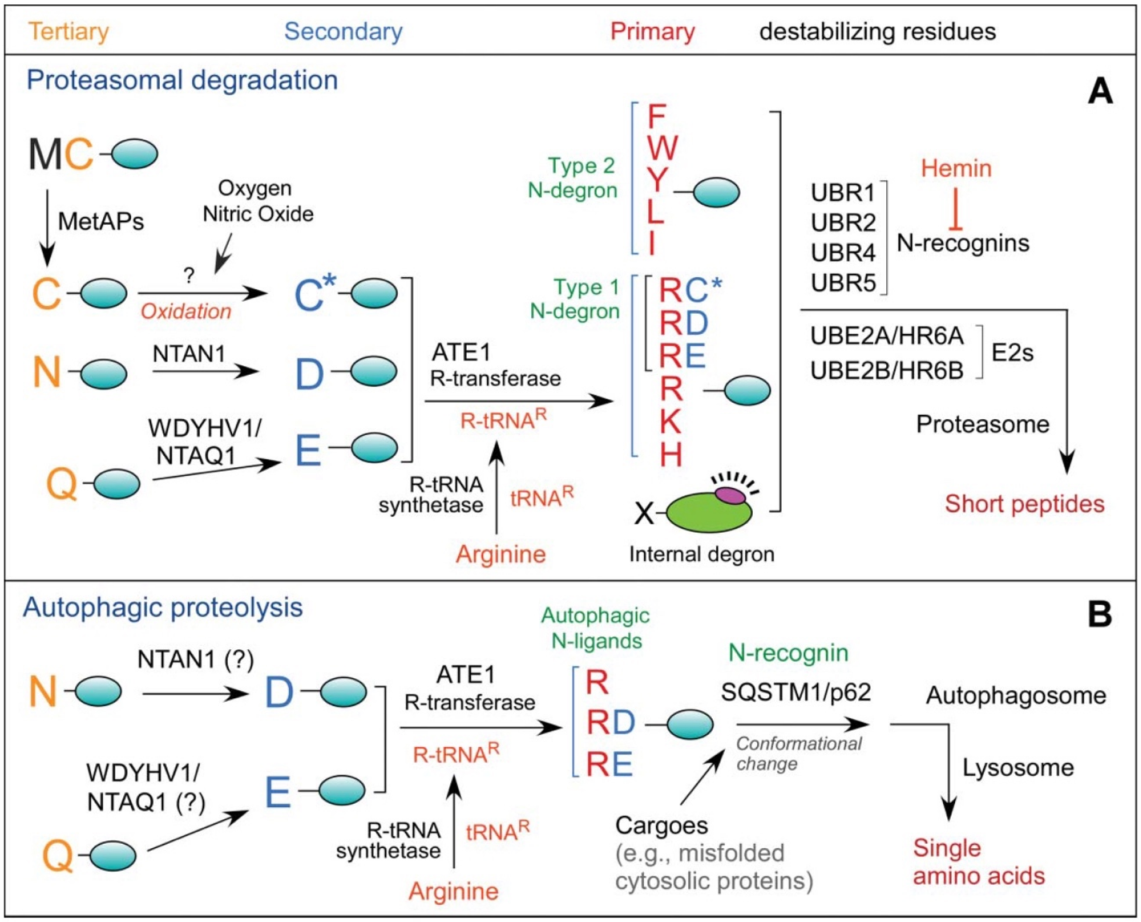

Figure 1: The mammalian N-end rule pathway in the UPS and autophagy.

(A) In the UPS, the tertiary destabilizing Nt-Asn and Gln are deamidated by two distinct enzymes, NTAN1 and WDYHV1/NTAQ1 into Asp and Glu, respectively. The secondary destabilizing N-terminal residues Asp and Glu are arginylated by ATE1 R-transferase isoforms produced through alternative splicing of ATE1. The destabilizing activity of Nt-Cys requires its oxidation prior to arginylation by ATE1. C* denotes the oxidized Nt-Cys residue, either Cys-sulfinic acid [$CysO_2(H)$] or Cys-sulfonic acid [$CysO_3(H)$]. Nt-Arg together with other type 1 and type 2 residues are directly bound by a set of N-recognins characterized by the UBR box, including UBR1, UBR2, UBR4, and UBR5. UBR box proteins can target substrates through the recognition of internal degrons as well as N-degrons (B) In autophagic proteolysis, the formation of cytosolic misfolded proteins triggers Nt-arginylation and cytosolic relocalization of ER-residing chaperones including BiP and PDI. Among Nt-arginylated ER proteins, R-BiP binds to the autophagic receptor p62 and is degraded through lysosomal degradation. In this proteolytic system, Nt-Arg acts as a cis-acting degron for Nt-arginylated proteins themselves and a trans-acting degron for associated cargoes, such as cytosolic misfolded proteins [11].

ATE1-encoded Arg-tRNA transferases (R-transferases; EC 2.3.2) [12-15]. The arginylation-permissive Nt-Asp and Nt-Glu residues can be exposed by endoproteolytic cleavage or newly generated through deamidation of Nt-Asn and Nt-Gln by the amidases NTAN1 and NTAQ1, respectively [16]. In the mammalian N-end rule pathway, Nt-Cys is oxidized into Cys-sulfinic acid ($CysO_2(H)$) or Cys-sulfonic acid ($CysO_3(H)$), which is arginylated to generate Nt-Arg [12, 15]. In addition to the classical N-end rule pathway, Nt-Met and acetylated N-terminal residues, found at 80% of human proteins, can also function as N-degrons, resulting proteolysis through the N-end rule pathway [17, 18].

In the N-end rule proteolytic pathway, single N-terminal amino acids can modulate proteins' half-lives through their recognition and binding by specific recognition components, called N-recognins [4, 19]. In eukaryotic cells, these N-recognins induce proteolysis through the recognition of specific N-terminal amino acids that function as degradation determinant (N-degrons). Rare examples of N-recognins, which can bind proteolysis-inducing N-terminal residues, include a family of UBR box-containing proteins (e.g., UBR1, UBR2, UBR4, and UBR5) and the autophagic adaptor p62/SQSTM-1/Sequestosome-1 (Figure 1B) [4, 20]. Following the recognition by N-recognins, N-terminal amino acids can act as *cis*-degrons that induce proteolysis of substrates themselves (Figure 1A). If substrates (e.g., chaperones) are associated with cargoes (e.g., misfolded proteins), the same degron can induce proteolysis of protein complexes or aggregates in a *trans*-mode (Figure 1B) [11, 20]. In principle, N-degrons can induce the degradation of non-proteolytic materials, such as endosomes and other membraneneous constituents, if the degrons are exposed on the surface of such subcellular structures.

1.2 MODULATION OF AUTOPHAGY BY THE N-TERMINAL ARGINYLATION

In eukaryotes, *ATE1*-encoded Arg-tRNA transferases (R-transferases; EC 2.3.2) transfer L-arginine (L-Arg) of Arg-tRNA^{Arg} to the N-terminal Asp (Nt-Asp) and Glu (Nt-Glu) of substrates including misfolded proteins and endoplasmic reticulum (ER)-residing chaperones [14, 20, 21]. Additionally, the Nt-Arg can be generated by endoproteolytic cleavages or enzymatically through the modification of Nt-Asn, Nt-Gln, Nt-Cys, Nt-Asp, and Nt-Glu [10]. The resulting N-terminal Arg (Nt-Arg) residue is recognized by N-recognins like UBR1, UBR2, UBR4/p600, UBR5/EDD, and p62/SQSTM1/Sequestosome-1, acting as a bimodal degradational signal to either (UPS) or macroautophagy (hereafter referred to as autophagy; Figure 1) [8, 9, 20]. Among numerous substrates, we found that various cellular stresses facilitate relocation of ER-residing proteins or nuclear proteins to the cytoplasm and induce their Nt-arginylation by ATE1 [9, 20]. The Nt-arginylation of ER chaperones like binding-immunoglobulin protein (BiP/GRP78/HSPA5), calreticulin/CRT/CALR, and protein disulfide isomerase (PDI) is induced by cytosolic double-stranded DNA (dsDNA), a strong activator of the innate immune response [20]. The dsDNA-mediated immune response promotes the accumulation of Nt-arginylated of BiP (R-BiP) in the cytosol, which binds the selective autophagy receptor p62 through its binding of the ZZ domain of p62, resulting its self-oligomerization [20]. However, the physiological meanings of Nt-arginylation of BiP and the induced interaction of R-BiP with SQSTM1 in the innate immune system are poorly defined.

Among numerous substrates, we found that various cellular stresses facilitate relocation of ER-residing proteins or nuclear proteins to the cytoplasm and induce their Nt-arginylation by

ATE1 [9, 20]. When misfolded cytosolic substrates excessively accumulate beyond the UPS's capacity or under unresolvable ER stress conditions, Ub-conjugated cargoes are redirected to macroautophagy and segregated by autophagosomes for lysosomal degradation [20, 22]. The accumulated cargoes, such as misfolded proteins, signals to ATE1-dependent N-terminal arginylation of endoplasmic reticulum (ER)-residing molecular chaperones including BiP/GRP78, calreticulin/CRT/CALR, and PDI [20]. Nt-arginylated ER proteins relocate to the cytosol where they get associated with cytosolic misfolded proteins and bind the N-recognin p62 through the specific interaction of their N-terminal Arg with p62 ZZ domain [20]. Upon binding, N-terminal Arg acts as an activating ligand that induces p62 self-oligomerization and interaction with LC3 on the surface of autophagosomal membranes, facilitating autophagic degradation for aggregated proteins. Under the specific cellular conditions including aggregated misfolded proteins, ER stress, proteasomal inhibition, and cytosolic double-stranded DNA (dsDNA) exposure, Nt-arginylation by ATE1 can contributes to reprograming global proteolytic flux to relieve cellular stress via autophagic degradation.

1.3 THE NONCANONICAL N-RECOGNIN UBR4

N-recognins directly bind to N-terminal destabilizing residues of substrates and induce polyubiquitination and subsequent degradation of the substrates through the 26S proteasome complex [5, 7]. We have shown that four mammalian proteins, UBR1, UBR2, UBR4/p600, and UBR5/EDD, can bind type-1 or type-2 destabilizing N-terminal residues (Figure 2) [5, 6, 8]. These N-recognins share the UBR box, which is a ~70-residue zinc finger domain that acts as a substrate recognition domain, to bind type-1 residues, including Nt-Arg [23]. The canonical N-recognins

UBR1 and UBR2 also contain the N-domain as type-2 binding site and have been characterized in various mammalian processes. However, the non-canonical N-recognin UBR4 can bind to both type 1 and type 2 residues with no known ubiquitylation domain. While the function and mechanism of the noncanonical N-recognins UBR4 in the N-end rule pathway remains poorly understood, studies by us and others have shown that the cooperative activities of N-recognins mediate the selective proteolysis of cytosolic short-lived proteins, including RGS4 and caspase-generated C-terminal fragments exposing N-terminal degrons (Sriram et al., 2011; Tasaki et al., 2012).

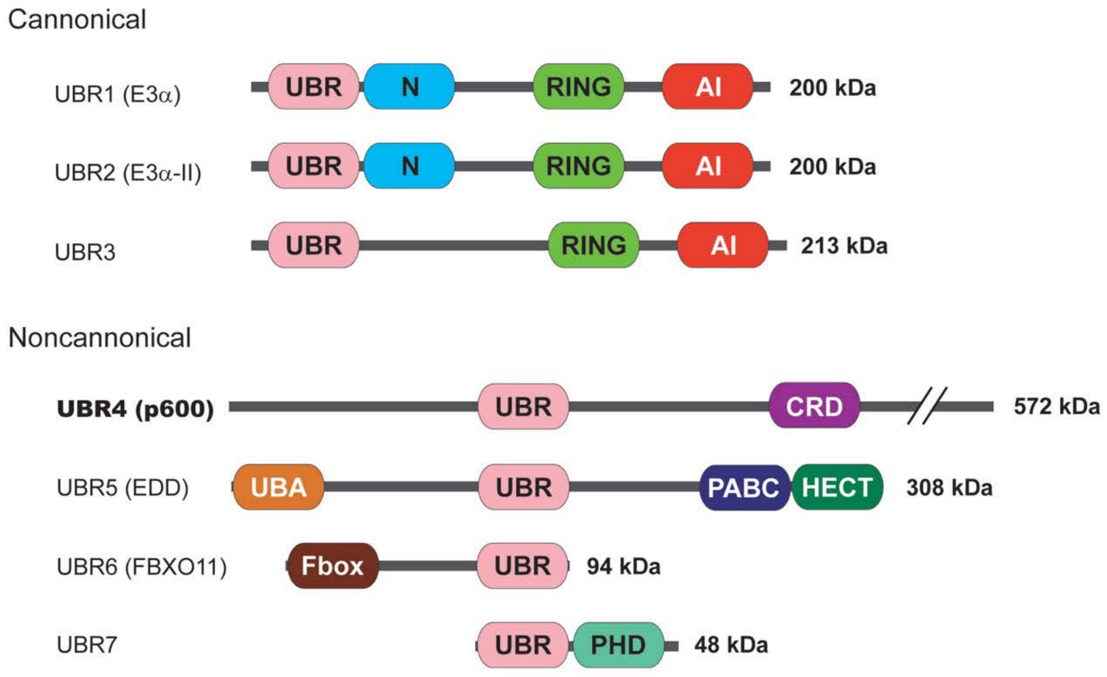

Figure 2: The UBR box N-recognin family of the mammalian N-end rule pathway.

AI, autoinhibitory domain; CRD, cysteine-rich domain; Fbox, F-box; HECT, homologous to the E6-AP carboxyl terminus; N, N-domain; PABC, poly(A) binding protein C-terminal domain; PHD, plant homeodomain finger; RING, RING finger; UBA, ubiquitin association domain; UBR, UBR box [24].

Human UBR4 is a microtubule-associated protein with a size of 570 kDa [8, 24-26]. Beside its huge size, UBR4 is abundant and one of top 15% in human whole organism [27]. UBR4 is ubiquitously expressed in all tissues at variable levels, but analysis of human brain cDNA libraries identified UBR4 as a putative large protein enriched in the central nervous system [28]. In addition, UBR4 is a major protein and candidate protein marker for microvesicles and ecotosomes [29, 30]. UBR4 promotes ubiquitination of ATP-citrate lyase (ACLY), a key regulator of fatty acid biogenesis, suggesting that UBR4 has a role in tumor progression and lipid synthesis [31].

In neuronal system, UBR4 is a marker whose mRNA and protein levels are strikingly decreased in the synaptic regions of neurodegenerative brains in mice, sheep, and *Drosophila melanogaster* [32, 33]. The mutations in human UBR4 has been correlated to early-onset dementia as well as developmental regression, brain atrophy, and ataxia [34]. UBR4 is required for optimal degradation of a model N-end rule substrate as well as ubiquitination of huntingtin (HTT) proteins such as 73 poly-glutamine repeat-bearing mutant HTT (73Q-HTT) and 175Q-HTT [35]. UBR4 and UBR5 are key regulators that synthesize K11/K48-branched heterotypic ubiquitin chains, which are induced and destined for proteasomal degradation during proteotoxic stress [35].

The host UBR4 is essential for replication and pathogenesis of various viruses. UBR4 is required for influenza A virus budding and viral infection through its association with the viral M2 protein, which promotes apical transport of viral proteins [36]. UBR4-M2 interaction initiates in the ER and the UBR4-M2 complex moves to the plasma membrane at the late stages of infection. UBR4-loss disrupts that the apical (from the perinuclear ER to the plasma membrane) transport of viral progenies during the last stage of infection as well as the affection of neighboring cells during the pathogenesis [36]. UBR4 is required for dengue virus and Zika virus infection and replication through its binding to nonstructural protein 5 (NS5) viral protein, which inhibits IFN-I signaling via IFN-regulated transcriptional activator STAT2 (signal transducer and activator of transcription 2) degradation [37, 38]. In addition, the interaction between UBR4 and viral protein E7 is highly conserved across 17 human papillomavirus types (HPV) including HPV-16, 6b, and 11 as well as bovine papillomavirus. It regulates E7-mediated cellular immortalization and transformation activities [39-42]. The UBR4 interaction with HPV E7 is required for the proteasomal degradation of PTPN14 (protein tyrosine phosphatase non-receptor Type 14), a tyrosine phosphatase and tumor suppressor protein [43, 44].

UBR4 regulates homeostasis of podocin/MEC-2 and its multimeric complex, which is a PHB-domain protein and constructs the renal filtration barrier, through helping its ubiquitination at the residues K301 and K307 [45]. UBR4 is a component of a triple E2-E3 complex with a E2 conjugating enzyme RAD6 (Radiation sensitivity protein 6) and a E3 ligase KCMF1 (potassium channel modulatory factor 1). Disruption of the complex leads to misregulation of late endosomal-lysosomal vesicle trafficking and can be related with a downregulated neuronal development in X-linked intellectual disability (XLID) patients [46]. Calossin/Pushover, the *D. melanogaster* of UBR4 orthology, plays a role in synaptic transmission in photoreceptor cells and perineurial glial growth [47, 48]. It plays a role in cell proliferation and differentiation through regulating MAPK for proteasomal degradation in RAS-MAPK signaling [49]. Consistently, UBR4 has been implicated in cell adhesion and integrin-mediated processes, including the formation of ruffled membranes and apoptotic regulation [50]. In *Arabidopsis*, UBR4/BIG has been shown to mediate the vesicular transport of auxin, a master hormone [51].

Overall, these results suggest that UBR4 plays an important role in various biological processes, including protein degradation, viral infection, axonal integrity, neurodegeneration, and synaptic plasticity.

1.4 DISSERTATION OUTLINE

The contents of the dissertation included:

Chapter I. Introduction is a brief description of the research background about the N-end rule pathway, the autophagic modulation by N-terminal arginylation, and the N-recognin UBR4.

Chapter II. The Role of UBR4 in Autophagic Modulation in the Yolk Sac is a full research paper that contains the research background, materials, methods, experimental results, discussion, and conclusion. It suggests that UBR4 plays an important role in mammalian development, in part through regulation of bulk degradation by lysosomal hydrolases in the YS.

Chapter III. The Role of the N-recognin UBR4 in the Biogenesis of the Early Endosome is a full research paper that contains the research background, materials, methods, experimental results, discussion, and conclusion. It shows that UBR4 modulates endosome maturation and the trafficking and proteolysis of internalized cargoes.

Chapter IV. The Function of UBR4 in Neurogenesis and Plasma Membrane Proteins is a full research paper that contains the research background, materials, methods, experimental results, discussion, and conclusion. It proposes that UBR4 plays a role in neurogenesis and the homeostasis of cell surface proteins as well as cell adhesion molecules.

Chapter V. The Function of N-terminal Arginylation by ATE1 in Innate Immunity is a full research paper that contains the research background, materials, methods, experimental results, discussion, and conclusion. It suggests that ATE1-mediated Nt-arginylation is essential for sustain innate immunity against foreign DNA and viral infections.

2.0 THE ROLE OF UBR4 IN AUTOPHAGIC MODULATION IN THE YOLK SAC

[Kim ST, Tasaki T, Zakrzewska A, Yoo YD, Sung KS, Kim S-H et al., The N-end rule proteolytic system in autophagy. Autophagy. 9(7): 1100-3. Jul 2013.]

[Tasaki T*, Kim ST*, Zakrzewska A, Lee BE, Kang MJ, Yoo YD et al., UBR box N-recognin-4 (UBR4), and N-recognin of the N-end rule pathway, and its role in yolk sac vascular development and autophagy. Proc Natl Acad Scri USA. 110(10): 3800-5. Mar 2013. *co-first author]

2.1 RESEARCH BACKGROUND

Substrates of the classical N-end rule pathway include cytosolic short-lived proteins carrying type-1 (Arg, Lys, and His; positively charged) and type-2 (Phe, Tyr, Trp, Leu, and Ile; bulky hydrophobic) N-degrons [5-8]. In addition, N-terminal Met excision or proteolytic cleavage can also expose N-degrons. Among these N-degrons, the principal degron Arg can also be generated through post-translational arginylation of Nt-Asp and Nt-Glu by ATE1 R-transferases [12-15]. In addition, deamidation of the secondary pro-N-degrons Asn and Glu by NTAN1 and NTAQ1 can generate the arginylation-permissive pro-N-degrons Asp and Glu [16]. In addition to type-1 and type-2 N-degrons, Nt-Met and acetylated N-terminal residues, can act as N-degrons [17, 18]. The cellular functions of the N-end rule pathway in degradation of short-lived proteins carrying N-degrons have been characterized in various processes [4, 10].

Our previous studies identified the mammalian N-recognin family consisting of UBR1, UBR2, UBR4/p600, and UBR5, which share the UBR box, a ~70 residue-zinc finger domain that acts as a substrate recognition domain [5, 6, 8, 23]. While the canonical N-recognins UBR1 and UBR2 have been characterized in various mammalian processes, the physiological functions of the noncanonical N-recognins UBR4 in the N-end rule pathway remain unclear. Unlike the other canonical N-recognins, UBR4 does not contain a known ubiquitylation domain [8]. Thus, we can expect that the action mechanism of UBR4 in the N-end rule pathway could be different from those of canonical N-recognins.

Autophagy mediates bulk lysosomal degradation of cytoplasmic constituents such as proteins and damaged cellular organelles. Various cellular stresses including amino acid starvation induce autophagy to promote lysosomal digestion of non-essential cellular materials, providing amino acids and maintaining essential cellular processes[52]. Autophagic cargoes are sequestered and delivered into double-membrane vesicles (autophagosomes) whose fusion with lysosomes, generating autolysosomes wherein the content is degraded by lysosomal hydrolases[53]. The formation of autophagosomes involves ATG12 recruitment to phagophores, which is conjugated to its substrate, ATG5. The ATG5-ATG12-ATG16L1 complex promotes ligation of the ubiquitin-like protein LC3-I with phospholipid phosphatidylethanolamine (PE) to generate LC3-II whose PE moiety is anchored to phagophore membranes[53, 54].

During early embryogenesis, yolk sac (YS) is a major supplier of amino acids for embryonic survival (till ~E9.5 in mice) and that these amino acids are generated through lysosomal digestion of endocytosed maternal lipids and proteins in YS endoderm [55, 56]. As illustrated in Figure 3, YS can be divided into two developmentally distinct layers. The inner mesodermal layer is a circulation organ in which vitelline vessels are developed through intercellular signaling of endothelial cells with vascular smooth muscle cells (SMCs) and surrounding mesenchymal cells. The outer endodermal layer contains a specialized proteolytic system for degradation of extracellular maternal proteins and lipids, which are internalized *via* endocytosis (Figure 3) [57]. Cargo-loaded endosomal vesicles are fused with autophagosomes which are finally digested by hydrolases of lysosomal vacuoles of the YS endoderm. The resulting lysosome-derived amino acids are essential for protein translation during vascular development and embryonic survival at early embryonic developmental stage. At E9.5, the embryo relies on lysosome-generated amino acids from the YS endoderm, because the placenta is not functional at this stage. Therefore, the YS endoderm has a tissue-specific autophagic system that mediates constitutive degradation of extracellular maternal proteins as a major type of cargoes.

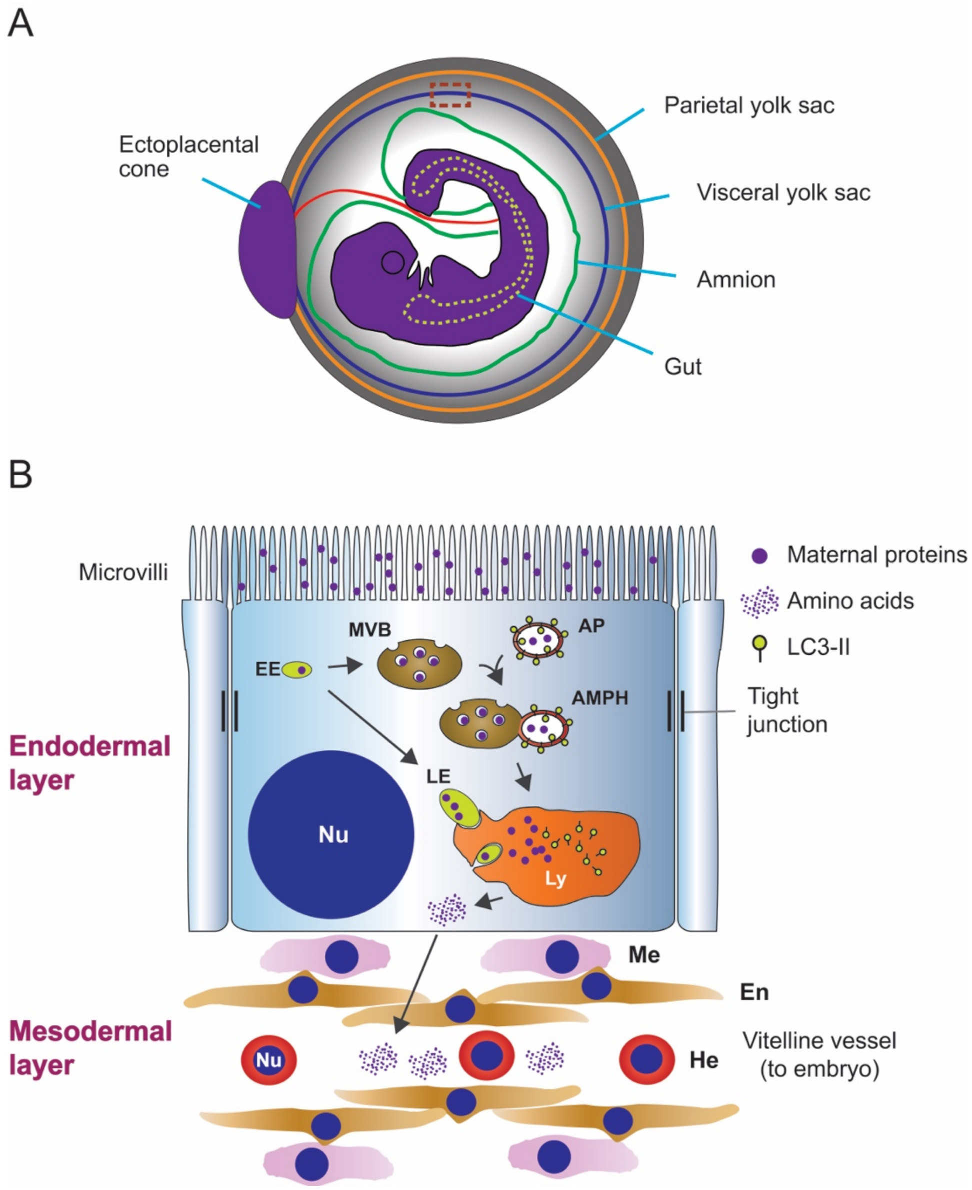

Figure 3: The structure and function of the visceral YS of murine embryos.

(A) A cross-section of a mouse embryo at E9.5 with the YS intact. (B) An enlarged view of a dotted rectangle in A. the visceral YS of early mouse embryos at E9.5 is composed of two developmentally distinct layers: an outer layer derived from the endoderm and an underlying layer derived from the mesoderm. the YS at E9.5 contains a constitutive, bulk protein degradation system that absorbs maternal proteins from the YS cavity and digests these foreign materials using lysosomal hydrolases. the model illustrates that endocytosed maternal proteins are delivered to and digested by the lysosome through early endosomes (EEs) and late endosomes (LEs). Lysosome-derived amino acids in the YS endoderm are supplied to the embryo via the vitelline circulation or used to synthesize paracrine that control vascular development in the mesodermal layer. Ap, autophagosome; Amph, amphisome; En, endothelial cells; Ly, lysosome; nu, nucleus; me, mesenchymal cell; he, hematopoietic cell [26].

In this chapter, we observe that UBR4 is required for the developmental processes during murine embryogenesis, in part through its function in heterophagy, a specialized autophagy targeting exogenous materials. Our previous and current studies together reveal a dual function of UBR4 in selective proteolysis by the proteasome and autophagic degradation by the lysosome.

2.2 MATERIALS AND METHODS

2.2.1 Construction of mice lacking UBR4

We cloned the *UBR4* gene from a bacterial artificial chromosome (BAC) library (CITB, Invitrogen, CA) derived from the mouse embryonic stem (ES) cell line CJ7 using a mouse *UBR4* cDNA fragment (nt 4231-5430) as a probe. The IRES-tau-lacZ-pA-ACNF plasmid, derived from the IRES-tau-lacZ-pA cassette [58] and the ACNF cassette [59], is a gift from Dr. Peter Mombaerts at the Rockefeller University. The targeting vector pUBR4KO-tauLacZ was constructed using gene recombineering (recombination-mediated genetic engineering) as described [60, 61], linearized with *Fse*I, and electroporated into E14 ES cells (a gift from Dr. Mombaerts). Targeted ES cell clones were analyzed using Southern blotting and PCR analysis. The clone 2F12 ES cells were injected into C57/BL6J blastocysts to generate chimeric mice which, in turn, were used to obtain germline transmission of the *UBR4*$^{-}$ mutant allele.

2.2.2 Antibodies

Rabbit polyclonal anti-human UBR4 antibody (1:400), raised against residues 3755–4160 [62], was used for immunostaining of the YS. Rabbit polyclonal anti-UBR4 antibody (1:500, IHC-00640, Bethyl laboratories, Montgomery, TX) was used for immunostaining of cultured cells. Other primary antibodies are rabbit polyclonal anti-V5 (1:500, V8137, Sigma, St. Louis, MO), goat polyclonal anti-ATG12 (1:100, SC-70128, Santa Cruz Biotechnology, Santa Cruz, CA), goat polyclonal anti-ATG5 (1:200, SC-8666, Santa Cruz Biotechnology), and goat polyclonal anti-LC3 (1:100, SC-16755, Santa Cruz Biotechnology). The following secondary antibodies were from Invitrogen (Eugene, OR): Alexa Fluor 488 goat anti-rabbit IgG (1:200, A11034), Alexa Fluor 555 donkey anti-goat IgG (1:200, A21432), Alexa Fluor 555 goat anti-mouse IgG (1:200, A21424), and anti-rat IgG-HRP (1: 500, Jackson ImmunoResearch).

2.2.3 Cell culture

HEK293 cell was purchased from the American Type Culture Collection (ATCC). All the cell lines were determined to be negative in a mycoplasma test using a MycoAlert detection kit (Lonza, LT07-118). HEK293 cell was cultured in Dulbecco’s Modified Eagle’s Medium (DMEM; Gibco,10566016). The media was supplemented with 10% FBS and 100 units/mL penicillin/streptomycin. All the culture plates and the cell lines were maintained at 37°C and 5% CO_2 in a humidified incubator.

2.2.4 Immunohistochemistry

For immunohistochemistry of animal tissues, paraffin-embedded slides were treated with xylene, followed by gradual dehydration in EtOH (100%, 90%, 80% and 70%; 6 min each) and rehydration in water for 20 min. The slides were treated with blocking solution (1% BSA and 0.2% Triton X-

100 in PBS) for 1 h and incubated with primary antibodies and subsequently secondary antibodies. The slides were counter-stained with 4′,6-Diamidino-2-phenylindole dihydrochloride (DAPI; Sigma, D8417) and mounted with Vectashield antifade mounting medium (Vector lab, H1000). Confocal images were taken by Fluoview FV1000 confocal laser scanning microscope equipped with Olympus Plan-Apo 60X (1.42 NA) oil immersion lens and analyzed using Fluoview software (Olympus, Shinjuku-ku, Japan). Two ImageJ (1) plugins, colocalization finder (by Christophe Laummonerie and Jerome Mutterer) and JACoP (Just Another Co-localization Plugin, 2), were used to evaluate colocalization of fluorescent images.

2.2.5 Immunocytochemistry of cultured cells

Coverslips were coated with diluted poly-L-lysine (1:10 in sterile deionized water) for 30 min at room temperature. After washing, the coverslip was exposed under a UV radiation lamp overnight in a hood. Cells were cultured on the coated coverslips and fixed in 4% paraformaldehyde (PFA) in PBS (pH 7.4) for 0.5 h at room temperature. After washing twice with PBS, the slide was treated with blocking solution (5% FBS and 0.3% Triton X-100 in PBS) for 1 h, followed by incubation with primary and secondary antibodies, subsequently.

2.2.6 Immunoelectron microscopy

HEK293-UBR4V5 cells were fixed in 2% PFA in PBS (pH 7.4) for 1 h and washed with PBS. Fixed cells were collected by scraping and resuspended in 3% gelatin. The gelatin was solidified on ice, and cells embedded in gelatin were fixed again with 2% PFA for 15 min. After cryoprotected with 2.3 M sucrose with PVP solution overnight, samples were frozen in liquid nitrogen and were trimmed into 0.5 mm cubes. The frozen cell blocks were sectioned by cryomicrotome (Leica EM Crion) in 70 nm sections and collected on 200 mesh grids. Primary antibodies were diluted in PBS with 0.5% BSA and 0.15% glycine. Donkey anti-rabbit 12 nm gold and donkey anti-goat 18 nm gold beads were diluted to 1:25 before use. After immunostaining, sections were incubated with 2.5% glutaraldehyde for 10 min and with 2% Neutral UA acetate for 7 min. Sections were further processed with 4% uranyl acetate and methyl cellulose for contrasting and drying, respectively. After drying, samples were recorded using JEOL JEM1011 TEM with high resolution AMT digital camera (Peabody, MA).

2.2.7 Establishment of *UBR4*$^{-/-}$ MEFs

Primary MEFs were established from E8.5 *UBR4*$^{-/-}$ embryos and their +/+ littermates. The embryos were minced by pipetting in Iscove's Modified Dulbecco's Medium (IMDM) (Invitrogen, #31980-022), 15% FBS (Hyclone), 0.1 mM non-essential amino acids (Invitrogen), 0.1 mM β-mercaptoethanol, and 100 U/ml penicillin/streptomycin (Invitrogen). The cells were seeded on the gelatinized 35 mm culture dish. Permanent cell lines were established from primary MEFs through crisis-mediated immortalization over 10 passages.

2.2.8 Proximity ligation assay

The proximity ligation assay (PLA) was used to visualize protein-protein interactions in UBR4V5 stable HEK293 cells using reagent kit (Olink Bioscience, Uppsala, Sweden). The cells were fixed with 4% PFA for 0.5 h and blocked for 1 h in 10% goat serum (Invitrogen, Camarillo, CA), followed by incubation with UBR4 and test antibodies (ATG12 or LC3) in antibody solution (0.3%

Triton X-100 and 5% bovine serum albumin in PBS) overnight at 4 °C. The cells were incubated with two oligonucleotide-tagged probe antibodies to primary antibodies. Annealing of the probes occurs when the target proteins are within 400 Å from each other, which initiates the amplification of Green fluorophore. Following 1 h incubation with the PLA probes, the cells were subject to hybridization, ligation, and DNA amplification in accordance with the manufacturer's instruction. A z-stack image of the green PLA signals was collected by 20 sampling the specimen at different focal planes (0.53 μm /slice) using confocal microscope (Olympus, FV1000).

2.3 EXPERIMENTAL RESULTS

2.3.1 Mice lacking UBR4 die during early embryogenesis.

To determine the role of UBR4 in mammalian development, we constructed mice lacking UBR4. As the UBR box is a general substrate recognition domain for destabilizing N-terminal residues, a UBR box-containing region spanning exons 36 through 42 was replaced with IRES (internal ribosome entry site)-translated tau-lacZ and a floxed tACE-Cre-Neo cassette in embryonic stem (ES) cells (Figure 4). The selection marker Neo flanked by loxP sites was removed by the Cre-recombinase expressed from the tACE (angiotensin-converting enzyme) promoter in spermatogonia of germline-transmitted F1 pups (Figure 4). Genotyping F2 C57BL/6J:129/Ola hybrid offspring from heterozygous parents yielded no viable *UBR4*$^{-/-}$ mice (Table 1), indicating that *UBR4*$^{-/-}$ mice die as embryos or neonates. By E9.0-9.5, *UBR4*$^{-/-}$ embryos were retrieved at Mendelian ratios but growth-arrested at the 14- to 18- somite stage, some of which were found dead (Table 1). No live mutants were retrieved at E11.5 and afterwards. Thus, mouse UBR4 is

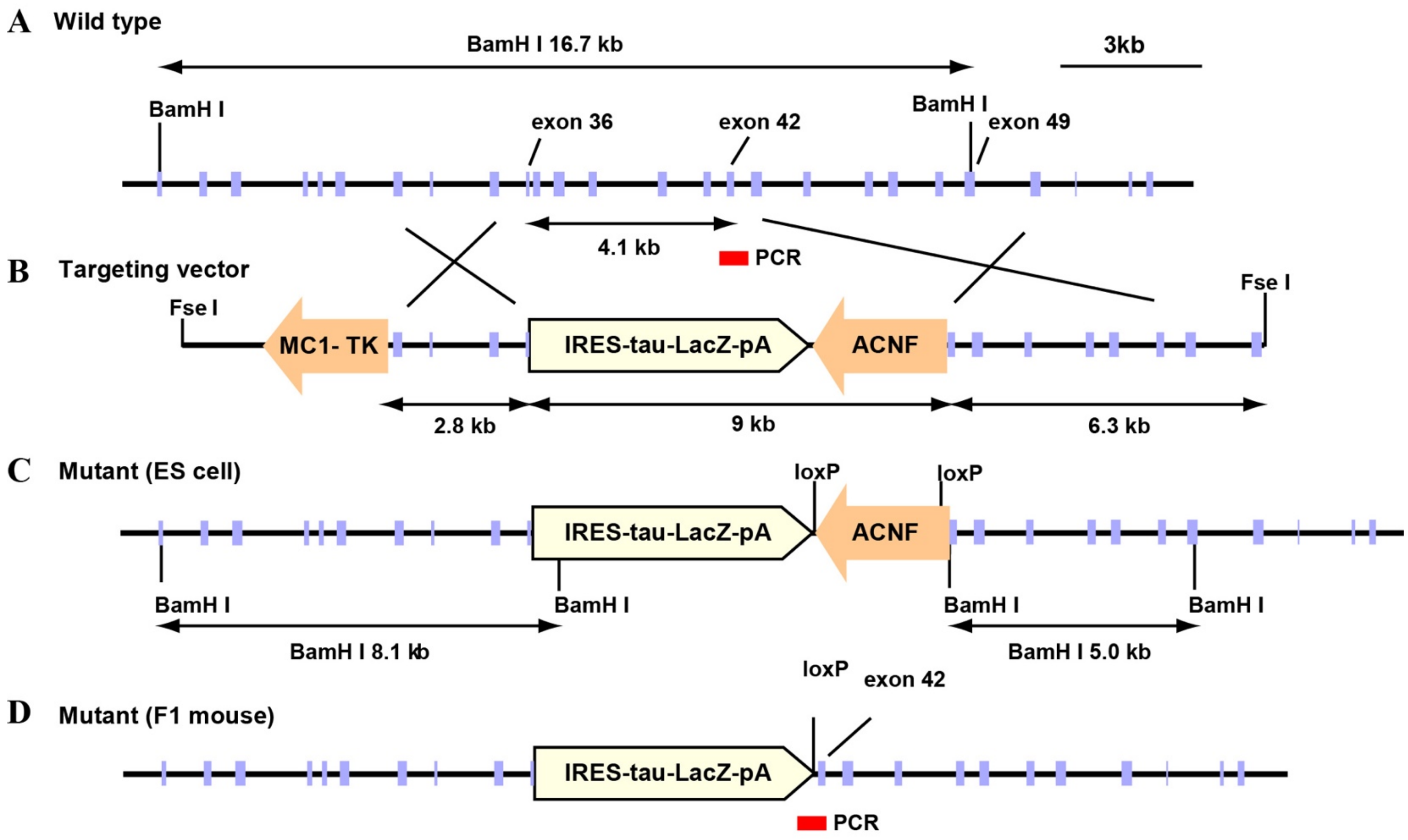

Figure 4: Targeting strategy of the UBR4 gene using recombineering.

(A) Restriction map of the ~7.5-kb 5′-proximal region of the ~108-kb mouse UBR4 gene spanning exons 27 through 53. (B) Targeting vector. (C) Targeted UBR4− allele in ES cells. (D) Targeted UBR4− allele in F1 pups. Exons are denoted by solid vertical rectangles. Directions of transcription of the neomycin (neo) and the thymidine kinase (tk) genes are indicated. Homologous recombination resulted in the replacement of the UBR4 exons 36–42 with the neo cassette. Exons 36 and 37, marked by an asterisk, contain Gly and Asp that are conserved in the UBR box N-recognin family and are essential for binding to type-1 destabilizing N-terminal residues in Saccharomyces cerevisiae Ubr1. Primers used for PCR genotyping are indicated by solid rectangles [24].

Table 1: Litter size of embryos from *UBR4*$^{+/-}$ intercrosses.

Stage	+/+	+/-	-/-	ND	# litter	Ave. litter size
E8.5	27	39	22		10	8.8
E9.0	13	23	12[a]		5	9.6
E9.5	43	107	40 [a]	3	23	8.4
E10.5	7	17	6 [a]	3	4	8.3
E11.5	6	8, 2[b]	3 [b]		2	6.0
E12.5	3	5	0		1	8.0
E15.5	1	2	0		1	3.0
P21	65	138	0		35	5.8

Footnote: a, morphologically abnormal; b, found dead; ND, not determined [24].

indispensable for survival during embryogenesis.

2.3.2 UBR4 is highly expressed in the YS endoderm.

This prompted us to examine UBR4 expression on the cross section of the YS comprising two developmentally distinct layers, the outer layer derived from the endoderm and the inner layer from the mesoderm (Figure 5A). Instead, the staining of UBR4 was largely restricted to autophagy-enriched endodermal cell layer that coordinates differentiation of mesoderm-derived vascular cells

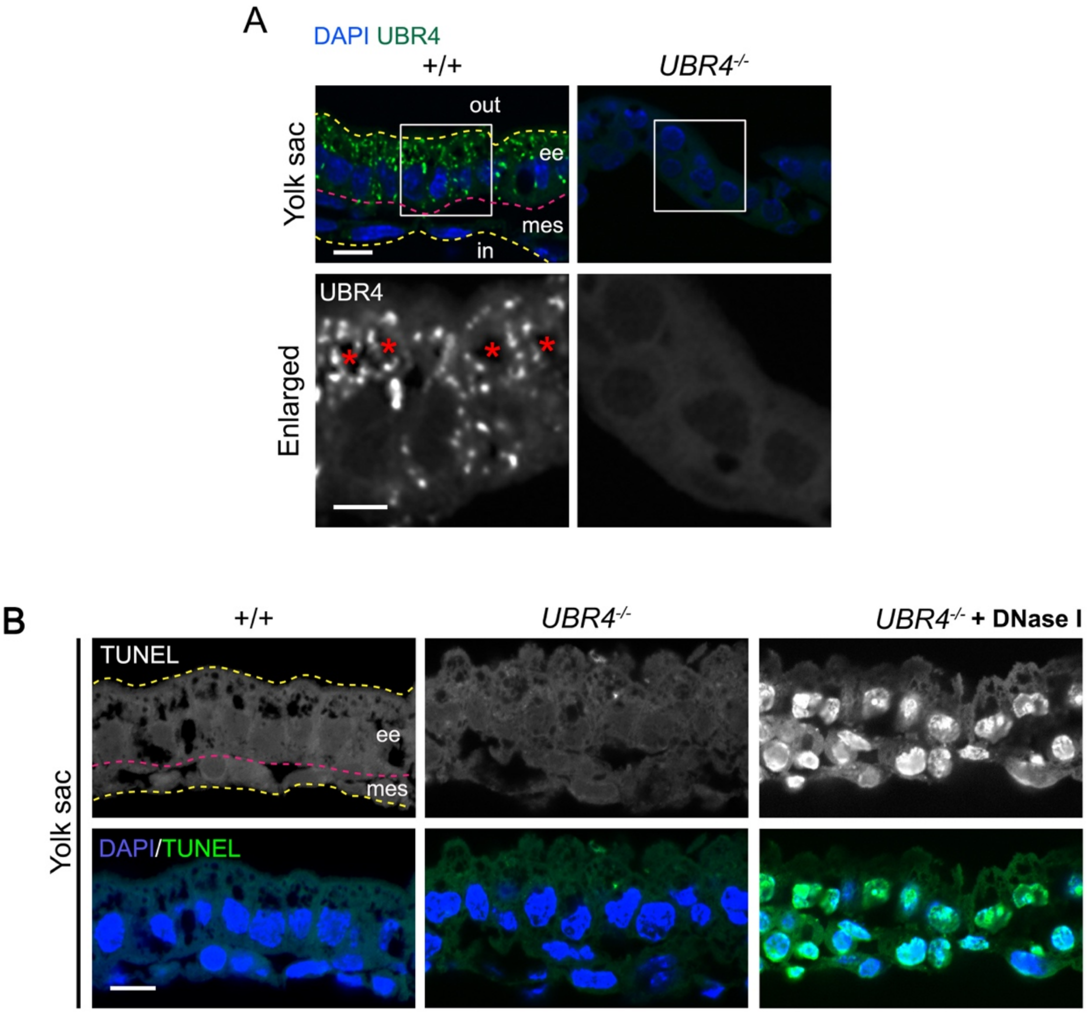

Figure 5: Expression of UBR4 in the YS endoderm.

(A) Immunostaining of UBR4 on cross-sections of +/+ and *UBR4*$^{-/-}$ YS at E9.5 (scale bar, 10 μm). Enlarged views of areas indicated by rectangles (scale bar, 5 μm). *, lysosomal vacuole. (B) TUNEL assay of +/+ and *UBR4*$^{-/-}$ YS at E9.5. DNase 1 was treated on *UBR4*$^{-/-}$ YS as a positive control for TUNEL^{+} cells. ee, extraembryonic endoderm; mes, mesodermal layer [24].

and supplies lysosome-produced amino acids during early embryogenesis. *UBR4*$^{-/-}$ YS showed a comparable level to +/+ in apoptosis as determined by terminal deoxynucleotidyl transferase dUTP nick end labeling (TUNEL) assay (Fig. 5B).

2.3.3 UBR4 is associated with autophagosome in the YS endoderm.

To determine the function of UBR4 in the YS endoderm, we immunostained endogenous UBR4 on YS cross sections at E9.5. In contrast to typical cytosolic proteins of the UPS that would appear to be diffusive, the staining appeared as cytosolic punctate signals (Figure 6A). Although morphologically heterogeneous, some had round shape with diameters of 0.1-0.3 or ~1.0 μm and distributed with lysosomal vacuoles in a cytosolic compartment between the microvilli and nucleus (Figure 6A). A significant portion of UBR4 puncta were at least partially associated with puncta positive for LC3, a hallmark of double membrane structures (Figure 6A). Despite colocalization, the shapes and sizes of UBR4 puncta were distinct from those of LC3 puncta. In addition, a confocal distance measurement indicated that the center of UBR4 puncta was separated from that of LC3 puncta by approximately 0.15 μm (Figure 6B-D). These results suggest that UBR4 is not a constitutive component of autophagic machinery but associated with autophagic cargoes. Next, we asked whether UBR4-loss affects autophagic activity. Immunostaining of LC3 on YS cross sections from +/+ and *UBR4*$^{-/-}$ embryos at E9.5 indicated that *UBR4*$^{-/-}$ YS contained a markedly increased level of LC3 puncta in number and signal intensity (Figure 6E), without significant changes in cell death (Figure 5B). ATG12 puncta, a hallmark of phagophores, were also significantly induced in *UBR4*$^{-/-}$ YS, though less striking compared with LC3 (Figure 6E). Given that MVBs carrying maternal proteins from the YS cavity are major autophagic cargoes in the YS endoderm, we asked whether UBR4 is associated with the MVB using the transmission electron microscopy (EM). The EM of UBR4 and LC3 in HEK293-UBR4V5 cells identified one or a few UBR4 dots (not as a cluster of aggregates) within the MVB or in the proximity of endosome-like

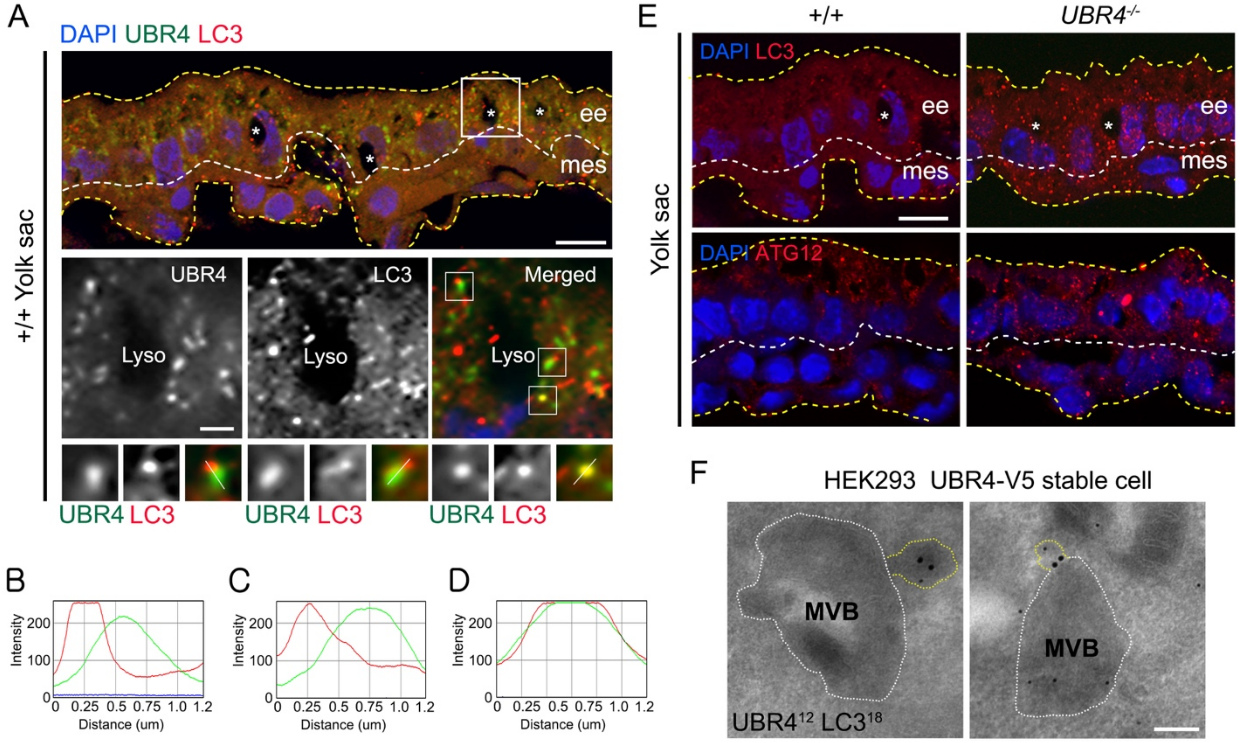

Figure 6: UBR4 is associated with autophagosome of the YS endoderm.

(A) Immunohistochemistry assay for UBR4 and LC3 in cross-sections of the +/+ and *UBR4*$^{-/-}$ YS. *, lysosome (scale bar, 10 μm). Enlarged views of area indicated by rectangles (scale bar, 2 μm). (B-D) Distances between UBR4^{+} and LC3^{+} puncta. (E) Immunohistochemistry assay for LC3 and ATG12 in cross-sections of the +/+ and *UBR4*$^{-/-}$ YS (scale bar, 10 μm). *, lysosome.(F) Electron microscopy analysis of HEK293–UBR4V5 stably overexpressed cells labeled for UBR4 (12 nm) and LC3 (18 nm) (scale bar, 200 nm) [24].

cellular materials and LC3 at the ‘entrance’ of the MVB (Figure 6F). These results suggest that UBR4 plays a role in a tissue-specific constitutive autophagic pathway of the YS endoderm, through its association with autophagic cargoes.

2.3.4 UBR4 plays a role in delivery of autophagic cargoes to phagophores.

To test whether UBR4 has a general function in autophagy, we immunostained UBR4 in HEK293 cells expressing 570 kDa-UBR4 with C-terminal V5 tag (UBR4V5). The immunostaining analysis revealed cytosolic punctate signals with diameters of 0.1-0.3 or ~1.0 μm, typical for phagophores and autophagosomes, respectively (Figure 7A). Most UBR4 puncta colocalized at least partially with LC3 puncta (Figure 7A), a hallmark of phagophores and autophagosomes. UBR4 puncta with sizes of 0.1-0.3 μm also showed similar colocalization with ATG12 and ATG5 that mark phagophores (Figure 7A). However, UBR4 puncta had shapes and sizes distinct from those of ATG12, ATG5, and LC3. To directly determine the association of UBR4 with autophagic vacuoles, we performed the EM of UBR4V5 in HEK293-UBR4V5 cells (Figure 7B). The analysis identified one or a few individual UBR4V5 dots (not as a cluster of aggregates) in association with cargo-like materials with a diameter of approximately 0.1 μm and in the proximity of ATG12 on the surface or lumen of autophagic vacuoles (Figure 7B). These results collectively suggest that UBR4 can be associated with cellular materials to form UBR4-cargo complexes which, in turn, are delivered to LC3-positive autophagic vacuoles. However, we do not exclude the possibility that a fraction of overexpressed UBR4 molecules are misfolded and, thus, deposited to autophagic vacuoles.

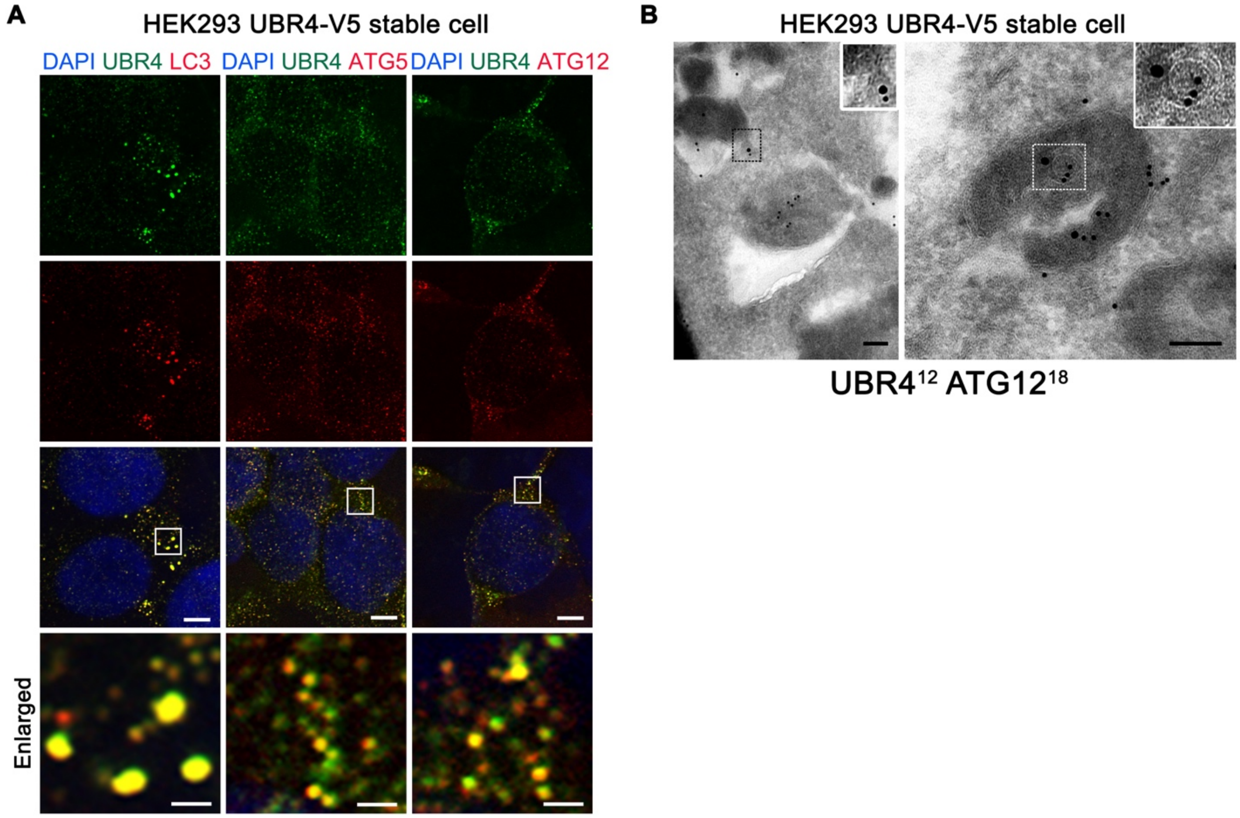

Figure 7: UBR4 plays a role in delivery of autophagic cargoes to phagophores and autophagosome.
(A) Immunostaining of UBR4 in comparison with LC3, ATG5, and ATG12 in HEK293–UBR4V5 stably expression cells. Enlarged views of areas indicated by rectangles. (B) Immunoelectron microscopy of HEK293–UBR4V5 cells labeled for UBR4 (12 nm) and ATG12 (18 nm) (scale bar, 100 nm). Enlarged views of areas indicated by rectangles [24].

2.3.5 Amino acid starvation facilitates UBR4 association with autophagic core machineries.

To examine whether nutrient deprivation promotes UBR4 association with autophagic core machinery, we employed proximity ligation assay (PLA) which visualizes two proteins located in the proximity (< 400 Å) based on the ability of antibody-conjugated oligonucleotides to hybridize with each other. The PLA of UBR4V5 and LC3 in HEK293-UBR4V5 cells revealed punctate signals with diameters of ~1.0 μm (2.76 ± 0.28 per cell, N=148), indicating multiple UBR4-LC3

PLA interactions within autophagosomes (Figure 8). UBR4V5 showed similar PLA interactions with its upstream components, ATG12 (1.47 ± 0.33, N= 51) and ATG5 (3.36 ± 0.31, N= 77). Nutrient deprivation for 1 h caused a significantly increased correlation between UBR4 and LC3 (7.96 ± 0.39, N= 101; *** *p = 0.001*) and, to a less degree, ATG12 (3.2 ± 0.37, N= 27; ** *p = 0.002*) and ATG5 (5.04 ± 0.34, N= 111; *** *p = 0.0007*) as well. These results together suggest that nutrient deprivation promotes the association of UBR4 with autophagic cargoes, leading to its degradation by autophagy.

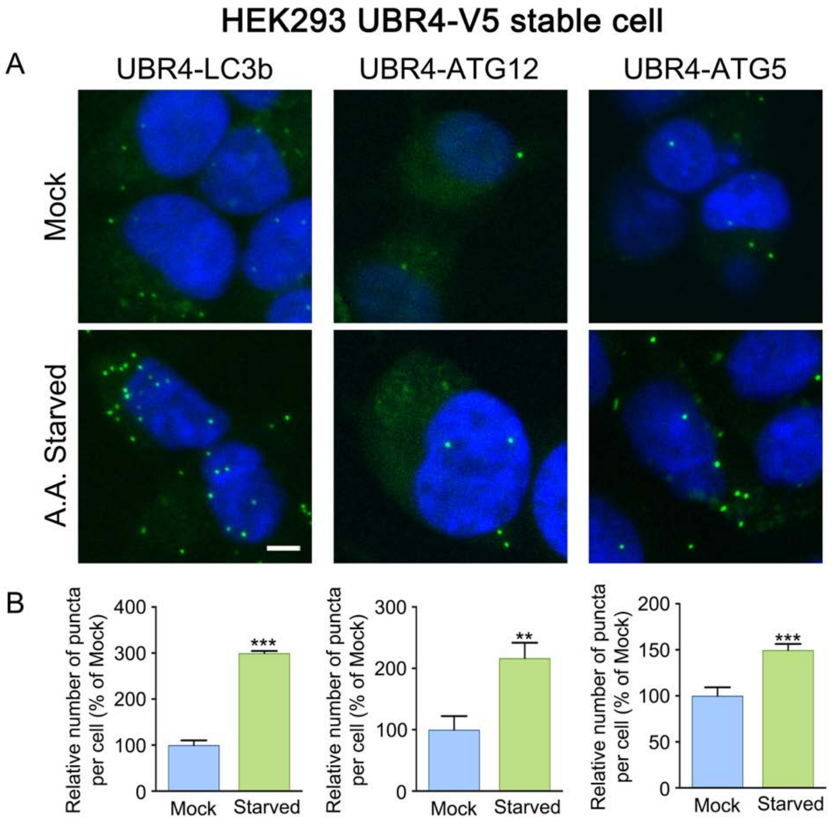

Figure 8: PLA assay of UBR4 in comparison with LC3, ATG12, and ATG5 in HEK293–UBR4V5 cells. (A) PLA of UBR4 with LC3, ATG12, and ATG5 in control and amino acid starved HEK293-UBR4V5 cells (scale bar, 5 μm). (B) Quantification of A, representing the number of PLA$^+$ puncta per cell. Data are presented as mean percentage ± SEM of Mock. Statistical significance was determined using two-tailed t-test.

2.3.6 UBR4-loss results in misregulation of autophagic induction and flux.

Given the enhanced formation of LC3 and ATG12 cytosolic puncta in *UBR4*$^{-/-}$ YS (Figure 6E), we examined autophagic induction and flux in +/+ and *UBR4*$^{-/-}$ MEFs. Both of Immunostaining and immunoblotting analyses showed that *UBR4*$^{-/-}$ MEF contained a higher level of LC3 compared with +/+ cells (Figure 9A and B; 9C, lane 1 vs. 3). Cytosolic form LC3-I is accumulated in *UBR4*$^{-/-}$ MEFs even in normal growth media. Transient over-expression of UBR4V5 in *UBR4*$^{-/-}$ MEFs only marginally reduces the synthesis of LC3-I and the formation of LC3 foci. This marginal effect provides a possibility that autophagic induction in *UBR4*$^{-/-}$ cells is caused by cellular stress and/or impairment of organelles that cannot be readily rescued by transient supplement of UBR4.

Immunoblotting analysis confirmed that *UBR4*$^{-/-}$ MEFs contained significantly increased basal levels for LC3-I and LC3-II (Figure 10A) as well as GABARAP-I and GABARAP-II (Figure 10B, lanes 2 vs. 1), which are the other homologs of LC3 in mammalian system. Transient over-expression of Green Fluorescence Protein (GFP)-associated LC3 (GFP-LC3) confirmed that formation of cytosolic punctate structures was activated in *UBR4*$^{-/-}$ MEFs growing in normal as well as starvation media (Figure 10C). These results suggest that UBR4 deficiency can induce autophagic pathway. To further characterize the role of UBR4 in autophagy, we transiently transfected HEK293 cells with small interfering RNA (siRNA) against human UBR4. Transiently silencing of human *UBR4* markedly induced the formation of LC3 puncta in HEK293 cells (Figure 11A). Moreover, transient re-expression of recombinant UBR4V5 in human UBR4-knockdown HEK293 cells reverted those induced LC3 puncta back to the basal level (Figure 11). These results indicate that UBR4 plays an active role in autophagic flux.

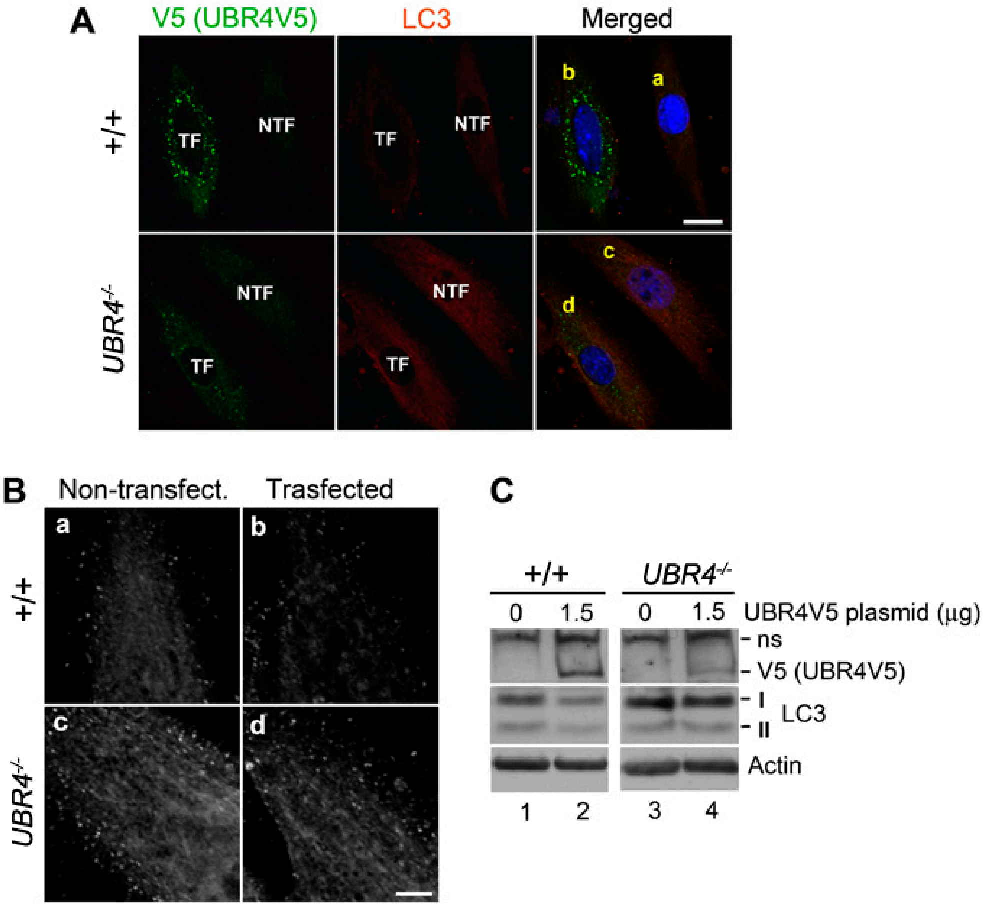

Figure 9: ***UBR4*$^{-/-}$ MEF contained a higher level of LC3.**

(A) Expression and conversion of LC3 in +/+ and *UBR4*$^{-/-}$ MEFs transiently expressing UBR4V5. Immunofluorescent analysis of V5 (UBR4V5) and LC3 in +/+ and *UBR4*$^{-/-}$ MEFs transiently transfected with a plasmid encoding UBR4V5. +/+ and *UBR4*$^{-/-}$ MEFs were transfected with a plasmid (1.0 μg) encoding UBR4V5 (scale bar, 20 μm). (B) Enlarged views of the cellular areas indicated by a–d. a; non-transfected +/+ cell; b, transfected wild-type cell; c, non-transfected *UBR4*$^{-/-}$ MEF; d, transfected *UBR4*$^{-/-}$ MEF cell (scale bar, 4 μm). (C) Immunoblotting analysis of V5 (UBR4V5) and LC3 in +/+ and *UBR4*$^{-/-}$ MEFs transiently transfected with the indicated amounts of a plasmid encoding UBR4V5 [24].

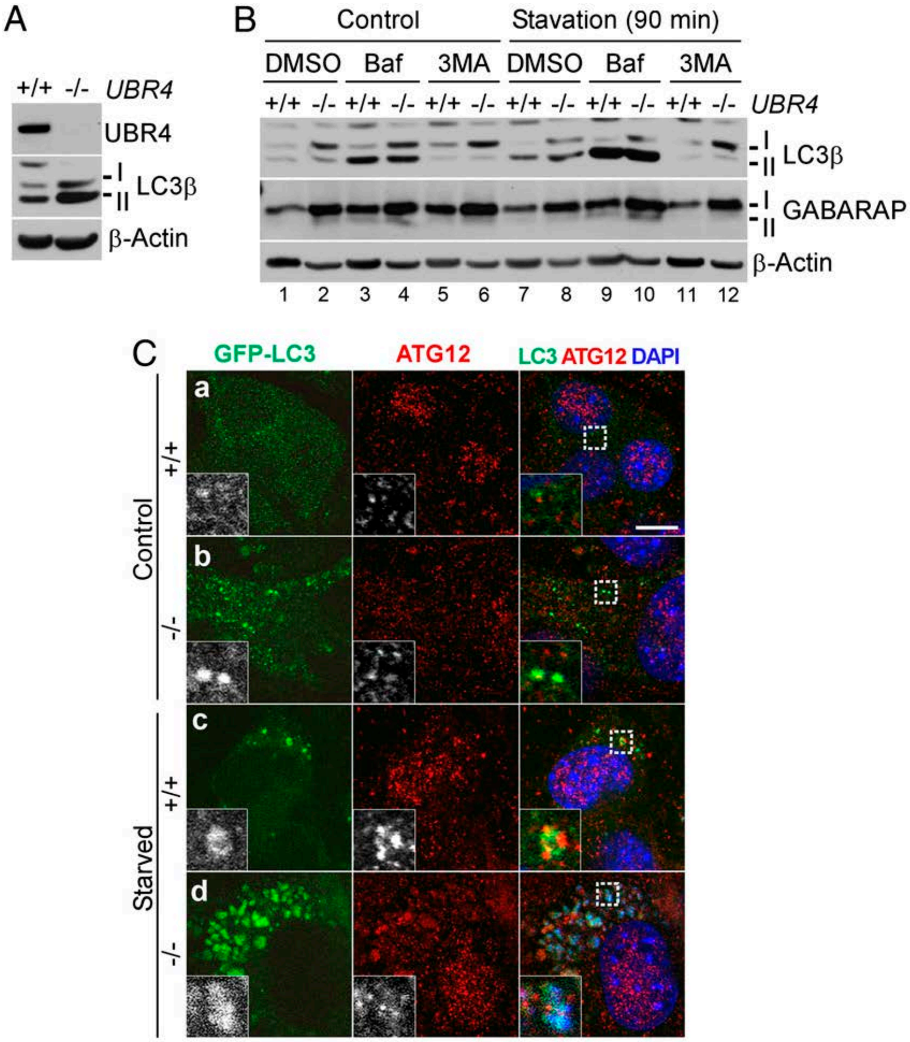

Figure 10: UBR4 loss leads to multiple misregulations of autophagic induction and flux.

(A) Immunoblotting of +/+ and *UBR4*$^{-/-}$ MEFs. (B) Immunoblotting of +/+ and *UBR4*$^{-/-}$ MEFs growing in normal or starvation medium for 90 min in the presence or absence of 0.2 μM bafilomycin A1 or 10 mM 3-methyladenine (3MA). (C) Immunostaining of transiently expressed GFP-LC3 and endogenous ATG12 in +/+ and *UBR4*$^{-/-}$ MEFs. Panels A and B were conducted by Takafumi Tasaki [24].

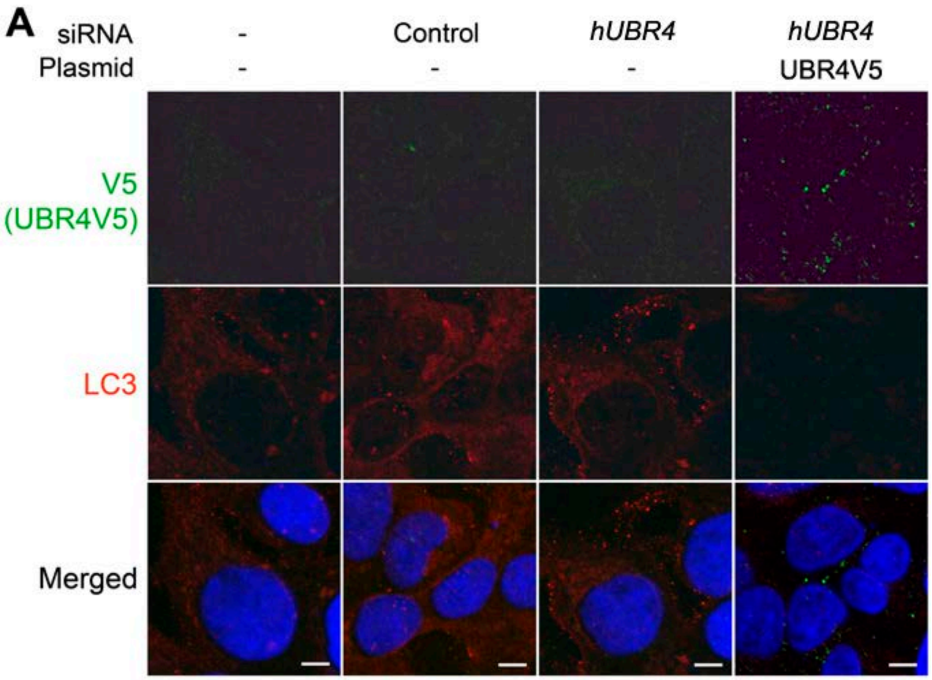

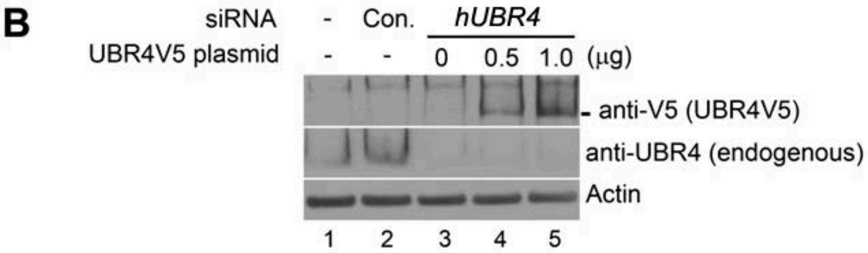

Figure 11: Knockdown of UBR4 induces the formation of LC3 puncta in HEK293 cells.

(A) HEK293 cells were transfected with control or si*UBR4* siRNA. After 48 h post-siRNA transfection, the cells were transfected with 1 μg UBR4V5 plasmid. After 24 h from the transfection, cells were subjected to immunocytochemistry of V5 (UBR4V5) and LC3 (scale bar, 5 μm). (B) Immunoblotting analysis of HEK293 cells that had been treated with si*UBR4* for 48 h, followed by transient transfection of the plasmid UBR4V5. Note that overexpression of UBR4V5 in UBR4 knockdown cells results in disappearance of endogenous human UBR4 and accumulation of recombinant human UBR4V5 [24].

2.4 DISCUSSION AND CONCLUSION

The results presented in the study suggest that UBR4 subpopulation in the YS endoderm is specifically associated with cellular cargoes to form UBR4-cargo complexes destined to autophagosomes and lysosomal vacuoles. Given that embryo requires lysosome-derived amino acids digested from the YS endoderm, it is likely that misregulation of autophagic pathways in the *UBR4*$^{-/-}$ YS endoderm significantly contributes to embryonic lethality with multiple developmental defects.

In this study we demonstrate that mice lacking UBR4, a newly identified N-recognin, die during early embryogenesis associated with induced autophagy pathway in YS endoderm. The YS endoderm is a specialized digestive organ wherein maternal proteins from the YS cavity are endocytosed and digested into amino acids through the MVB-autophagosome-lysosome pathway [57]. What is the function and mechanism of UBR4 in the autophagic and MVB pathway, as the N-recognin of the N-end rule pathway? The N-end rule pathway has been characterized as a proteolytic system that controls the half-lives of cytosolic short-lived proteins through selective proteolysis by the 26S proteasome. N-recognin, known to bind to substrates of selective proteasomal degradation, is also associated with substrates of bulk lysosomal degradation. UBR4 does not have a known ubiquitylation domain but does contain the UBR box which is conserved in the UBR N-recognin family and binds to type-1 destabilizing N-terminal residues, including the primary degron Arg. Therefore, it is natural to speculate that UBR4 is associated with (unknown) cellular cargoes through binding of the UBR box to the N-terminal Arg exposed from the substrates (Fig 12).

UBR4 has a putative LC3 interacting region (LIR), which is predicted by iLIR database (https://ilir.warwick.ac.uk) (Fig. 12) [63]. Through the interaction with LC3, UBR4 can bind proteasomal and/or autophgic cargoes, exposing the primary degron, and deliver them to phagophore/autophagosome pathway for selective degradation under cellular stresses. Our results show that *UBR4*$^{-/-}$ YS and MEFs contain an increased level of LC3$^+$ puncta as compared with controls. This suggests that multiple misregulations of autophagy and other UBR4-dependent processes in *UBR4*$^{-/-}$ cells result in cellular stress (e.g., nutrient insufficiency, and/or accumulation of damaged organelles) which, in turn, stimulates the formation of autophagic vacuoles.

Further investigation is needed to understand the mechanism by which UBR4 plays a dual role in selective degradation of short-lived proteins *via* the proteasome and bulk degradation of cellular materials *via* the lysosome.

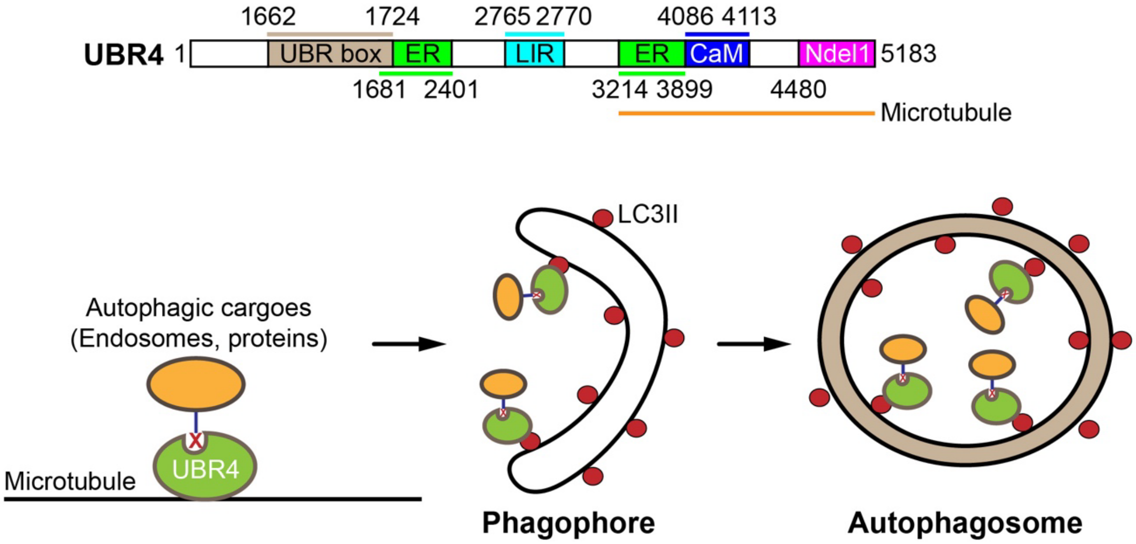

Figure 12: UBR4 domains and protein binding regions.

UBR4 contains UBR box that binds to type-1 destabilizing N-degrons, including the primary degron Arg. It has an atypical calmodulin (CaM)-binding domain. The C-terminal of UBR4 contains a large microtubule-binding region, which overlaps with Ndel1-binding region. It includes two ER-associated domains and a putative LC3 interacting region (LIR).

3.0 THE ROLE OF THE N-RECOGNIN UBR4 IN THE BIOGENESIS OF THE EARLY ENDOSOME

[Kim ST, Lee YJ, Tasaki T, Mun S, Hwang JS, Kang MJ, Ganipisetti S, Yi EC, Kim BY, and Kwon YT., The N-recognin UBR4 of the N-end rule pathway is targeted to and required for the biogenesis of the early endosome. Journal of Cell Science. July 30 2018. Accepted]

3.1 RESEARCH BACKGROUND

In eukaryotes, cellular proteins are mainly degraded by the UPS, autophagy, and/or endosomal system. In the UPS, proteasomal proteases degrade Ub-tagged short-lived and misfolded/damaged substrates into short-peptides [21, 64-66]. Autophagy uses lysosomal hydrolases to degrade various long-lived and insoluble misfolded proteins into amino acids [67]. By contrast, plasma membrane-associated and extracellular proteins are endocytosed and sequestered in endosomes and degraded by endosomal hydrolases into short peptides and truncated proteins [68-72]. Studies have shown that approximately 50% of the plasma membrane and 5-30% of cellular volumes are internalized in every hour [73, 74]. As such, the plasma membrane and associated proteins can be almost entirely replaced by new materials in just one hour [73, 74]. Although the majority of cell surface proteins are short-lived substrates of endosomal proteolysis, the key regulators underlying endosomal processes remain incompletely understood.

The substrates of endosomal proteolysis are endocytosed and sequestered within endocytic vesicles [74-78] (Figure 13). Endocytic vesicles can be recycled back to the membrane [79] or homotypically fused with each other to form early endosome (pH 5.8-6.3) [72, 80], in which the cargoes are digested by endosomal hydrolases into short peptides or truncated fragments [72, 73, 81-83]. The partially digested cargoes are further degraded as early endosomes undergo maturation into late endosomes (pH 5.4-5.8) containing approximately 50 hydrolases [71, 84-86] (Figure 13). The proteolytic products in late endosomes are released into the cytosol and further digested by the proteasome and aminopeptidases [71, 87]. Together, approximately 80% of endosomal cargoes destined for degradation are digested within early endosomes or late endosomes which occurs

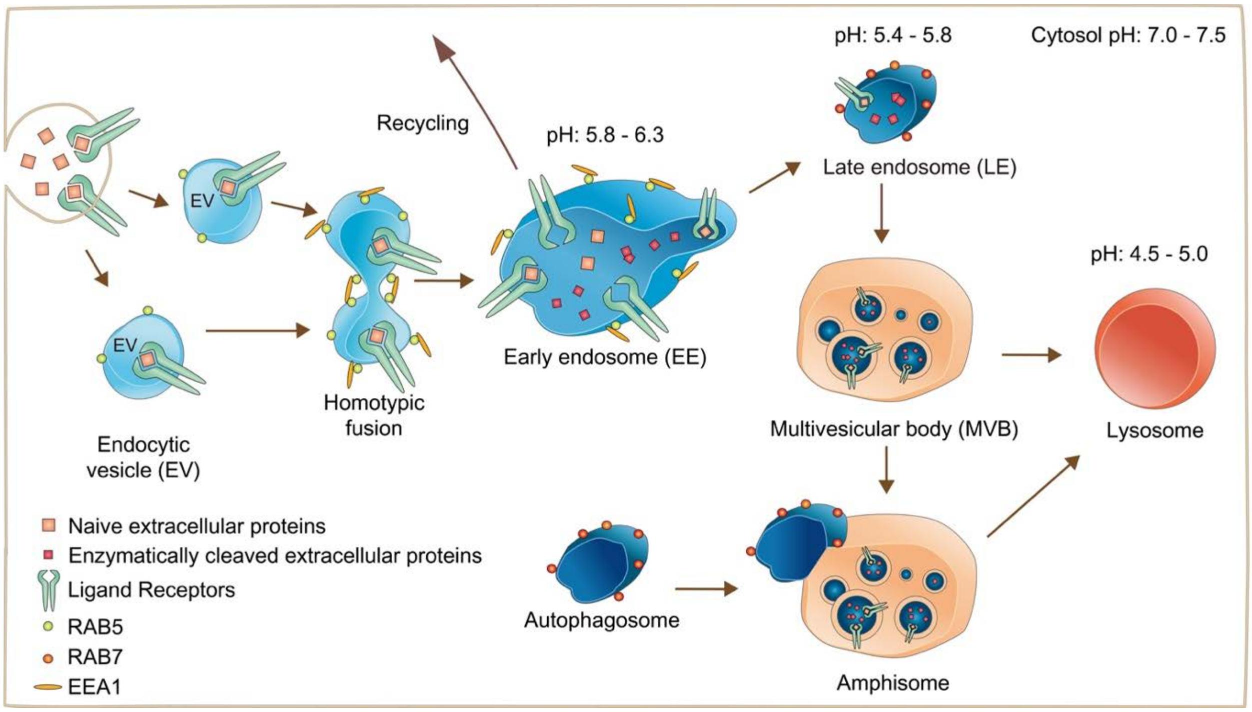

Figure 13. Endosomal maturation and proteolysis.

External contents and surface proteins are endocytosed via primary endocytic vesicles and accumulated in early endosomes (pH 5.8-6.3) through homotypic fusion. Within 10 min, early endosomes recycle their cargoes to the plasma membrane or partially digests the cargoes by endosomal hydrolases into short peptides. Through early-to-late endosome conversion, the undigested fragments are exposed to more acidic pH, which is optimal for the enzymatic activity of hydrolases in late endosomes (pH 5.4-5.8). A portion of early endosomes and late endosomes are fused to MVBs along with autophagosomes, which generates amphisomes. Eventually, multiple cargoes originated from various sources including extracellular contents, plasma membrane, and autophagosomes are digested by endosome-derived hydrolases in lysosomes (pH 4.5-5.0) into amino acids.

independent of lysosomes and, thus, are mechanistically distinct from the UPS and autophagy [70, 88]. The undigested cargoes in late endosomes are delivered to lysosomes (pH 5.0) and degraded into amino acids by lysosomal hydrolases [71]. Endosomes also mediate lysosome-independent degradation of autophagic cargoes sequestered in hydrolases-free autophagosomes. Specifically, a portion of early endosomes and late endosomes are fused with autophagosomes to form amphisomes and initiates the degradation of autophagic cargoes using their endosomal hydrolases

[71, 89] (Figure 13). In addition, some early endosomes and late endosomes are co-deposited to multivesicular bodies (MVBs) along with autophagosomes and their cargoes (Figure 13), wherein autophagic cargoes are degraded by endosomal hydrolases, independent of lysosomes [90]. The undigested and partially digested cargoes in amphisomes and MVBs are eventually digested by endosome-derived hydrolases in lysosomes into amino acids (Figure 13). Overall, the amounts of cargoes degraded in early endosomes, late endosomes, MVBs, and amphisomes, prior to lysosomal targeting, may rival or even exceed those by lysosomes, especially in normally growing cells.

The endocytic vesicles containing endosomal cargoes mature into early endosomes and subsequently late endosomes through a series of homotypic fusion. During this process, GTP-bound RAB5 is associated with endocytic vesicles and induces the formation of phosphatidylinositol 3-phosphate (PI3P) on endocytic vesicles [72] (Figure 13). The PI3P moieties on endocytic vesicles subsequently recruit EEA1 (early endosome antigen 1). PI3P-bound EEA1 is maximally ~240 nm long and tethers two endocytic vesicles through the interaction of its two ends with two RAB5 molecules, each of which on an endocytic vesicle [72, 91, 92]. The tethering of two endocytic vesicles by EEA1 is facilitated by Ca^{2+}-bound calmodulin that binds EEA1 and its conformational change from 70 nm to 240 nm long [93-95] (Figure 13). The cooperation amongst RAB5, EEA1, and calmodulin is critical for homotypic fusion of endocytic vesicles into early endosomes (Figure 13). The resulting early endosomes can be fused with endocytic vesicles or early endosomes in the course of maturation to an late endosome [72]. During the conversion of early endosomes to late endosomes, RAB5 is dissociated from early endosomes and replaced with the G-protein RAB7 [96]. To date, little is known about the peripheral components that modulate endosomal maturation and proteolysis.

The N-end rule pathway is a proteolytic system, in which single N-terminal amino acids function as a determinant of degradation signals (degrons), called N-degrons [3, 4, 10]. The degradation determinants include positively charged (Arg, Lys, and His; type 1) and bulky hydrophobic (Phe, Tyr, Trp, Leu, and Ile; type-2) residues on the protein N-termini [5, 97, 98]. Amongst these, the Arg N-degron can be generated by the conjugation of the amino acid L-Arg by *ATE1*-encoded R-transferases (EC 2.3.2) [15, 16, 97, 99]. The N-terminal Arg (Nt-Arg) of arginylated proteins can induce proteolysis by the N-end rule pathway via either the UPS or autophagy [11, 20, 100]. We have previously identified a family of N-recognins UBR1, UBR2, UBR4, and UBR5 [6, 101]. The E3 ligases UBR1 and UBR2 are RING finger proteins that mediate ubiquitination of short-lived and misfolded proteins in the cytosol and nucleus [6, 101]. Compared with UBR1 and UBR2, the biochemical mechanisms and physiological functions of UBR4 and UBR5 as N-recognins remain poorly understood.

Our earlier work has identified UBR4 as an N-recognin that can bind type-1 and type-2 N-degrons including Nt-Arg [8]. We and others have constructed knockout mice lacking UBR4 [24, 102]. Our mutant animals, in which a DNA region encoding the UBR box was deleted, die during embryogenesis at midgestation (~E9.5-10.5) associated with vascular defects and multiple misregulation of autophagic induction in the yolk sac (YS) [24, 26].

In this chapter, we show that UBR4 modulates the biogenesis of endosomes and the formation and functionality of endosome-related cellular structures. UBR4 loss impacts the trafficking and proteolysis of endocytosed protein cargoes. Our results suggest that UBR4 is a key regulator in the endosome-lysosome system, providing the mechanisms underlying the aforesaid observations with UBR4.

3.2 MATERIALS AND METHODS

3.2.1 Antibodies

Rabbit polyclonal anti-UBR4 antibody (Bethyl Laboratories, IHC-00640, 1:300) was used for immunohistochemical analysis of YS and embryos and immunocytochemical analysis of cultured cells. Other antibodies are as follows: rabbit polyclonal anti-EEA1 (Cell Signaling, 2411, 1:100), mouse monoclonal anti-EGFR (Santa Cruz, SC-374607, 1:200), rabbit polyclonal anti-RAB5 (Cell Signaling, 3547, 1:400), mouse monoclonal anti-RAB7 (Sigma, R8779, 1:1,300), rabbit polyclonal anti-V5 (Sigma, V8137, 1:500). For immunoblotting analysis, mouse monoclonal anti-β actin (Sigma, A1978, 1:10,000), rabbit polyclonal anti-UBR4 (Abcam, AB86738, 1:100), and mouse monoclonal anti-GAPDH (Sigma, G8795, 1:20,000) were used. The following secondary antibodies are from Invitrogen: Alexa Fluor 488 goat anti-rabbit IgG (A11034, 1:200), and Alexa Fluor 555 goat anti-mouse IgG (A21424, 1:200).

3.2.2 Plasmids and other reagents

mRFP-RAB5 and EGFP-calmodulin were kindly gifted from Ari Helenius (Addgene plasmid # 14437) and Emanuel Strehler (Addgene plasmid # 47602), respectively. EGFP-EEA1 and TagRFP-EEA1 were kindly gifted from Silvia Corvera (Addgene plasmid # 42307 and #42635, respectively. GFP and V5 tagged UBR4 plasmids were prepared as described in the previous studies[8, 24]. These plasmids were transiently transfected with Lipofectamine 3000 reagent following the manufacturer's instructions (Invitrogen). Normal goat serum (ab7481) was obtained from Abcam. Hoechst 33342 (H21492) was obtained from Invitrogen. 4′,6-Diamidino-2-phenylindole dihydrochloride (DAPI; D8417) and nocodazole (M1404) were obtained from Sigma. W-7 (681629) and latrunculin A (428021) were obtained from Calbiochem. Synthetic TAT-FITC peptide was purchased from Anygen (Kwangju, South Korea). The sequence was FITC-GGGGYGRKKRRQRRR-NH2. Vectashield antifade mounting medium (H1000) was from Vector lab. All other chemicals were reagent grades from Sigma or Merck.

3.2.3 UBR4 knockout mice

We have previously constructed UBR4-knockout mice, in which the UBR box, a substrate recognition domain for destabilizing N-terminal residues, was replaced with IRES (internal ribosome entry site)-translated tau-lacZ [24]. Animal studies were conducted according to the protocols (SNU130604-2-10) approved by the Institutional Animal Care and Use Committee at Seoul National University.

3.2.4 Cell culture

We previously established primary mouse embryonic fibroblasts (MEFs) from +/+ and *UBR4*$^{-/-}$ embryos at E8.5 [24]. Immortalized cell lines were established from primary MEFs through crisis-mediated immortalization over 10 passages [24]. MEF cells were cultured in Iscove’s modified Dulbecco’s medium (IMDM) (31980–022; Invitrogen), 15% FBS (HyClone), 0.1 mM non-essential amino acids (Invitrogen), 0.1 mM β-mercaptoethanol, and 100 units/mL penicillin/streptomycin (Invitrogen). CCL2 HeLa and HEK293 cell were purchased from the

American Type Culture Collection (ATCC). All the cell lines were determined to be negative in a mycoplasma test using a MycoAlert detection kit (Lonza, LT07-118). HeLa and HEK293 cell were cultured in Dulbecco’s Modified Eagle’s Medium (DMEM; Gibco,10566016). The media was supplemented with 10% FBS and 100 units/mL penicillin/streptomycin. All the culture plates and the cell lines were maintained at 37°C and 5% CO_2 in a humidified incubator.

3.2.5 RNA interference assay

Reagents for siRNA silencing were purchased from Life Technologies. Transfection was performed according to the manufacture’s protocol. Briefly, Cells were transfected with either siControl (Invitrogen, cat. #4390843), EEA1 siRNA (Origene, cat#SR30003), or UBR4 siRNA (Invitrogen, cat. #4392420, ID #23628) at a final concentration of 10 nM using Lipofectamine RNAiMAX reagent (Invitrogen, 13778150). Approximately 48 h after siRNA silencing, cells were harvested for immunoblotting and immunocytochemical analyses. The sequences of *UBR4* siRNAs are 5’-GCCUGUUCGAAAGCGCAAA (sense) and 5’-UUUGCGCUUUCGAACAGGC (antisense).

3.2.6 Immunoblotting analysis

Cells were washed with ice-cold PBS and lysed using RIPA buffer (50 mM Tris-HCl, 150 mM NaCl, 1% NP-40, 1% sodium deoxycholate, and 0.1% SDS) containing freshly prepared protease inhibitor cocktail (Sigma, P8340). Lysates were centrifuged at 14,000 rpm for 20 min at 4°C, and the supernatants were used for immunoblotting. Protein concentrations were measured using the BCA protein assay kit (Pierce, 23225). The samples were diluted with 2X Laemmli sample buffer

(65.8 mM Tris-HCl, pH 6.8, 26.3% (w/v) glycerol, 2.1% SDS, 0.01% bromophenol blue, Bio-Rad, 161-0737) or in Lithium dodecyl sulfate (LDS) sample buffer (Invitrogen, NP0007) with a reducing reagent, followed by heating for 10 min at 70°C. Whole cell lysates were separated by sodium dodecyl sulfate (SDS)-polyacrylamide gel electrophoresis and transferred to polyvinylidene difluoride membranes (PVDF; Millipore, IPVH00010). Blocking was done using TBS-T (20 mM Tris-HCl, pH 7.5, 150 mM NaCl, and 0.05% (v/v) Tween 20) containing 1% BSA for 1 h at room temperature, and the membrane was incubated with antibodies diluted with the blocking solution for overnight at 4°C.

3.2.7 Histology and immunohistochemistry

Immunohistochemistry analysis was performed as described in the previous study [24]. Briefly, for histological analysis, embryos were fixed overnight at 4°C in 4% PFA in PBS, pH 7.4. Fixed embryos were gradually dehydrated with 70%, 90%, and 100% EtOH, followed by immersion in Neo-Clear (Millipore, 65351). Tissues were embedded in paraffin wax at 58°C and sectioned transversely or sagittally with 7 µm thickness. Paraffin-embedded slides were freshly treated with Neo-Clear twice for 10 min each, followed by gradual rehydration in EtOH (100%, 90%, 80%, and 70%; 6 min each) and water for 20 min. The slides were treated with blocking solution (5% normal goat serum and 0.2% Triton X-100 in PBS) for 1 h and incubated with primary antibodies and subsequently secondary antibodies.

3.2.8 Immunocytochemistry of cultured cells

Immunocytochemistry analysis was performed as described in the previous study [24]. Three 22

mm^2 coverslips per well were placed in 6-well plates, followed by incubation of diluted poly-L-lysine (1:10 in sterile deionized water; Sigma, P8920) for 30 min at room temperature. After washing once, the plate was exposed under UV radiation lamp overnight in a fume hood. Cells were cultured in the plate for further experiments. Cells were fixed in 4% PFA in PBS, for 30 min at room temperature. After washing twice with PBS, the cells were incubated for 1 h in blocking solution (5% normal goat serum and 0.3% Triton X-100 in 0.1 M PBS). After blocking, the samples were incubated with primary antibodies and subsequently secondary antibodies. Confocal images were taken with a Zeiss LSM 700 laser scanning confocal microscope equipped with Zeiss C-Apochromat 60x (1.2 NA) and 40x (1.2 NA) water immersion lens and analyzed using ZEN (black edition) 2012 SP5 software (Zeiss). Using the ZEN software, z-stacks of images covering the entire cell thickness were acquired and projected maximally. Image processing and annotation was done with Adobe Photoshop, Adobe Illustrator and Fiji software [103]. N-SIM images were taken with a Nikon Eclipse Ti inverted microscope (Nikon, Tokyo, Japan) equipped with a Nikon Apo TIRF 100x (1.49 NA) oil-immersion lens. The SIM images were reconstructed from the raw images through the Nikon NIS-element (ver. 3.22.10.).

3.2.9 TAT-FITC peptide internalization assay.

TAT Peptide incubation was performed as previously described with minor modification [104]. Cells were washed twice with PBS and preincubated in Opti-MEM (Gibco, 31985070) for 30 min, followed by TAT-FITC peptide treatment for the indicated times. Cells were fixed with 4% PFA for further experiments. Immunocytochemical processes were conducted as described above.

3.2.10 Horseradish peroxidase (HRP) uptake analysis.

HRP uptake analysis was performed as previously described with minor modification [105-107]. After washing cells with prewarmed culture media, cells were incubated in IMDM containing 5 mg/ml HRP and 1% BSA for 30 min. The uptake was stopped by washing cells five times with ice-cold PBS containing 0.1% BSA. After the final wash, cells were scraped into 1 ml of ice-cold PBS and pelleted at 800 x g for 3 min at 4°C. Cell pellet was lysed in 400 µl of ice-cold PBS containing 0.1% Triton X-100. The lysate was assayed for horseradish peroxidase activity. The enzyme assay was conducted in a 96-well microplate using 1-Step™ Ultra TMB-ELISA substrate solution as the chromogenic substrate. The reaction was started by adding 1 µl of the lysate to 100 µl of 1-Step™ Ultra TMB-ELISA substrate solution (Thermo Scientific, 34029). The reaction was conducted at room temperature for 20 min and stopped by adding 100 µl of 2 M H_2SO_4. Quantified by measuring OD_{425nm} in a Tecan microplate reader (Tecan, Sunrise™). Protein content was determined by the Pierce BCA assay (Thermo, 23227) according to the manufacturer’s instructions.

3.2.11 Immunoelectron microscopy

Immunoelectron microscopy analysis was performed as described in the previous study [24]. Briefly, cells were fixed in 2% PFA in PBS, pH 7.4, for 1 h and washed with PBS. Fixed cells were collected by scraping and resuspended in 3% gelatin. Cells embedded in gelatin were fixed again with 2% PFA for 15 min. After cryoprotected with 2.3 M sucrose with PVP solution overnight, samples were frozen in liquid nitrogen and were trimmed into 0.5 mm cubes. The frozen cell blocks were sectioned by cryo-microtome (Leica EM Crion) in 70 nm sections and collected on 200 mesh grids. The primary antibody was diluted in 0.1 M PBS with 0.5% BSA, 0.15% glycine according to the established condition for immunohistochemistry. A secondary antibody labelled with 12 nm gold beads (Jackson ImmunoResearch) was diluted to 1:25 before use. After immunostaining, sections were incubated with 2.5% glutaraldehyde for 10 min and with 2% Neutral UA acetate for 7 min. Sections were further processed with 4% uranyl acetate and methyl cellulose for contrasting and drying, respectively. After drying, samples were recorded using JEOL JEM1011 TEM with high resolution AMT digital camera (Peabody, MA).

3.2.12 Fractionation of proteins

Crude extracts were prepared by homogenizing +/+ and *UBR4*$^{-/-}$ MEFs in a hypotonic solution. Cellular proteins were separated into cytosolic (S150) and microsomal (P150) fractions using differential centrifugations and solubilization [24]. Cell were harvested from 5 of 15 cm dishes by trypsin-EDTA solution, followed by three-time of wash with PBS. Cell pellets were washed once with 5-packed cell volume (pcv) of hypotonic buffer (10 mM HEPES, pH7.9; 1.5 mM MgCl2; 10 mM KCl) supplemented with protease inhibitor cocktail (Sigma), 20 mM NaF, 10 mM sodium orthovanadate, and 1 mM DTT. Cells were suspended with 2-pcv of hypotonic buffer with supplements was added and cells were incubated for 10 min on ice. The expanded cells were homogenated by dounce homogenizer and a soluble fraction was collected after a centrifugation at 15,000 x g for 5 min. The pelleted fraction including nucleus, mitochondria, and plasma membranes, was solubilized with RIPA buffer (10 mM Tris-HCl, pH 7.4, 1% NP-40, 0.1% sodium deoxycholate, 0.1% SDS, 0.15 M NaCl, and 1 mM EDTA) to yield a soluble fraction (P15S) and an insoluble fraction (P15I). The soluble fraction after dounce homogenization and a centrifugation was further fractionated by an ultra-centrifugation at 150,000 x g for 1 h. The supernatant represents a cytosol (S150) and the pelleted membranes represent microsomes including ER (P150). Protein concentration was quantified, using the BCA protein assay and each fraction was kept frozen at -80°C until a use for SDS-PAGE.

3.2.13 EGFP-EEA1 and mRFP-RAB5 puncta analysis

HeLa cells were transiently transfected with either 1 μg/ml of EGFP-EEA1 or mRFP-RAB5 plasmids using Lipofectamine 3000 reagent (Invitrogen). Following the transfection, cells were cultured for 24 h and trypsinized for replating on coated slides. 24 h after replating, cells were treated with picolinic acid and fixed with 4% PFA for further experiments at the indicated times. After PBS washing, immunocytochemical processes were conducted as described above.

3.2.14 Pull-down assay of UBR4 and calmodulin

Pulldown assay was performed as previously described with minor modification [8]. HEK293 Cells were transfected with UBR4-GFP and GUS-GFP (GUS, β-glucuronidase) plasmids using Lipofectamine LTX and Plus reagent (Invitrogen) and harvested 48 h after transfection. GUS-GFP was used as a transfection control. Cells were lysed in 1% Nonidet-P40 (NP-40), 0.15 M NaCl, 1 mM EDTA, 10 mM Tris-HCl (pH 7.5). The lysates were incubated with anti-GFP biotin conjugated antibody in binding buffer A (0.1% Nonidet P-40, 10% glycerol, 0.15 M KCl, and 20 mM HEPES, pH 7.9) and mixed with streptavidin-sepharose beads (Amersham Bioscience). The beads were pelleted by centrifugation at 2,400 x g for 30 s, washed three times with binding buffer A and resuspended in SDS-PAGE sample buffer, and heated and analyzed by immunoblotting with anti-calmodulin antibody.

3.2.15 Synthesis of biotinylation of picolinic acid

Picolinic acid was biotin-conjugated using EZ-link pentylamine-Biotin (Thermo, 21345). 0.18 mM picolinic acid was added to the mixture including 0.22 mM *N*-(3-dimethylaminopropyl)-*N′*-ethylcarbodiimide hydrochloride (EDCI.HCl), 6.2 mM hydroxybenzotriazole (HOBt), 0.54 mM N,N-diisopropylethylamine (DIPEA), and 2 ml DMF. After 10 min, 0.15 mM 5-(biotinamido)pentylamine was added to the mixture with continued stirring. The reaction was quenched by the addition of water and then ethyl acetate was added. It was washed with saturated citric acid to eliminate unreacted amine derivatives followed by sequential washing with sodium bicarbonate to remove unreacted acid derivative and with brine. The combined organic layers were dried over anhydrous Na_2SO_4 and concentrated under vacuum. The crude residue was purified using silica gel column chromatography (methanol/dichloro methane = 1:9) to yield the biotinylated picolinic acid as white solid. The structure of the product biotinylated picolinic acid was confirmed with LC-MS (Figure 14). Its mass spectrum revealed a molecular ion peak at 434.32 $[M+H]^+$ corresponding to the molecular formula $C_{21}H_{31}N_5O_3S$ confirms the structure of biotinylated picolinic acid.

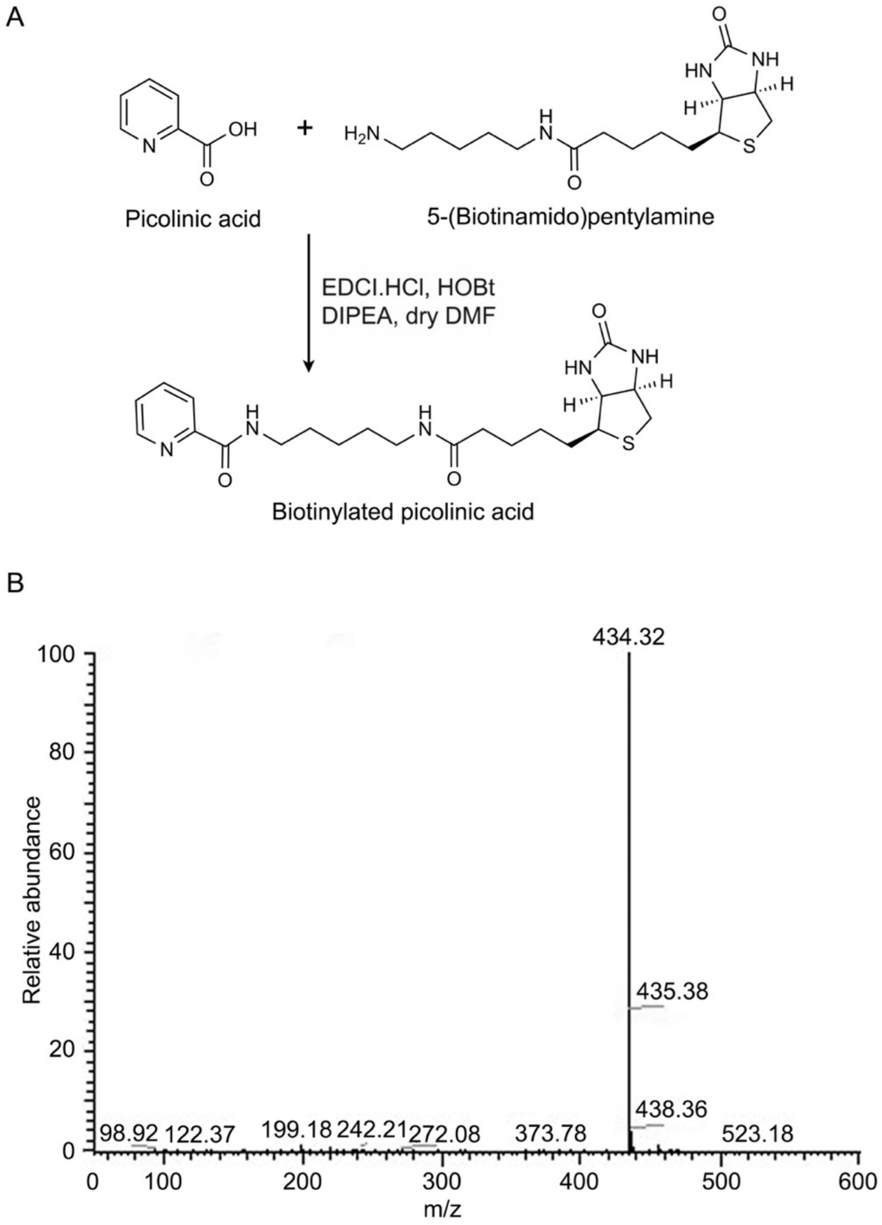

Figure 14: Synthesis of biotinylated picolinic acid.

(A) Schematic illustration for synthesis of biotinylated picolinic acid. (B) Verification of picolinic acid biotinylation using LC-MS. Synthesis was conducted by Srinivasrao Ganipisetti.

3.2.16 X-peptide and biotinylated picolinic acid pull-down assay

The X-peptide and biotinylated picolinic acid pull-down assays were carried out as previously described with minor modification [6]. We used a set of 12-mer X-nsP4 peptides (X-IFSTIEGRTYK–biotin) bearing N-terminal Arg (type 1), Phe (type 2), and Gly (stabilizing control) residues, which is known as a N-end rule substrate. For cross-linking with resin, the biotin-conjugated picolinic acid and peptides were mixed with high capacity streptavidin agarose resin (Thermo, 20361) with a ratio of 0.5 mg peptide per 1 ml settled resin and incubated on rotator at 4°C for overnight. After washing 5 times with PBS, the peptide-beads conjugates were diluted with PBS at 1:1 ratio. To prepare protein extracts, cells were collected by centrifugation and lysed by freezing and thawing at least ten times in hypotonic buffer (10 mM KCl, 1.5 mM $MgCl_2$, and 10 mM HEPES, pH 7.9) with a protease inhibitor mix (Sigma, P8340). After spinning down with centrifugation in 12,000 rpm at 4°C for 15 min, proteins were quantified using BCA protein assay kit (23227, Thermo). Total proteins (300 μg) diluted in 250 μl binding buffer (0.05% Tween-20, 10% glycerol, 0.2 M KCl, and 20 mM HEPES, pH 7.9) were mixed with 50 μl peptide-bead resin and incubated at 4°C for overnight on a rotator. The protein-bound beads were collected by centrifugation at 5,000 rpm for 1 min and washed five times with binding buffer. The beads were resuspended in 25 μl SDS sample buffer, heated at 70°C for 10 min, and subjected to SDS-PAGE and immunoblotting.

3.2.17 Labeling of epidermal growth factor (EGF) and transferrin with fluorescence

Labeling with EGF and transferrin were performed as previously described with minor modification [108]. Cells were serum-starved for 1 h and stimulated with 1 μg/ml EGF conjugated with Alexa Fluor 555 (Invitrogen, E35350) or 0.5 μg/ml transferrin with Alexa Fluor 488 (Invitrogen, T13342) in DMEM-HEPES buffer containing 1% BSA on ice for 1 h and washed with cold PBS. The samples were incubated in pre-warmed media for indicated times, followed by 4% PFA fixation at the appropriate time point. After fixation, we followed the same procedures as we mentioned above in immunocytochemistry.

3.2.18 EGF-biotin pulldown assay

Labeling with EGF was performed as previously described with minor modification [108]. Cells were serum-starved for 1 h and stimulated with 1 μg/ml EGF conjugated with biotin (Invitrogen, E3477) in DMEM-HEPES buffer containing 1% BSA on ice for 1 h and washed with cold PBS. The samples were incubated in pre-warmed media for indicated times, followed by lysis. The internalized EGF-biotin was analyzed by dot blotting. For dot blot experiments, isolated EGF-biotin samples were spotted onto a nitrocellulose membrane and incubated with the anti-biotin HRP conjugated secondary antibody.

3.2.19 Statistical analysis

All numerical data are presented as means ± SEM or mean percentages ± SEM. Western blots shown are representative of three or more independent experiments. Comparisons among treatment groups were performed with one-way analysis of variance (ANOVA) and Tukey test or Dunnet's multiple comparison as a post hoc comparison. Instances involving only two comparisons were evaluated with two-tailed t-test. Statistical significance was accepted if the null hypothesis was rejected with $p < 0.05$. All statistical analyses were determined using Prism 7.0a software (GraphPad, La Jolla, CA).

3.3 EXPERIMENTAL RESULTS

3.3.1 The EEA1$^+$ early endosome is impaired in the YS and embryos lacking mouse UBR4.

We have previously found that *UBR4*$^{-/-}$ mouse embryos die at E9.5-10.5 associated with vascular defects in the YS [24]. At this stage, embryos cannot synthesize amino acids *de novo* and, thus, obtain amino acids by breaking down endocytosed proteins in the YS (Figure 15A) [109]. These extracellular protein cargoes (e.g., albumins), provided by pregnant mothers, are endocytosed by the YS and sequestered and degraded by EEA1$^+$ early endosomes [71, 110]. The cargoes within early endosomes are further degraded as early endosomes are fused with autophagosomes to generate amphisomes and, subsequently, by lysosomal hydrolases [109]. To determine the role of

UBR4 in endosomal pathways in animals, we examined the localization of UBR4 on the cross sections of E9.5 +/+ and *UBR4*$^{-/-}$ YSs and embryonic bodies. Immunostaining analysis showed that UBR4 is prominently expressed in the YS endoderm, a specialized tissue enriched in endosomal proteolysis (Figure 15B and C). UBR4 signals formed cytosolic puncta that colocalized with EEA1^{+} early endosomes (Figure 15C). UBR4^{+}EEA1^{+} punctate signals were more prominent in the YS endoderm as compared with the YS mesoderm (Figure 15C). Within the YS endoderm, both UBR4 and EEA1 signals were enriched in the cytosol's apical side and near lysosomal vacuoles. A significant portion of UBR4^{+}EEA1^{+} puncta distributed along the axis from the plasma membrane to apical vacuoles (Figure 15C). Moreover, the EEA1 staining was significantly reduced in the YS of *UBR4*$^{-/-}$ at E9.5 (Figure 15D).

To further validate these results in embryonic tissues, we immunostained EEA1 on the cross sections of +/+ and *UBR4*$^{-/-}$ mouse embryonic bodies at E9.5. Whereas EEA1 was detected as punctate structures in various tissues of +/+ embryos, such signals were markedly down-regulated and disorganized in various tissues of *UBR4*$^{-/-}$ embryos, including the neural tube and paraximal mesoderm of neuronal tissues (Figure 15E). These results collectively suggest that UBR4 plays a role in the biogenesis of early endosomes in YS and various tissues of mouse embryos.

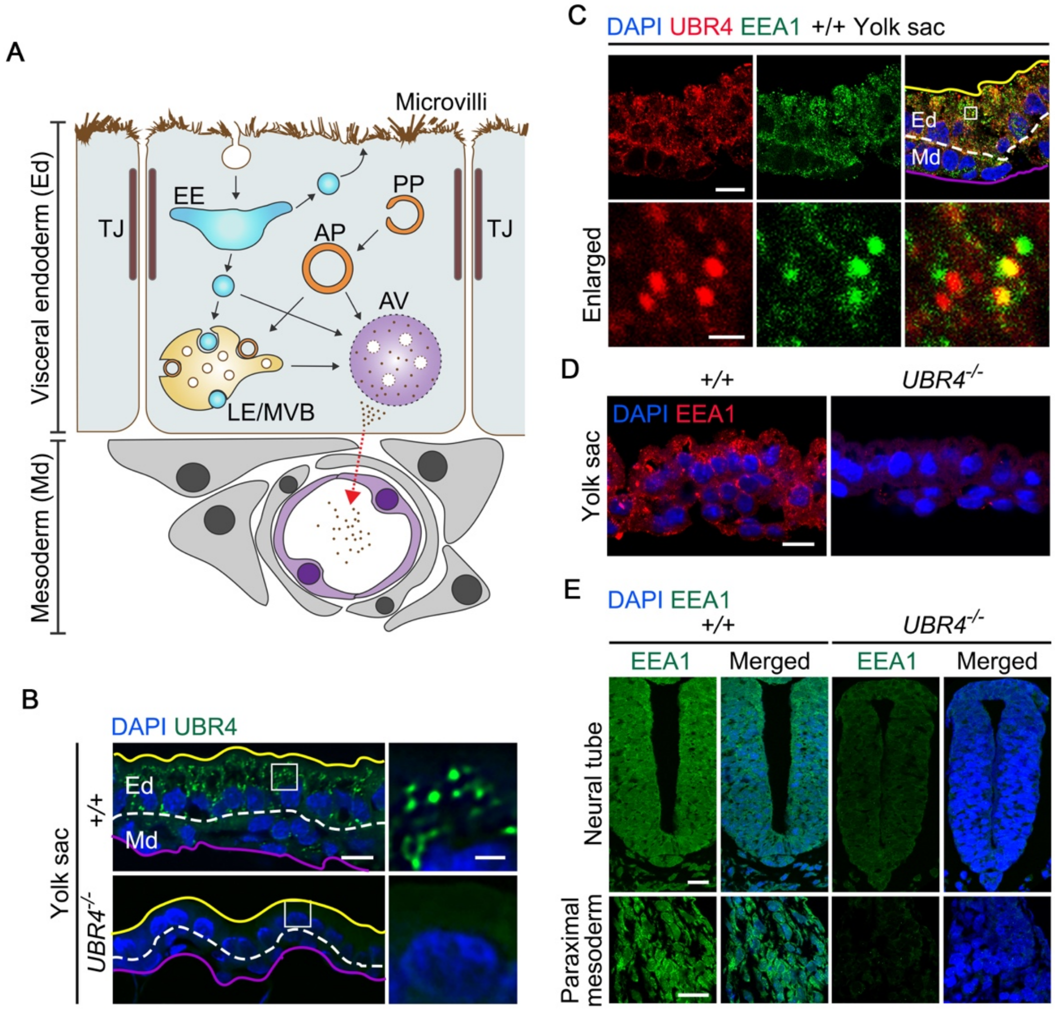

Figure 15: UBR4 regulates endosomal pathways in mouse YS and embryos.

(A) Schematic illustration of the structure and function of the visceral YS of murine embryos. The visceral YS of mouse embryos at E9.5 is composed of two developmentally distinct layers, visceral endoderm (Ed) and mesoderm (Md). AP, autophagosome; AV, apical vacuole; EE, early endosome; LE, late endosome; MVB, multivesicular body; PP; phagophore; TJ, tight junction. (B) Immunostaining analysis of UBR4 on cross sections of +/+ and *UBR4*$^{-/-}$ YS at E9.5. The dotted line represents two distinct layers of the visceral YS (scale bar = 10 μm). Enlarged views show the area indicated by rectangles (scale bar = 1 μm). Ed, endodermal layer; Md, mesodermal layer. (C) Immunostaining analysis of UBR4 and EEA1 on the cross sections of +/+ YS at E9.5 (scale bar = 10 μm). Enlarged views show the areas indicated by rectangles (scale bar = 1 μm). Ed, endodermal layer; Md, mesodermal layer. (D) Immunostaining analysis of EEA1 on the cross sections of +/+ and *UBR4*$^{-/-}$ YS at E9.5. UBR4 is required for the formation of EEA1^{+} early endosomes in YS (scale bar = 10 μm). (E) Immunostaining of EEA1 on +/+ and *UBR4*$^{-/-}$ embryonic tissues, including neural tube and paraximal mesoderm (scale bar = 20 μm).

3.3.2 UBR4 is dispensible for the internalization of extracellular ligands.

To characterize the rle of UBR4 in endosomal pathways, we compared the internalization of extracellular ligands in +/+ and *UBR4*$^{-/-}$ MEFs by measuring the uptake of horseradish peroxidase (HRP), a fluid-phase marker for bulk endocytosis [105-107]. Quantitation analyses showed that *UBR4*$^{-/-}$ MEFs contained a comparable amount of internalized HRP relative to +/+ MEFs (Figure 16A). As an alternative way to monitor the endocytosis and visualize early endosomes containing endocytosed external cargoes, we treated FITC conjugated-TAT peptide, which is derived from the transactivator of transcription (TAT) of human immunodeficiency virus (HIV). TAT peptide binds to various cellular receptors and internalized through endosomal pathway. Upon internalization, TAT crosses the endosomal membrane to enter the cytosol [104, 111, 112]. Fluorescence assay showed that TAT-FITC was endocytosed and made punctate structures in +/+ MEFs and both number and size were gradually increased in timely manner (2 fold and 1.5 fold of +/+ 10 min, respectively; Figure 16B-D). Contrary to +/+ MEFs, the size of TAT^{+} endosomal vesicles in *UBR4*$^{-/-}$ MEFs had remained arrested as 50% of +/+ at 20 min (*** $p < 0.001$; Figure 16B and C). Even though *UBR4*$^{-/-}$ MEF had smaller TAT^{+} endosomes, it contained an excessive number of TAT^{+} puncta, compared to that of +/+ MEFs (6 fold of +/+ 20 min, *** $p < 0.001$; Figure 16D). The result suggests that comparable amount of TAT was endocytosed in *UBR4*$^{-/-}$ MEFs. Collectively, these results show that UBR4 is largely dispensible for the internalization of extracellular ligands but plays a role in early endosomal maturation.

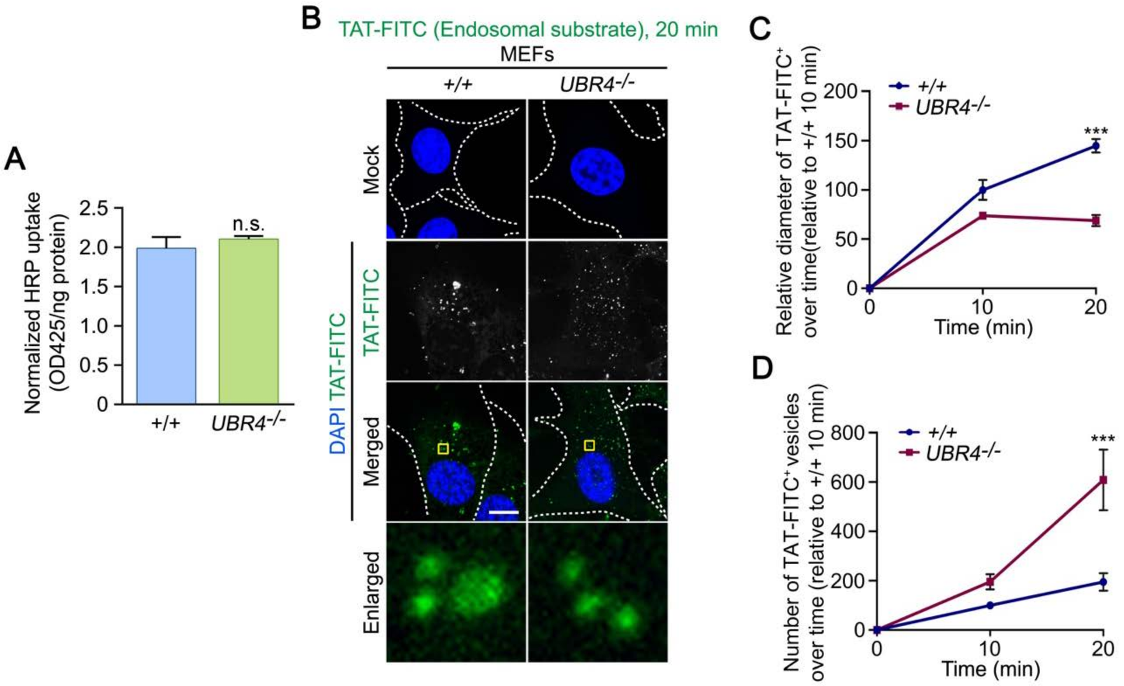

Figure 16: UBR4 is dispensible for the internalization of external cargoes.

(A) HRP uptake analysis in +/+ and *UBR4*$^{-/-}$ MEF cells. Cells were treated with prewarmed serum-free IMDM containing 5 mg/ml HRP and 1% BSA. Normalized OD_{425nm} measurements by the protein amount determined by the BCA assay. n.s., not significant. Representative of three biological replicates. Statistical significance was determined using two-tailed t-test. (B) Immunofluorescence analysis of +/+ and *UBR4*$^{-/-}$ MEFs treated with the endosomal substrate FITC conjugated TAT (sacle bar = 10 µm) during the indicated times. (C and D) Quantification of B, representing the diameter and number of TAT-FITC$^+$ vesicles, respectively. ***$p < 0.001$ compared to +/+ MEF cells (n = 4-8 in each group). Data are presented as mean percentage ± SEM of +/+ at 10 min. Statistical significance was determined using one-way analysis of variance (ANOVA) and Sidak test as a post hoc comparison.

3.3.3 UBR4 modulates the biogenesis of early endosomes.

To determine the function of UBR4 in endosomal proteolysis and endocytosis, we further examined the biogenesis of early endosomes in +/+ and *UBR4*$^{-/-}$ MEFs. Immunostaining analysis visualized EEA1$^+$ puncta with diameters of 200-500 nm throughout the cytosol of +/+ MEFs (Figure 17A and B). In contrast, UBR4 deficiency *UBR4*$^{-/-}$ MEFs contained a significantly reduced number of large early endosomes (Figure 17A). We systematically clarified the descriptions of endosomes based on other studies as well as our own additional quantitation analyses (Figure 17C). Early endosome is heterogenous in terms of size and morphology because it constitutes of thin tubular extensions (~60 nm diameter) and large vesicles (~400 nm diameter) [113]. Thus, we separated three categories and defined a large vesicle that is greater than 500 nm as a matured endosome (Figure 17C). Quantitative analysis showed that UBR4 deficiency decreased the number

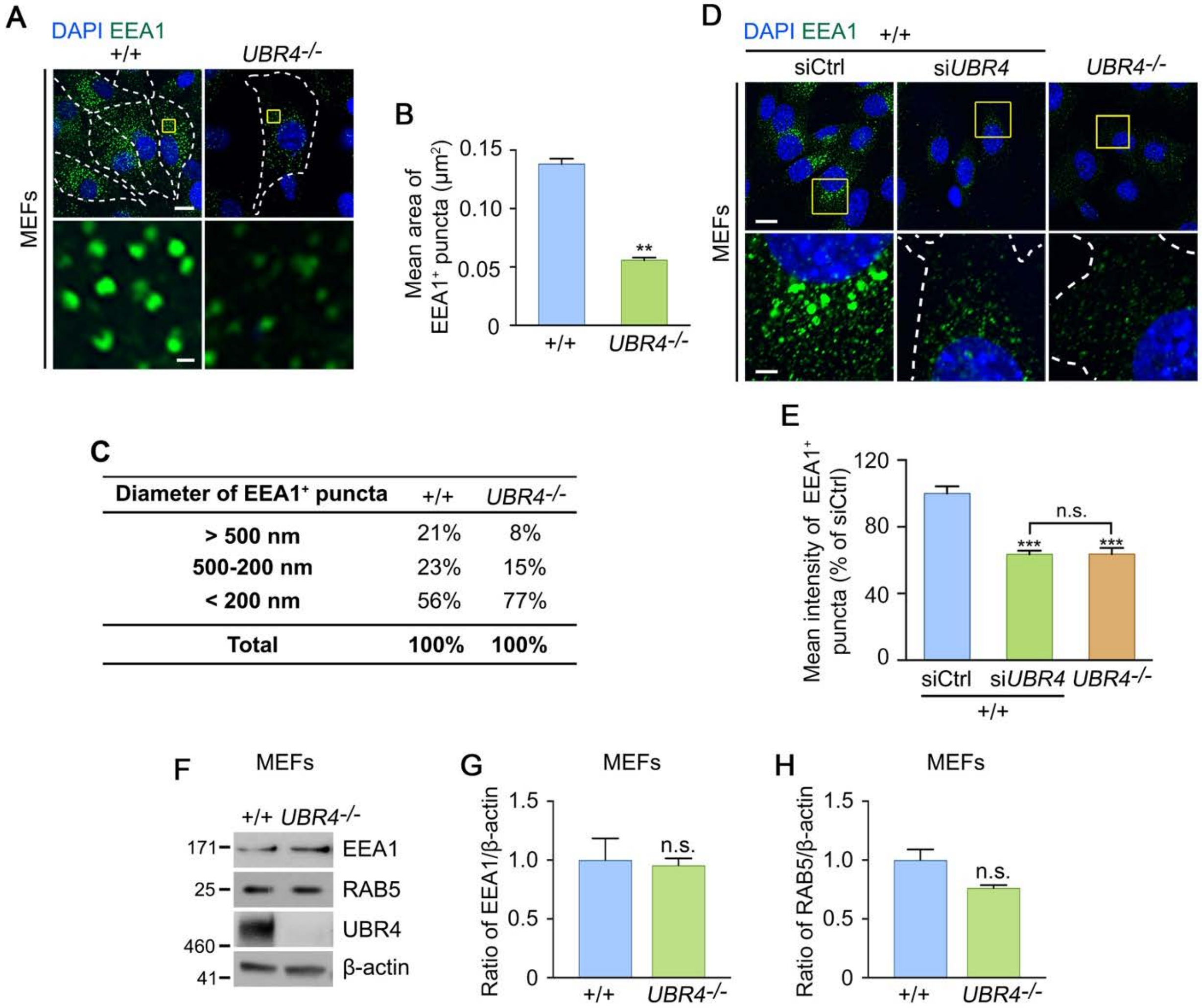

C

Diameter of EEA1+ puncta	+/+	*UBR4-/-*
> 500 nm	21%	8%
500-200 nm	23%	15%
< 200 nm	56%	77%
Total	**100%**	**100%**

Figure 17: Down-regulated EEA1$^+$ endosomal biogenesis by UBR4 deficiency.

(A) Immunostaining of EEA1 on +/+ and *UBR4*$^{-/-}$ MEFs. White dotted lines delineate the cell boundary (scale bar = 15 μm). Enlarged views shows arears indicated by yellow rectangles (scale bar = 2 μm). (B) Quantification of A, showing the mean areas of EEA1^{+} puncta (μm^{2}). ***$p < 0.0001$ compared to +/+ MEF cells (n = 3,057 and n = 3,455 for +/+ and *UBR4*$^{-/-}$ MEFs, respectively). Data are presented as mean ± SEM. Statistical significance was determined using two-tailed t-test. (C) Classification of EEA1^{+} puncta within three divisions depends on their diameters from B. (D) Immunostaining of EEA1 on siCtrl- and si*UBR4*-treated +/+ and *UBR4*$^{-/-}$ MEFs. The number of EEA1^{+} EE puncta was significantly down-regulated in UBR4 knockdown as well as knockout MEFs (scale bar = 15 μm). Enlarged views show the areas indicated by yellow rectangles. White dotted lines delineate the cell boundary (scale bar = 1 μm). (E) Quantification of D, showing the mean intensity of EEA1^{+} puncta (% of siCtrl). n.s., not significant; ***$p < 0.0001$ compared to siCtrl-treated +/+ MEF cells (n = 4 for each group). Data are presented as mean percentage ± SEM of siCtrl-treated +/+ MEF cells. Statistical significance was determined using one-way ANOVA and Tukey test as a post hoc comparison. (F) Immunoblotting of EEA1 and RAB5, and UBR4 in +/+ and *UBR4*$^{-/-}$ MEFs. β-Actin was probed for loading control. (G and H) Quantification of F, showing the ratio of EEA1 and RAB5 amounts relative to β-actin amounts, respectively. n.s., not significant. Representative of three biological replicates. Statistical significance was determined using two-tailed t-test. Panels F-H were conducted by Yoon Jee Lee.

of matured EEA1^{+} endosomes to 38% relative to +/+ MEF cell (Figure 17C). Such a down-regulation of EEA1^{+} early endosomes was readily reproduced by transiently depleting UBR4 using siRNA (Figure 17D and E). Despite the down-regulation of EEA1^{+} puncta maturation, *UBR4*$^{-/-}$ MEFs contained a normal level of EEA1 as determined by immunoblotting analyses (Figure 17F-H).

Moreover, the overexpression of EEA1 in *UBR4*$^{-/-}$ MEFs did not restore the defect, suggesting that the failure to form EEA1^{+} endosomes is not caused by EEA1 insufficiency (Figure 18A). To further characterize the role of UBR4 in early endosomal formation, we performed immunostaining analyses using RAB5 which is associated with endocytic vesicles and early endosomes and replaced with RAB7 in late endosomes [114]. Consistent with the results with EEA1, *UBR4*$^{-/-}$ MEFs were notably impaired in the formation of RAB5^{+} early endosomes (Figure 18B).

Next, we asked whether exogenous expression of UBR4 would rescue the reduced size of

EEA1$^+$ and RAB5$^+$ early endosomes in *UBR4*$^{-/-}$ MEFs. The overexpression of UBR4-GFP restored the ability of *UBR4*$^{-/-}$ MEFs to form EEA1$^+$ puncta (Figure 18C and D). Similar to the restored EEA1 puncta formation, transiently overexpressed UBR4-GFP in *UBR4*$^{-/-}$ MEFs readily rescued the biogenesis of RAB5$^+$ early endosomes (Figure 18E and F). Collectively, these data suggest that UBR4-loss impairs the biogenesis of early endosomes.

We have previous identified a set of N-recognins (UBR1, UBR2, UBR4, and UBR5) characterized by the UBR box [8]. Amongst these, UBR1 and UBR2 have been implicated in the UPS-linked N-end rule pathway [10, 98]. To determine whether the aforesaid role in endosomal pathways is confined to UBR4 amongst N-recognins, we performed immunostaining analyses. *UBR1*$^{-/-}$*UBR2*$^{-/-}$ MEFs normally contained EEA1$^+$ as well as RAB5$^+$ early endosomes as compared with +/+ MEFs (Figure 19). These results suggest that UBR4 may be a designated N-recognin that controls endosomal proteolysis.

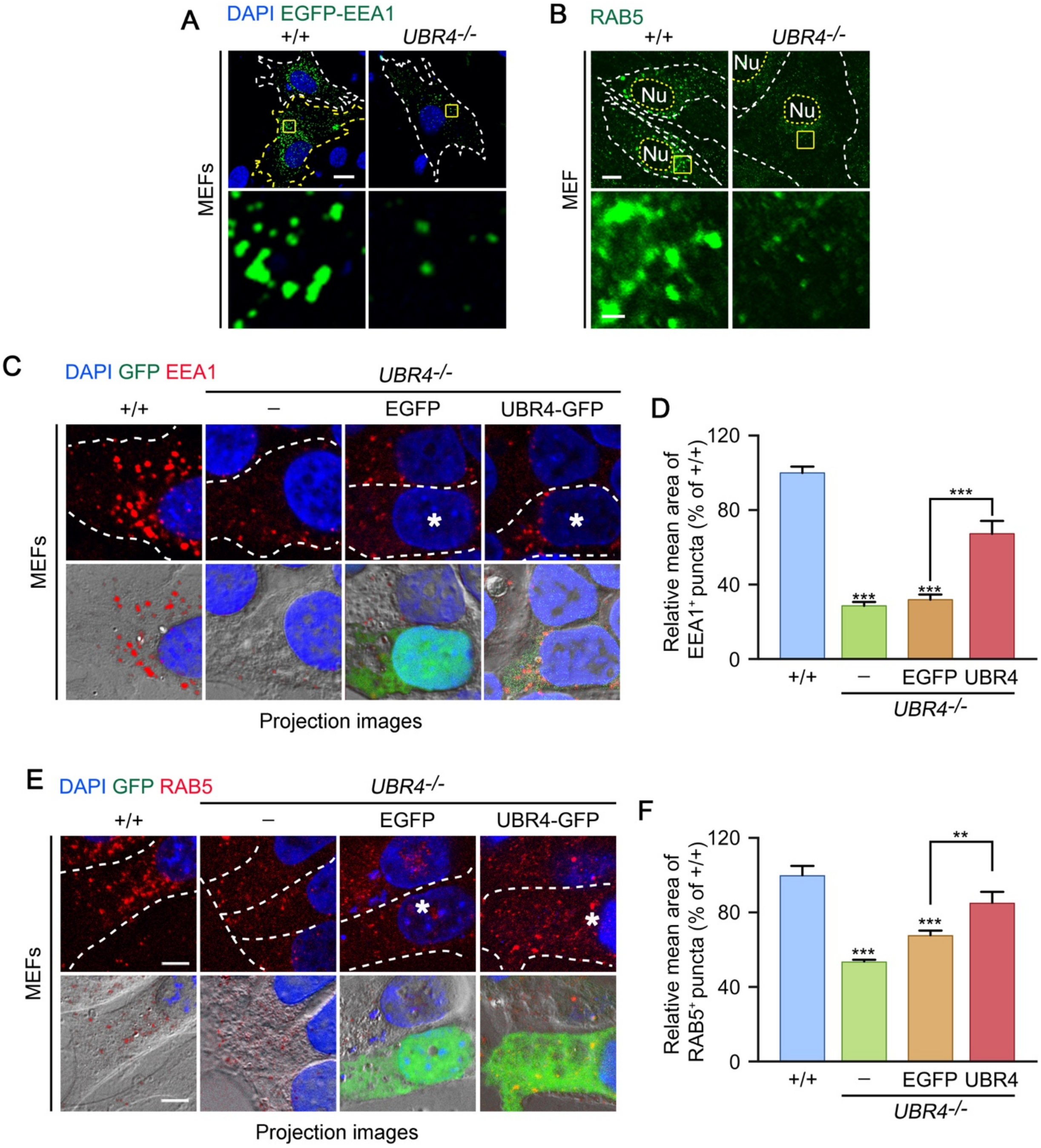

Figure 18: UBR4 is required for the biogenesis of the EEs.

(A) +/+ and *UBR4*$^{-/-}$ MEFs were transiently transfected with EGFP-EEA1 for 48 h and fixed with 4% PFA for further analysis. White and yellow dotted lines delineate the cell boundary (scale bar = 10 μm). Enlarged views show the areas indicated by yellow rectangles (scale bar = 1 μm). (B) Immunostaining of RAB5 on +/+ and *UBR4*$^{-/-}$ MEFs. The number of RAB5^{+} early endosomal puncta was notably decreased in *UBR4*$^{-/-}$ MEFs (scale bar = 10 μm). Enlarged views show the area indicated by yellow rectangles. White dotted lines delineate the cell boundary (scale bar = 1.5 μm). (C) Immunostaining analysis of EEA1 on +/+ and *UBR4*$^{-/-}$ MEFs transiently transfected with plasmids encoding EGFP or UBR4-GFP (1.0 μg/ml). After 24 h from transfection, cells were fixed with 4% PFA for further process (scale bar = 5 μm). Transfected cells were indicated by an asterisk (*). (D) Quantification of C, showing the relative mean area of EEA1^{+} puncta (% of +/+). The formation of EEA1^{+} puncta was rescued by transient supplement of UBR4 for 24 h. ***$p < 0.001$ compared to +/+ MEF cell (n = 15-35 in each group). Data are presented as mean percentage ± SEM of +/+ MEF cell. Statistical significance was determined using one-way ANOVA and Tukey test as a post hoc comparison. (E) Immunostaining analysis of RAB5 on +/+ and *UBR4*$^{-/-}$ MEFs transiently transfected with plasmids encoding EGFP or UBR4-GFP (1.0 μg/ml). At 24 h after transfection, cells were fixed with 4% PFA for further process (scale bar = 5 μm). Transfected cells were indicated by an asterisk (*). (F) Quantification of E, showing the relative mean area of RAB5^{+} puncta (% of +/+). The formation of RAB5^{+} puncta was rescued by transient supplement of UBR4 for 24 h. ***$p < 0.001$ compared to +/+ MEF cells and **$p = 0.008$ compared to EGFP-transfected *UBR4*$^{-/-/}$ MEF cells (n = 16-25 in each group). Data are presented as mean percentage ± SEM of +/+ MEF cells. Statistical significance was determined using one-way ANOVA and Tukey test as a post hoc comparison.

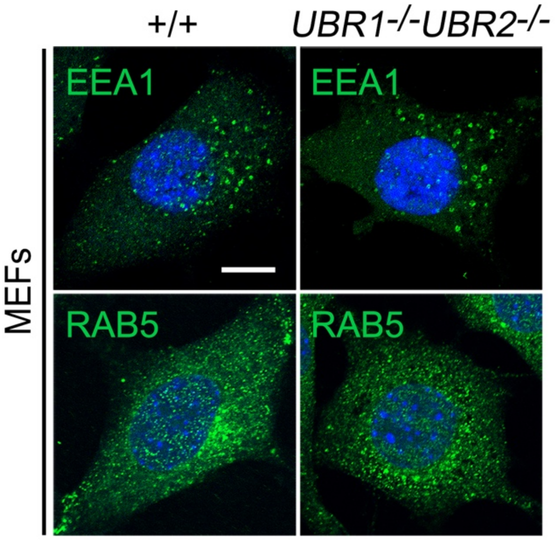

Figure 19: The normal formation of EEA1^{+} and RAB5^{+} early endosomes in *UBR1*$^{-/-}$*UBR2*$^{-/-}$ MEF cell. Immunostaining of EEA1 and RAB5 on +/+ and *UBR1*$^{-/-}$*UBR2*$^{-/-}$ MEFs. There were no significant differences on the intensities of EEA1 and RAB5 in *UBR1*$^{-/-}$*UBR2*$^{-/-}$ MEF as compared with those of +/+ MEF (scale bar = 10 μm).

3.3.4 UBR4 is associated with the EEA1$^+$ early endosome through its interaction with Ca^{2+}-calmodulin.

We examined the intracellular localization of UBR4 in comparison with endosomal markers. Immunostaining analysis using super-resolution confocal microscope (N-SIM) with a resolution of 100 nm showed that UBR4 stainings formed punctate structures with sizes of 150 x 300 nm (Figure 20A). Some UBR4$^+$ signals were juxtaposed to RAB5$^+$ endosomes in a way that tethers

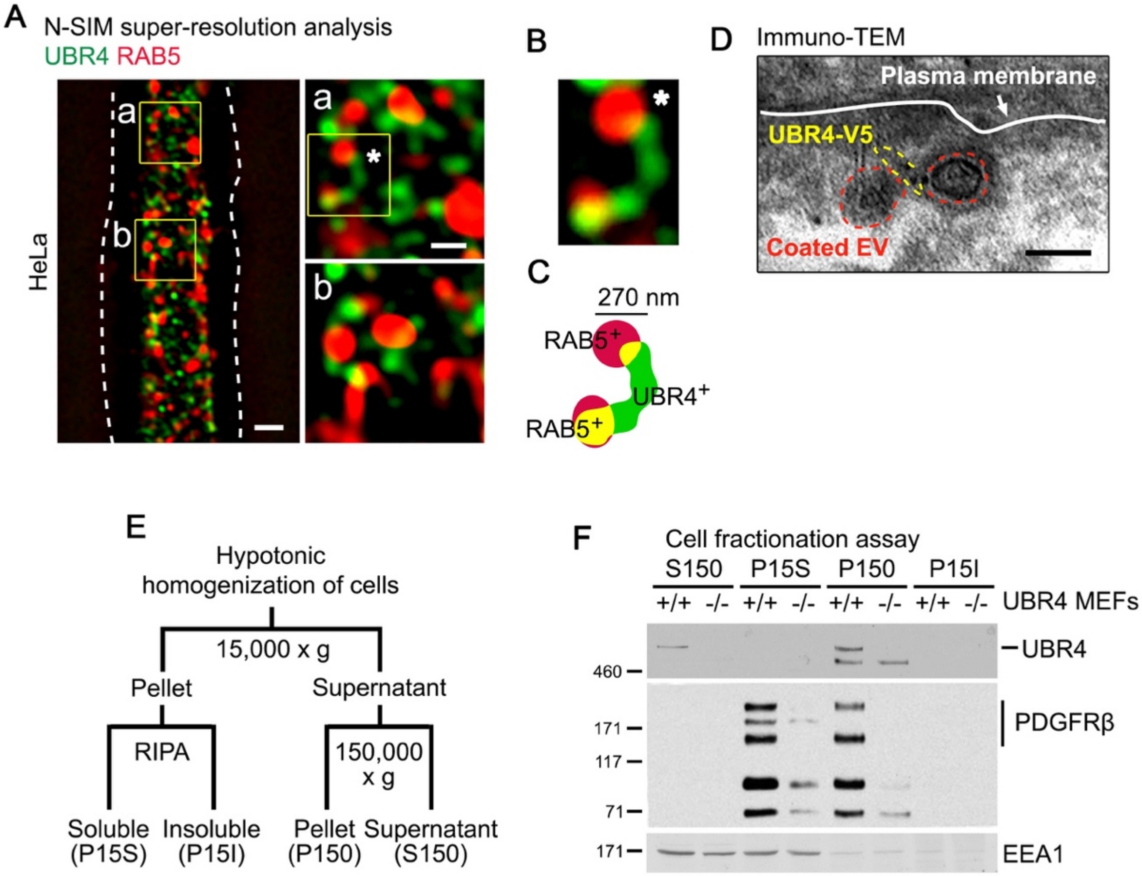

Figure 20: UBR4 is recruited to endosomal vesicles.

(A) Representative images captured by an N-SIM super-resolution microscope showing immunostaining for the subcellular localization of UBR4 and RAB5 in HeLa cells. White dotted line delineates the cell boundary (scale bar = 1.5 μm). Enlarged views show the areas 'a' and 'b' indicated by yellow rectangles (scale bar = 400 nm). (B) A magnified micrograph corresponding to the box within the region 'a', which is indicated by an asterisk (*). (C) Schematic illustration of UBR4$^+$RAB5$^+$ punctate structure corresponding to B. UBR4 is located between RAB5$^+$ primary endocytic vesicles. (D) Transmission electron microscopy (TEM) using a 12 nm immunogold labelled secondary antibody against V5 in HEK293 stably expressing UBR4V5. White line delineates the plasma membrane, and yellow dotted line represents the UBR4V5$^+$ vesicular structure. Red dotted line shows two distinct endocytic vesicles (scale bar = 100 nm). (E) Schematic diagram of cell fraction assay. (F) Cell fraction assays using +/+ and *UBR4*$^{-/-}$ MEFs retrieved UBR4 mainly from plasma membrane-associated and cytosolic vesicular fractions. Cellular proteins were separated into cytosolic and microsomal fractions using differential centrifugations and solubilization. Panel F was conducted by Takafumi Tasaki.

two RAB5$^+$ endosomes (Figure 20B and C). As an alternative method to determine the localization of UBR4 on endosomal vesicles, we performed immunoelectron microscopy using UBR4V5 stably expressing HEK293 cells. Immunogold labeled UBR4 molecules also were attached with two endosomal vesicles (Figure 20D). Given that UBR4 is partially associated with two endosomal vesicles, UBR4 can be mediate the process of early endosomal maturation. To further support this speculation, we separated +/+ and *UBR4*$^{-/-}$ MEFs into the soluble cytosol (S150), cells membranes (P15S), and cytosolic vesicles (P150) using differential centrifugation (Figure 20E). UBR4 was mainly retrieved from the soluble cytosol as well as cytosolic vesicles. These results suggest that some part of UBR4 is associated with endosomal membranes (Figure 20F).

Next, we searched for the proteins that link UBR4 to endocytic vesicles. During the maturation of endocytic vesicles, Ca^{2+}-bound calmodulin (CaM) is associated with the endocytic vesicles and induces the conformational change of EEA1, facilitating the homotypic fusion of two primary endocytic vesicles into a matured early endosome [115, 116]. To date, little is known about how CaM activity is regulated during endosome biogenesis. Given the association of UBR4 with endosomes, we paid attention to a previous study in which UBR4 was identified as a CaM-binding protein, although its meaning remains unknown [50]. To validate this finding, we performed *in vitro* interaction assays using UBR4-GFP stably expressed in HEK293 cells. The results showed that UBR4 indeed bound calmodulin and that their interaction was disrupted when Ca^{2+} was chelated (Figure 21A). We therefore examined the colocalization of UBR4 and CaM on

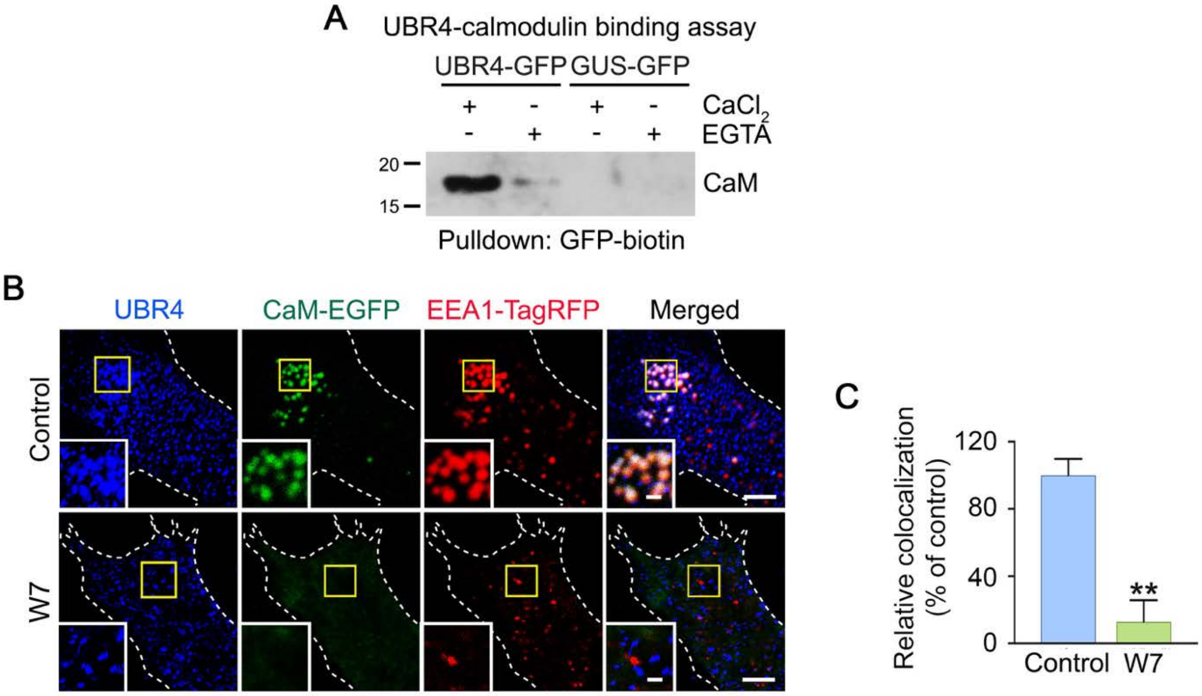

Figure 21: UBR4 is recruited to $EEA1^+$ EEs through interaction with Ca^{2+}-bound calmodulin.

(A) Calcium-dependent binding of calmodulin (CaM) to UBR4. HEK293 cells were transiently transfected with UBR4-GFP and GUS-GFP plasmids and lysed for the pull-down assay. Western blot analysis was used to determine the presence of calmodulin in the complexes. GUS-GFP plasmid was used as a transfection control.(B) Immunofluorescence assay of UBR4 in comparison with calmodulin and EEA1. HeLa cells transiently expressing calmodulin-EGFP and EEA1-TagRFP were treated with the CaM inhibitor W7 for 15 min (scale bar = 3 μm). Enlarged views show the areas indicated by yellow rectangles (scale bar = 1 μm). (C) Quantification of B, showing the relative colocalization frequency between $UBR4^+$- and $EEA1^+$-puncta (% of control). $^{**}p = 0.0013$ compared to DMSO-treated HeLa cells ($n = 4$ for control and $n = 5$ for W7-treated group). Data are presented as mean percentage ± SEM of DMSO-treated HeLa cells. Statistical significance was determined using two-tailed t-test. Panel A was conducted by Takafumi Tasaki.

the early endosomes in HeLa cells transiently expressing CaM-EGFP and EEA1-TagRFP. Co-immunostaining analyses showed that virtually most of CaM^+EEA1^+ puncta were also positive for UBR4 (Figure 21B). When cells were treated with W7, a CaM inhibitor, for 15 min, UBR4 as well as CaM were dissociated from $EEA1^+$ puncta (Figure 21B and C). These results suggest that UBR4 is associated with early endosomes in part through its interaction with Ca^{2+}-CaM.

3.3.5 UBR4 regulates endosomal trafficking.

To determine the role of UBR4 in endosomal trafficking, we treated +/+ and *UBR4*$^{-/-}$ MEFs with Alexa Fluor 555-conjugated EGF (epidermal growth factor) and monitored the intracellular trafficking of the EGF-EGFR complex using co-immunofluorescence analyses. By 10 min, EGF^+EGFR^+ endosomes in +/+ MEFs were distributed across the cytosol, from the plasma membrane to the peri-nuclear region (Figure 22B). By 20 min, most EGF^+EGFR^+ endosomes migrated to the peri-nuclear region, indicative of endosomal trafficking. By sharp contrast, *UBR4*$^{-/-}$ MEFs contained a markedly decreased number of EGF^+EGFR^+ signals which appeared to be arrested at endocytic vesicles based on their morphology and sizes (Figure 22B). As an alternative assay, we quantified the intracellular localization of EGF^+EGFR^+ endosomes along the plasma membrane-nucleus axis at 10 min and 20 min (Figure 22C). Whereas most of the EGF^+EGFR^+ endosomes in +/+ MEFs migrated to the peri-nuclear region, those in *UBR4*$^{-/-}$ MEFs stayed near the plasma membrane (Figure 22C-E). Despite impaired endosomal trafficking, *UBR4*$^{-/-}$ MEFs retained the cytoskeleton structures as determined by immunostaining analyses of actin filaments and microtubules (Figure 23). These results suggest that UBR4 is required for endosomal trafficking of ligand-receptor complexes internalized from the plasma membrane.

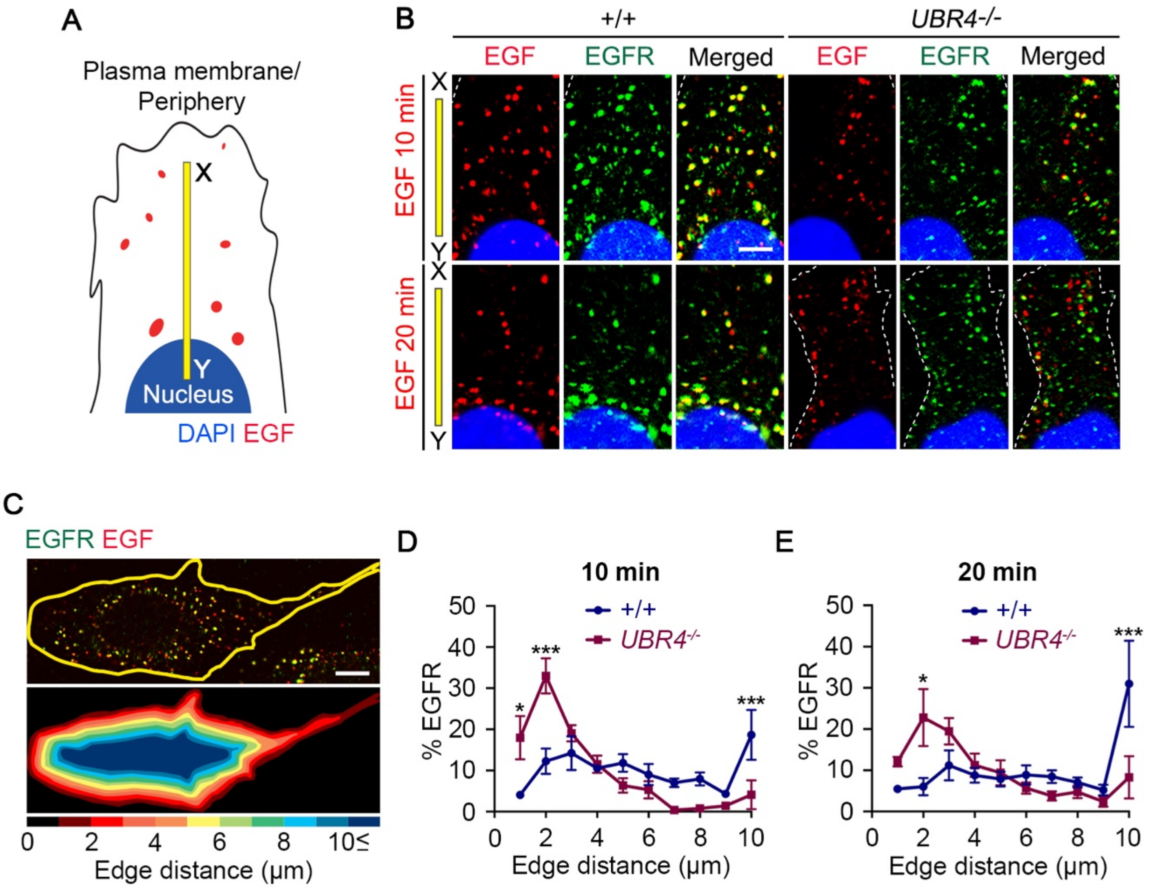

Figure 22: UBR4 loss impairs the trafficking of endocytosed protein cargoes.

(A) Schematic diagram of fluorescence-labeled EGF$^+$ vesicles trafficking. X and Y represent peripheral and perinuclear cellular regions, respectively. (B) Immunostaining of Alexa Fluor 555-labelled EGF and EGFR on +/+ and *UBR4*$^{-/-}$ MEFs. Cells were incubated with serum-free medium for 1 h, followed by 1 µg/ml EGF treatment during the indicated time. White dotted line delineates cell boundary (scale bar = 10 µm). (C) Schematic diagram of quantitative analysis of internalized EGF-EGFR complex. Upper panel shows a confocal image of Alexa Fluor 555-labelled EGF and EGFR on +/+ MEF. Each of the confocal image was manually segmented based on distance from the plasma membrane (down panel). Each band has a width of 1 µm. (D) Segmented band-based quantitative analysis of subcellular EGF-EGFR complex distribution. Plot showing the subcellular distribution of EGF-EGFR complex from the plasma membrane during EGF treatment for 10 min. *$p = 0.0157$ for 1 µm, ***$p < 0.0001$ for 2 µm, and ***$p = 0.0096$ for < 10 µm compared to +/+ MEF cells, respectively (n = 3 in +/+ and 5 in *UBR4*$^{-/-}$). Data are presented as percentage ± SEM. Statistical significance was determined using two-way ANOVA and Sidak's test as a post hoc comparison. (E) Plot showing the subcellular distribution of EGF-EGFR complex from the plasma membrane during EGF treatment for 20 min. *$p = 0.0221$ for 2 µm and ***$p = 0.0005$ for < 10 µm compared to +/+ MEF cells, respectively (n = 7 in +/+ and 5 in *UBR4*$^{-/-}$). Data are presented as percentage ± SEM. Statistical significance was determined using two-way ANOVA and Sidak test as a post hoc comparison.

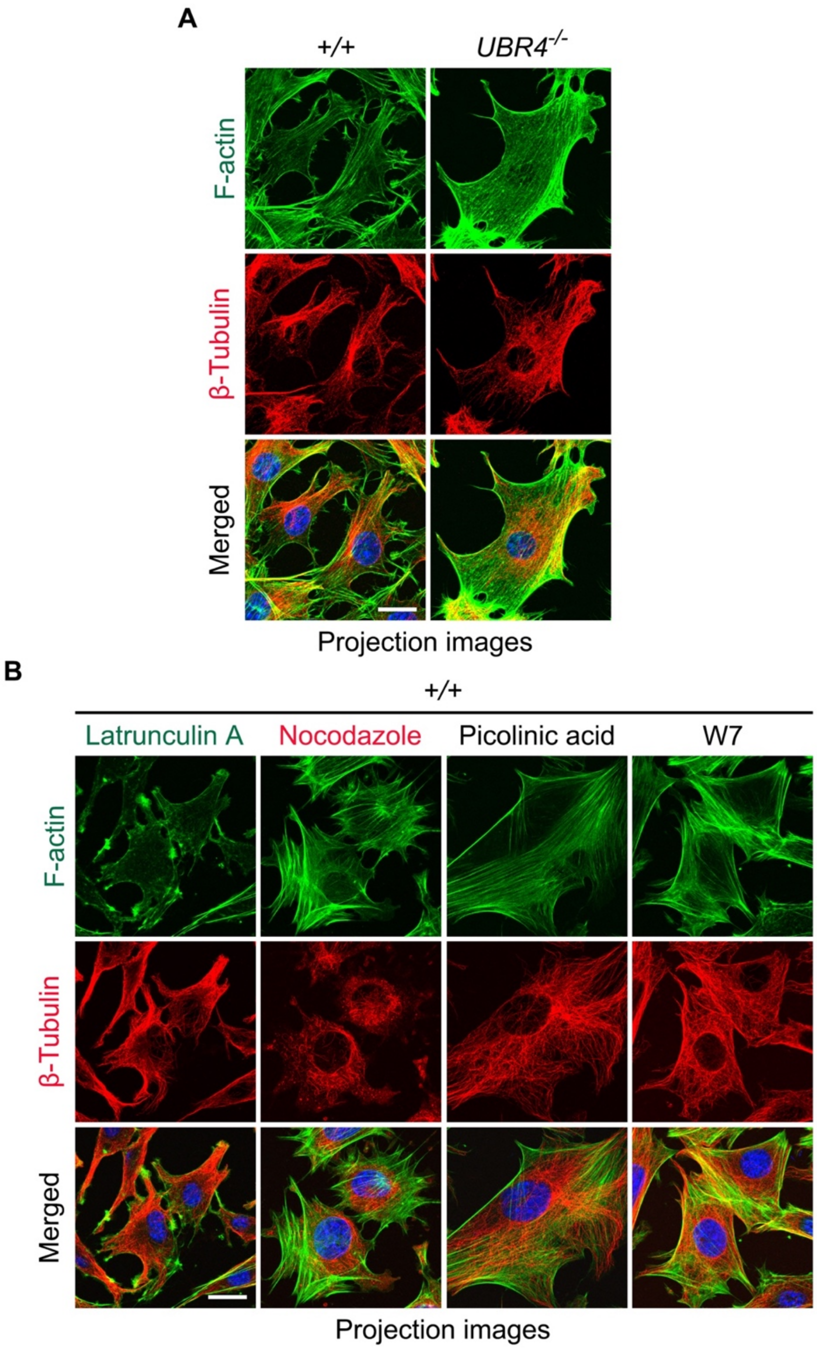

Figure 23: UBR4 depletion does not destabilize cytoskeletal filaments and microtubules.

(A) Immunostaining analysis of actin filaments and microtubules on +/+ and *UBR4*$^{-/-}$ MEFs. All images are displayed as z-stack maximum projections (scale bar = 10 µm). (B) Immunostaining analysis of actin filaments and microtubules on +/+ MEF cells. Cells were treated with latrunculin A and nocodazole for 6 h as actin- and microtubule-destabilizing agents, respectively. Cells were also treated with picolinic acid for 24 h and W7 for 30 min, respectively (scale bar = 10 µm). All images are displayed as z-stack maximum projections.

3.3.6 Defective endosomal proteolysis in UBR4-deficient MEFs.

One important function of endosomes is the turnover of plasma membrane-associated and extracellular proteins. To characterize the role of UBR4 in endosomal proteolysis, we treated +/+ and *UBR4*$^{-/-}$ MEFs with an endocytic cargo DQ-BSA, which generates fluorescence upon endosomal proteolysis [117]. Fluorescence analysis showed that in +/+ MEFs, DQ-BSA was normally endocytosed and degraded by endosomal hydrolases (Figure 24A and B). In sharp contrast, the degradation of DQ-BSA was markedly impaired in *UBR4*$^{-/-}$ MEFs as compared with +/+ cells (Figure 24A and B). Such an inhibition of DQ-BSA degradation was reproduced when UBR4 was transiently silenced using siRNA (Figure 24A and B). These results suggest that the misregulated biogenesis of early endosome reduces degradation of endosomal protein cargoes, implicating the significance of UBR4 in endosomal proteolysis.

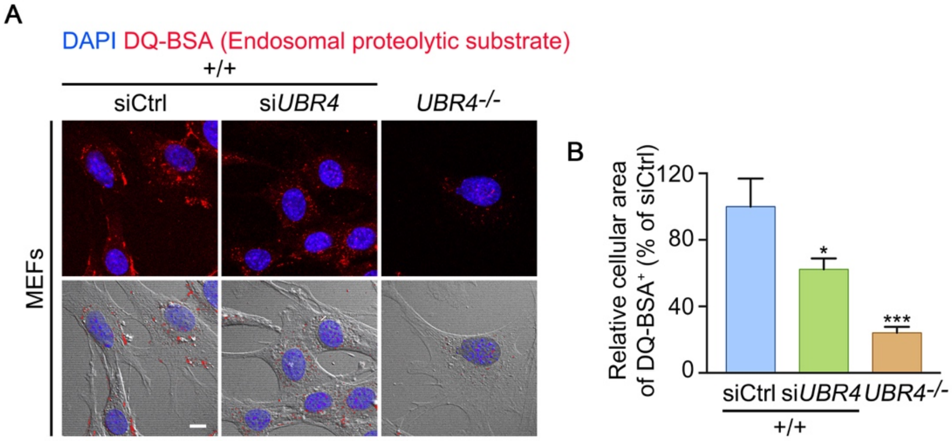

Figure 24: UBR4 is required for proteolysis of endosomal cargoes.
(A) Immunofluorescence analysis of +/+ and *UBR4*$^{-/-}$ MEFs treated with the model substrate DQ-BSA of endosomal proteolysis for 40 min (scale bar = 10 μm). +/+ MEFs were transiently transfected with negative control siRNA (siCtrl)

and UBR4 siRNA (si*UBR4*) for 48 h. UBR4 loss disrupts endosomal proteolysis. (B) Quantification of A, representing the relative cellular area of DQ-BSA$^+$ puncta. * $p = 0.0375$ and ***$p < 0.0001$ compared to siCtrl-treated +/+ MEF cells (n = 30 in each group). Data are presented as mean percentage ± SEM of siCtrl-treated +/+ MEF cells. Statistical significance was determined using one-way analysis of variance (ANOVA) and Tukey test as a post hoc comparison.

3.3.7 Development of a UBR4 ligand and its use to reversibly inhibit endosomal processes.

To develop a pharmaceutical reagent targeting UBR4, we screeened 11,679 drugs through DrugBank 5.0 database, a bioinformatics and cheminformatics resource containing drugs and their (putative) targets [118]. This screening identified picolinic acid as a putative ligand to the zinc finger of UBR4. Picolinic acid is a pyridine carboxylate metabolite of the type-2 amino acid tryptophan of the N-end rule pathway [118] (Figure 25A). To determine whether picolinic acid binds UBR4, we assessed the ability of picolinic acid to pulldown full-length 570 kDa UBR4 from HEK293 cell extracts. In comparison, we performed analogous assay using biotin-conjugated 11-mer peptides bearing Nt-Arg (type 1), Nt-Phe (type 2), and Nt-Gly (stabilizing). UBR4 was pulled down by picolinic acid, Arg-peptide and Phe-peptide but not by Gly-peptide (Figure 25B and C). Although we do not exclude the possibility of off-target effects, these results suggest that picolinic acid binds UBR4. Next, to assess the efficacy of picolinic acid, we treated this compound on HeLa cells transiently expressing EEA1-EGFP and RAB5-mRFP. This treatment markedly down-regulated the formation of EEA1$^+$ as well as RAB5$^+$ early endosomes (Figure 25D and E). The inhibitory effect of picolinic acid on endosomal maturation was reversible (Figure 25F-I). Specifically, although transfected EGFP signals was not affected by picolinic acid (Figure 25F), EEA1$^+$ and RAB5$^+$ puncta became smaller in a time-dependent manner and were readily restored when picolinic acid was removed (Figure 25G-I). These results provide a means to modulate endosomal processes by targeting UBR4.

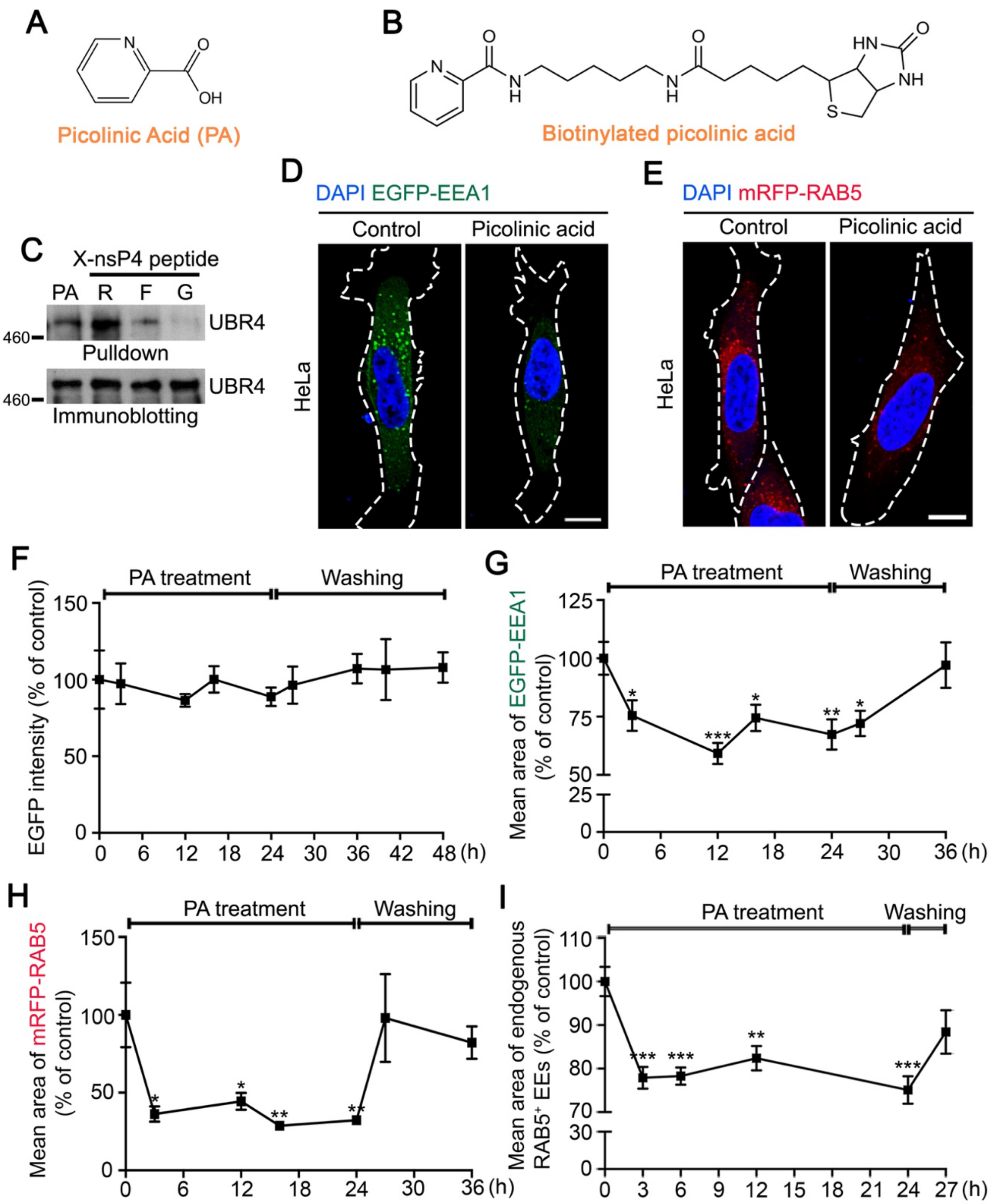

Figure 25: Development of a UBR4 inhibitor and its use to inhibit early endosomal biogenesis.

(A) The chemical structures of picolinic acid. (B) The chemical structure of biotinylated picolinic acid. (C) The pulldown assay of UBR4 using biotin-conjugated picolinic acid (PA) which is immobilized on streptavidin-beads. Also shown is the X-peptide pulldown assay in which UBR4 was captured using biotin-conjugated 11-mer X-nsP4 peptides (X= Arg, Phe, or Gly) which are immobilized on streptavidin-beads. (D and E) Fluorescence analysis of

EGFP-EEA1 and mRFP-RAB5. Picolinic acid perturbed the formation of early endosomes in HeLa. HeLa cells were transiently transfected with EGFP-EEA1 and mRFP-RAB5 for 48 h, respectively, followed by the treatment of 3 mM picolinic acid for 24 h. White dotted line delineates cell boundary (scale bar = 10 μm). (F) HeLa cells were transfected with EGFP and measured its intensity during picolinic acid treatment and after the washout. Control assay for G and H. (G and H) The inhibitory effects of picolinic acid on endosomal biogenesis was reversible. After PA treatment, we measured the average puncta sizes of transiently transfected EGFP-EEA1$^+$ and mRFP-RAB5$^+$ before and after PBS washing in a timely manner. $*p < 0.05$, $**p < 0.001$, $***p < 0.0001$ ($n = 25$ for EEA1 and $n = 10$ for RAB5). Data are presented as mean percentage ± SEM of untreated control. Statistical significance was determined using one-way ANOVA and Dunnet's multiple comparison test as a post hoc comparison. (I) PA reversably inhibits the maturation of endogenous RAB5$^+$ endosomes in HeLa cells ($n = 18$ in each group). Shown are the time-course measurement of relative areas of endogenous RAB5$^+$ puncta. Note that HeLa cells normally generate RAB5$^+$ endosomes after picolinic acid is washed out. $**p < 0.001$, $***p < 0.0001$. Data are presented as mean percentage ± SEM of untreated control. Statistical significance was determined using one-way ANOVA and Dunnet's multiple comparison test as a post hoc comparison. Panel C was conducted by Suran Mun.

To determine the function of picolinic acid in endosomal trafficking, we treated DMSO and picolinic acid in HeLa cells with Alexa Fluor 555-conjugated EGF and monitored the intracellular trafficking of the EGF$^+$EGFR$^+$ complex using co-immunofluorescence assay. By 10 min, most EGF$^+$EGFR$^+$ endosomes migrated from the plasma membrane to the peri-nuclear region in control group (Figure 26A). However, picolinic acid arrested the migration of EGF$^+$EGFR$^+$ complex. As alternative assay, we monitored the intracellular trafficking of Alexa Fluor 488-conjugated transferrin. Fluorescence analysis showed that trafficking of transferrin was also similarly impaired by picolinic acid (Figure 26B). These results suggest that picolinic acid inhibits endosomal processes such as early endosomal maturation and trafficking of ligand-receptor complexes internalized from the plasma membrane.

Next, we tested whether picolinic acid treatment effects on the protein level of UBR4. Immunoblotting analyses showed that the treatment of picolinic acid did not change the total cellular level of UBR4 (Figure 26C and D). Even though the inhibited endosomal maturation and trafficking by picolinic acid, the decreases are not due to the reduction of UBR4 level.

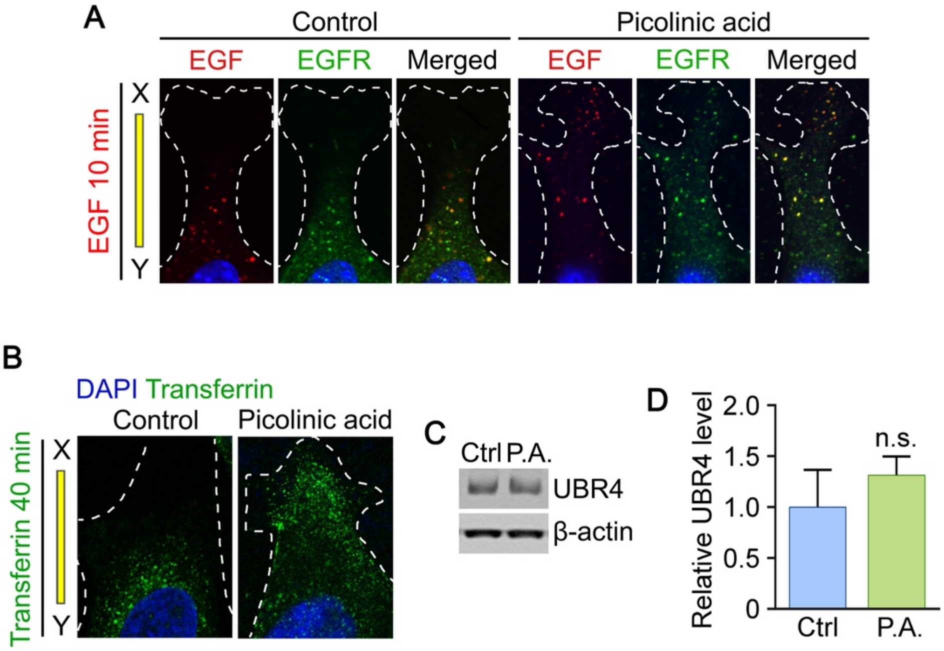

Figure 26: Picolinic acid impairs endosomal trafficking.

(A) Immunostaining of Alexa Fluor 555-labelled EGF and EGFR on HeLa cells. Cells were incubated with starvation medium for 1 h, followed by 1 μg/ml EGF treatment for 10 min. White dotted line delineates cell boundary. (B) Fluorescence analysis of Alexa Fluor 488-labelled Transferrin on HeLa cells. Cells were incubated with starvation medium for 1 h, followed by 500 ng/ml transferrin treatment for 40 min. Picolinic acid that binds to UBR box of UBR4 hampers endosomal trafficking. White dotted line delineates cell boundary. (C) Immunoblotting of UBR4 in DMSO- and picolinic acid-treated HeLa cells. β-Actin was probed for loading control. (D) Quantification of C, showing the ratio of UBR4 amounts relative to β-actin amounts. n.s., not significant. Representative of three biological replicates. Statistical significance was determined using two-tailed t-test. Panels C and D were conducted by Yoon Jee Lee.

3.4 DISCUSSION AND CONCLUSION

We have previously identified two classes of N-recognins that can recognize the Nt-Arg residues of arginylated proteins using the UBR box (UBR1, UBR1, UBR4, and UBR5) or the ZZ domain (p62) [8, 20]. Studies by us and others have shown that UBR1 and UBR2 mediate the ubiquitination of short-lived regulators carrying N-degrons as well as soluble misfolded proteins, leading to proteasomal degradation into short-peptides [8, 15, 23, 119]. More recently, we have shown that the autophagic receptor p62 binds the Nt-Arg of arginylated ER-derived proteins and mediates their lysosomal degradation along with misfolded proteins [20]. Compared with other N-recognins, little is known about UBR4 and UBR5. In this study, we characterized the functions and mechanisms of UBR4. We show that UBR4 is associated with the endocytic vesicles in part through the binding to calmodulin (Figure 21B and 27A). Functionally, UBR4 is not critical for endocytosis, i.e., the internalization of extracellular materials such as HRP and TAT-FITC (Figure 16). However, the majority of EEA1$^+$ and RAB5$^+$ early endosome is arrested in terms of size, possibly during homotypic fusion with each other (Figure 27B). Overall, our results indicate that UBR4 is required for the biosynthesis of early endosomes (Figure 27B). This conclusion is supported by several lines of evidence: (1) *UBR4*$^{-/-}$ MEFs contained a significantly reduced number of matured EEA1$^+$ and RAB5$^+$ early endosomes (Figure 17A-E) (2) the treatment of an UBR4 inhibitor markedly down-regulated the formation of EEA1$^+$ as well as RAB5$^+$ early endosomes (Figure 25D-I), and (3) UBR4 is required for ligand-mediated endosomal trafficking from the plasma membrane (Figure 22D and E). Additionally, these disrupted endosomal maturation and trafficking observed in UBR4 deficiency MEF cells were not caused by destabilization of actin filaments and microtubules (Figure 23A). Either of picolinic acid and W7 also did not damage these cytoskeletal components (Figure 23B).

Given that UBR4 is an N-recognin, it is tantalizing to speculate that the function of UBR4 may be modulated by the Nt-Arg residues of arginylated proteins on early endosomal membranes. The majority of cell surface proteins and various extracellular materials are endocytosed and degraded by endosomal hydrolases in the early endosomes, late endosomes, MVBs, and amphi-

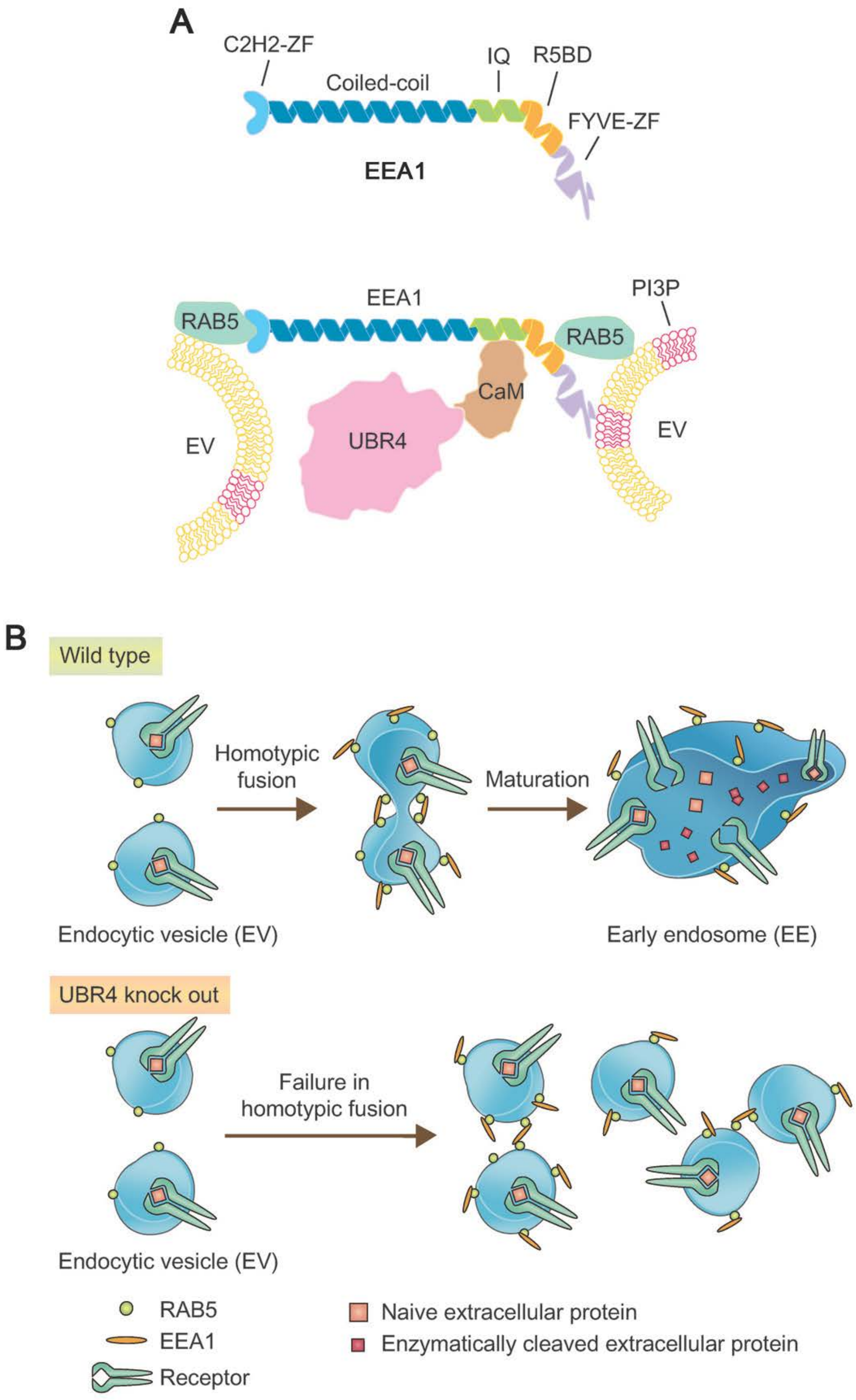

Figure 27: Schematic diagrams showing the process of endosomal maturation.

(A) A model illustrating the function of UBR4 in the endosomal fusion. Ca^{2+}-bound CaM is associated with the endocytic vesicles and induces the conformational change of EEA1, facilitating the homotypic fusion of two endocytic vesicles into an early endosome. Our results suggest that UBR4 is recruited to maturing endosomes through the interaction with Ca^{2+}-bound CaM. C2H2-ZF, Cys2-His2 zinc finger; CaM, calmodulin; FYVE-ZF, FYVE zinc finger; IQ, IQ calmodulin-binding motif; PI3P, phosphatidylinositol 3-phosphate; R5BD, RAB5-binding domain. (B) A diagram showing that two endocytic vesicles are fused with each other to form a single early endosoome. This process is impaired in UBR4-deficient cells, resulting in the accumulation of premature, abnormal endosomes.

somes [71]. Several isolated studies suggest that the overall amounts of cargoes that are digested by endosomal hydrolases may match or even exceed those by lysosomal hydrolases in normal conditions [71, 73-76, 81, 82]. Despite the importance of the endosomal proteolytic system, little attention has been paid to its functions and mechanisms, for example, in the turnover of cell surface proteins. In principle, internalized cell surface proteins carried in the endocytic vesicles are recycled back to the plasma membrane or move forward to the degradative endosomal pathway. Although the relative portion and rate depend on cell types and physiological states, it is estimated that approximately 50% of the plasma membrane-associated proteins and 5-30% of cellular volumes are be internalized in every hour [73, 74]. In this study, we show that UBR4 plays a role in endosomal proteolytic flux. This conclusion is supported by the findings that (1) UBR4 marks and is required for endosomal proteolysis in the YS of mouse embryos (Figure 15), (2) the degradation of the model substrate DQ-BSA is markedly impaired in *UBR4*$^{-/-}$ MEFs as compared with +/+ cells (Figure 24A and B), and (3) UBR4 is required for the biogenesis of early endosomes (Figure 17).

Our earlier work has shown that UBR4 knockout mice die at E9.5-E10.5 with vascular defects in the visceral YS [24]. Vascular development in UBR4-lacking YS was arrested during angiogenic remodeling of primary capillary plexus. To date, the mechanisms underlying the YS null phenotypes remain unknown. In this study, we show that UBR4 is prominently expressed in the YS endoderm, a specialized tissue enriched in endosomal proteolysis (Figure 15B and C). In the YS, UBR4 marks EEA1$^+$ early endosomes that carry internalized extracellular proteins provided by the mother. The cargoes are partially degraded within early endosomes and amphisomes and eventually converted to amino acids [26]. Notably, our immunostaining analyses on the sections of embryonic tissues show that EEA1$^+$ early endosomes are markedly downregulated in the YS of *UBR4*$^{-/-}$ embryos (Figure 15D). Given that the resulting amino acids are the major source for protein translation during embryogenesis, defective endosomal proteolysis in the YS may contribute to developmental abnormalities and arrest.

4.0 THE ROLE OF UBR4 IN NEUROGENESIS AND HOMEOSTASIS OF CELL SURFACE PROTEINS

[Kim ST, Lee YJ, Tasaki T, Hwang J, Kang MJ, Yi EC, Kim BY, and Kwon YT. The N-recognin UBR4 of the N-end rule pathway is required for neurogenesis and homeostasis of cell surface proteins. PLOS ONE. 2018. Under review.]

4.1 RESEARCH BACKGROUND

During the development of the nervous system, cell-cell adhesion regulates the differentiation, proliferation, and migration of neural stem/progenitor cells [120, 121]. Cell adhesion is mediated by membrane-associated proteins such as cadherins, by which cells bind the extracellular matrix or interact with other cells. Of classical cadherins, neural or N-cadherin (Cadherin-2), enriched in the neural system, is a component of adherens junction, in which it interacts with delta-catenin (p120), beta-catenin, and gamma-catenin [121, 122]. N-cadherin is also broadly expressed in non-neuronal tissues such as the cardiac system [121, 123]. Mice lacking N-cadherin exhibit embryonic lethality at E10 due to impaired cell adhesion in the primitive heart and YS [121, 123]. Similar developmental defects in cell adhesion are observed in mice lacking other adhesion proteins that interact with N-cadherin [121].

We have previously constructed UBR4-knockout mice in which a UBR box-containing region, spanning exons 36 through 42, was replaced with IRES (internal ribosome entry site)-translated tau-lacZ [24]. The mutant mice die during embryogenesis from E9.5 through E10.5. UBR4-deficient mouse embryos exhibit vascular defects in the yolk sac (YS) [24, 26]. The development of blood vessels in the *UBR4*$^{-/-}$ YS advances via vasculogenesis but is arrested during angiogenic remodeling of primary capillary plexus [24]. In the YS, UBR4 marks endoderm-originated, autophagy-specialized cells that support angiogenic remodeling of mesoderm-derived vascular cells and supply autophagy-produced amino acids during early embryogenesis [24, 26]. In cultured cells, UBR4 is a substrate of autophagy, and UBR4 loss results in the induction of autophagy and its flux, implicating UBR4 in autophagy modulation [24].

In this chapter, we further characterized the null phenotypes of UBR4-deficient mouse embryos. Our results show that *UBR4*$^{-/-}$ embryos develop multiple developmental defects including neurogenesis. Various types of cells in UBR4-deficient embryos lose directionality and are morphologically abnormal, which is at least in part attributed to the impairment in cell adhesion. UBR4-loss induces the depletion of cell surface proteins associated with the inability to generate MVBs. Our results reveal an essential role of UBR4 in non-proteolytic processes such as the homeostasis of cell surface proteins and, thus, cell adhesion and integrity.

4.2 MATERIALS AND METHODS

4.2.1 Chemicals and antibodies

Rabbit polyclonal anti-UBR4 antibody (Bethyl Laboratories, IHC-00640, 1:500) was used for immunostaining of mouse tissues and cultured cells. Other antibodies were as follows: rat monoclonal anti-CD63 (R&D, MAB5417, 1:200), mouse monoclonal anti-EGFR (Santa Cruz, SC-374607, 1:200), rabbit monoclonal anti-PDGFR-β (Cell Signaling, 3169, 1:100), mouse monoclonal anti-VTI1A (BD Biosciences, 611220, 1:200), Alexa Fluor 488-conjugated phalloidin (Invitrogen, A12379, 1:100), rabbit polyclonal anti-SLC7A1 (Proteintech, 14195-1-AP, 1:100), mouse monoclonal anti-tubulin (Millipore, 05-661, 1:600), goat polyclonal anti-VAT1 (Santa Cruz, SC-107348, 1:100). For immunoblotting analysis, mouse monoclonal anti-β-actin (Sigma, A1978, 1:10,000), rabbit polyclonal anti-UBR4 (Abcam, AB86738, 1:100), and mouse monoclonal anti-GAPDH (Sigma, G8795, 1:20,000) were used. The following secondary antibodies were obtained from Invitrogen: Alexa Fluor 488 goat anti-rabbit IgG (A11034, 1:200), and Alexa Fluor 555 goat anti-mouse IgG (A21424, 1:200). Normal goat serum (ab7481) was obtained from Abcam. Hoechst 33342 (H21492) was obtained from Invitrogen. 4′,6-Diamidino-2-phenylindole dihydrochloride (DAPI; D8417) was obtained from Sigma. Vectashield antifade mounting medium (H1000) was from Vector lab. All other chemicals were reagent grades from Sigma or Merck.

4.2.2 UBR4 knockout mice.

We have previously constructed UBR4-knockout mice, in which the UBR box, a substrate recognition domain for destabilizing N-terminal residues, was replaced with IRES (internal ribosome entry site)-translated tau-lacZ [24]. Animal studies were conducted according to the Guide for the Care and Use of Laboratory Animals published by the protocols (SNU130604-2-10) approved by the Institutional Animal Care and Use Committee at Seoul National University.

4.2.3 Cell culture

We previously established immortalized primary MEFs from +/+ and *UBR4*$^{-/-}$ embryos at E8.5 [24]. MEF cells were cultured in Iscove’s modified Dulbecco’s medium (IMDM) (31980–022; Invitrogen), 15% FBS (HyClone), 0.1 mM non-essential amino acids (Invitrogen), 0.1 mM β-mercaptoethanol, and 100 units/mL penicillin/streptomycin (Invitrogen). CCL2 HeLa and HEK293 cell were purchased from the American Type Culture Collection (ATCC) and cultured in Dulbecco’s Modified Eagle’s Medium (DMEM; Gibco,10566016), supplemented with 10% FBS and 100 units/mL penicillin/streptomycin. SH-SY5Y cells were provided by Prof. Onyou Hwang (University of Ulsan College of Medicine, Seoul, Republic of Korea). SH-SY5Y cells were cultured in DMEM/F-12 (Gibco, 10565-042), supplemented with 10% FBS and 100 units/mL penicillin/streptomycin. All the cell lines were determined to be negative in a mycoplasma test using a MycoAlert detection kit (Lonza, LT07-118). All the culture plates and the cell lines were maintained at 37°C and 5% CO_2 in a humidified incubator.

4.2.4 RNA interference assay

Reagents for siRNA silencing were purchased from Life Technologies. Transfection was performed according to the manufacture's protocol. Briefly, HEK293 and SH-SY5Y cells were transfected with either siControl (cat. #4390843) or UBR4 siRNA (cat. #4392420, ID #23628) at a final concentration of 10 nM using Lipofectamine RNAiMAX reagent (Invitrogen, 13778150). Approximately 48 h after siRNA silencing, cells were harvested for immunoblotting and immunocytochemical analyses. The sequences of *UBR4* siRNAs are 5'-GCCUGUUCGAAAGCGCAAA (sense) and 5'-UUUGCGCUUUCGAACAGGC (antisense).

4.2.5 Immunoblotting analysis

Cells were washed with ice-cold PBS and lysed using RIPA buffer (50 mM Tris-HCl, 150 mM NaCl, 1% NP-40, 1% sodium deoxycholate, and 0.1% SDS) containing freshly prepared protease inhibitor cocktail (Sigma, P8340). Lysates were centrifuged at 14,000 rpm for 20 min at 4°C, and the supernatants were used for immunoblotting. Protein concentrations were measured using the BCA protein assay kit (Pierce, 23225). The samples were diluted with 2X Laemmli sample buffer (65.8 mM Tris-HCl, pH 6.8, 26.3% (w/v) glycerol, 2.1% SDS, 0.01% bromophenol blue, Bio-Rad, 161-0737) or in Lithium dodecyl sulfate (LDS) sample buffer (Invitrogen, NP0007) with a reducing reagent, followed by heating for 10 min at 70°C. Whole cell lysates were separated by sodium dodecyl sulfate (SDS)-polyacrylamide gel electrophoresis and transferred to PVDF membranes (Millipore, IPVH00010). Blocking was done using TBS-T (20 mM Tris-HCl, pH 7.5, 150 mM NaCl, and 0.05% (v/v) Tween 20) containing 1% BSA for 1 h at room temperature, and the membrane was incubated with antibodies diluted with the blocking solution for overnight at 4°C.

4.2.6 Histology and immunohistochemistry

Immunohistochemistry analysis was performed as described in the previous study [24]. Briefly, for histological analysis, embryos were fixed overnight at 4°C in 4% PFA in PBS, pH 7.4. Fixed embryos were gradually dehydrated with 70%, 90%, and 100% EtOH, followed by immersion in Neo-Clear (Millipore, 65351), followed by paraffin embedding at 58°C. The samples were sectioned transversely or sagittally with 7 μm thickness. Paraffin-embedded slides were gradually rehydrated through the serial incubation with Neo-clear, EtOH (100%, 90%, 80%, and 70%; 6 min each) and water for 20 min. The slides were treated with blocking solution (5% normal goat serum and 0.2% Triton X-100 in PBS) for 1 h and incubated with primary antibodies and subsequently secondary antibodies.

4.2.7 Immunocytochemistry of cultured cells

Immunocytochemistry analysis was performed as described in the previous study [24]. Briefly, 22 mm^2 coverslips per well were incubated with diluted poly-L-lysine (1:10 in sterile deionized water; Sigma, P8920) for 30 min. After washing once, the plate was exposed under UV radiation lamp overnight in a fume hood. Cells were cultured in the plate for further experiments. Cells were fixed in 4% PFA in PBS, for 30 min and washed with PBS three times. After 1 h blocking (5% normal goat serum and 0.3% Triton X-100 in 0.1 M PBS), the samples were incubated with primary antibodies and subsequently secondary antibodies. Confocal images were taken with a Zeiss LSM 700 laser scanning confocal microscope equipped with Zeiss C-Apochromat 60x (1.2 NA) and 40x (1.2 NA) water immersion lens and analyzed using ZEN (black edition) 2012 SP5 software (Zeiss). Using the ZEN software, z-stacks of images covering the entire cell thickness were acquired and projected maximally. Image processing and annotation was done with Adobe Photoshop, Adobe Illustrator and Fiji software [103].

4.2.8 Biotinylation and affinity purification of cell surface proteins

Cells (10^7) were washed three times with cold PBS and biotinylated for 15 min at room temperature using 0.5 mg/ml sulfo-NHS-SS-biotin (Thermo Fisher, 21331), and then washed with 50 mM Tris-HCl (pH 7.5). Cells were harvested by centrifugation (500 × *g*, 5 min, 4°C) with a buffer containing 0.5 mM oxidized glutathione (Sigma) in PBS. The cell pellet was resuspended in PBS containing 2% NP-40, 0.2% SDS, 0.1 mM oxidized glutathion, and protease inhibitor cocktail (Roche Diagnostics). Cells were then lysed by sonication on ice. Protein concentrations were measured using the Micro BCA Protein Assay Kit (Thermo, 23235) [124, 125]. Protein mixtures were diluted to a concentration of 0.6 mg/mL using PBS and biotinylated proteins were isolated using a Streptavidin Sepharose High Performance column (GE Healthcare) following the manufacturer's protocol [126]. Purified proteins were precipitated with acetone, resuspended with 0.1% SDS in 100 mM ammonium bicarbonate, and protein concentration was determined by the BCA protein assay.

4.2.9 SDS-PAGE fractionation and in-gel digestion

Fifty micrograms of protein samples were fractionated on 4–12% Bis-Tris gel (Invitrogen) and stained with Coomassie Brilliant Blue (Sigma). Each gel lane was cut into eight pieces and subjected to in-gel tryptic digestion following the general protocol [127]. Briefly, protein bands were excised, destained, and washed. Proteins were reduced with 20 mM dithiothreitol and alkylated with 55 mM iodoacetamide. After dehydration, the proteins were digested with 12.5 ng/μL sequencing grade modified porcine trypsin (Promega) in 50 mM ammonium bicarbonate overnight at 37°C. Peptides were extracted from the gel pieces with 50% (v/v) acetonitrile in 5% (v/v) formic acid and dried under vacuum.

4.2.10 Mass spectrometry analysis and relative protein quantification

Peptides were resuspended in Solvent A (0.1% formic acid in water) and loaded onto an in-house packed 75 μm (inner diameter micro-capillary) x 10 cm C_{18} column and separated with a linear gradient of 5–32% Solvent B (0.1% formic acid in acetonitrile) for 70 min at a flow rate 300 nL/min. MS spectra were recorded on Q-Exactive (Thermo Fisher) interfaced with a nano-UPLC system (Easy nLC, Thermo Fisher). The Q-Exactive was operated in data-dependent mode with one survey MS scan at 400–1600 *m/z* followed by ten MS/MS scans by normalized collision energy of 30 eV, and the duration time of dynamic exclusion was 30 s. Collected MS/MS data were converted into mzXML files through the Trans Proteomic pipeline (TPP) (version 4.5) and searched against the decoy IPI Mouse database (version 3.87, 119072 entries) for the estimation of false discovery rate (FDR) with the SEQUEST® (Thermo Fisher Scientific; version v.27, rev.

11) in SORCERER^{TM} (Sage-N Research, version 3.5) search platform. Precursor and fragment ion tolerance were set to 50 ppm and 0.5 Da, respectively. Trypsin was chosen as the enzyme and up to two missed cleavages were allowed. Carbamidomethyl of cysteine was considered as the fixed modification, and methionine oxidation as variable modification. Scaffold software (version 3.4.9, Proteome Software Inc., Portland, OR) was used to validate MS/MS based peptide and protein identifications. Peptide and protein identifications were accepted if they could be established at greater than 95% and 99% probability respectively, as specified by the Peptide and Protein Prophet algorithm, and protein identification contained at least two identified peptides [128, 129]. Relative protein quantitation was accomplished using the spectral counting. The MS/MS data were normalized to compare abundances of proteins between samples using Scaffold software. The normalized spectral counts from duplicate measurements of the +/+ and *UBR4*$^{-/-}$ MEFs cells were compared using the R program with PLGEM software (http://www.bioconductor.org) in order to identify statistically significant protein changes between the two cell lines [130]. The subcellular localization of the identified proteins was classified using Ingenuity Pathway Analysis (IPA) (Ingenuity® Systems, www.ingenuity.com).

4.2.11 Immunogold labelling for transmission electron microscopy.

Immunoelectron microscopy experiment was performed as previously described [24]. UBR4V5 stably expressing HEK293 cells were fixed in 2% PFA in PBS for 1 h, followed by PBS washing. The fixed cells were collected by scraping and resuspended in 3% gelatin. Solidified gelatin on ice was fixed again with 2% PFA for 15 min. After sequential cryoprotections with 2.3 M sucrose and PVP solution overnight, samples were frozen in liquid nitrogen and were trimmed into 0.5 mm cubes, which were sectioned by cryo-microtome (Leica EM Crion) in 70 nm sections. The primary antibody against V5 was diluted in 0.1 M PBS, supplemented with 0.5% bovine serum albumin (BSA), 0.15% glycine. Secondary antibody, 12nm gold beads labelled donkey anti-rabbit IgG (Jackson ImmunoResearch), was diluted to 1:25. Sections were incubated with 2.5% glutaraldehyde for 10 min and with 2% Neutral UA acetate for 7 min, followed by incubation in 4% uranyl acetate and methyl cellulose for contrasting and drying. After drying, samples were recorded using JEOL JEM1011 TEM with high resolution AMT digital camera (Peabody, MA).

4.2.12 Statistical analysis

All numerical data are presented as means ± SEM or mean percentages ± SEM. Western blots shown are representative of three or more independent experiments. Comparisons among treatment groups were performed with one-way ANOVA and Tukey test or Dunnett’s multiple comparison as a post hoc comparison. Instances involving only two comparisons were evaluated with unpaired t-test or two-tailed Mann-Whitney test for non-parametric test. Statistical significance was accepted if the null hypothesis was rejected with $p < 0.05$. All statistical analyses were determined using Prism 7.0c software (GraphPad, La Jolla, CA).

4.3 EXPERIMENTAL RESULTS

4.3.1 Mouse embryos lacking UBR4 die associated with multiple developmental abnormalities.

We have previously constructed UBR4 knockout mice, in which a 4.1 kb-DNA fragment encoding the UBR box was deleted [24]. The mutant mouse embryos died at midgestation (~E9.5-10.5) associated with vascular defects in the YS (Table 1) [24]. In this study, we characterized the null phenotypes of the mutant embryos proper. When gross phenotypes were examined, *UBR4*$^{-/-}$ embryos began to show growth retardation at E8.5, resulting in developmental arrest at E9.5 (Figure 28A). By E10.5, most homozygous mutants were close to death or found dead (Table 1). No live mutants were retrieved at and beyond E11.5. These results suggest that UBR4 is indispensable for embryonic development at midgestation.

One distinct developmental defect was that the majority of *UBR4*$^{-/-}$ embryos between E8.5 and E9.5 had smaller and malformed pharyngeal arches as compared to control embryos (Figure 28A). The abnormalities were more prominent in the second pharyngeal arch, which is derived from pharyngeal epithelium and mesenchymal cells (Figure 28A and B, blue line). It is known that mesoderm cells in the first arch migrate to the developing heart tube, contributing to right ventricular myocardium at E7.5-E8.0 (Figure 28B). By E9.5-E10, mesodermal cells in the second arch also migrate to contribute to outflow tract myocardium [131]. Consistent with these developmental fates, *UBR4*$^{-/-}$ embryos almost invariably exhibited defects in cardiovascular development characterized by thin myocardium and loosely associated cardiac fibroblasts (Figure

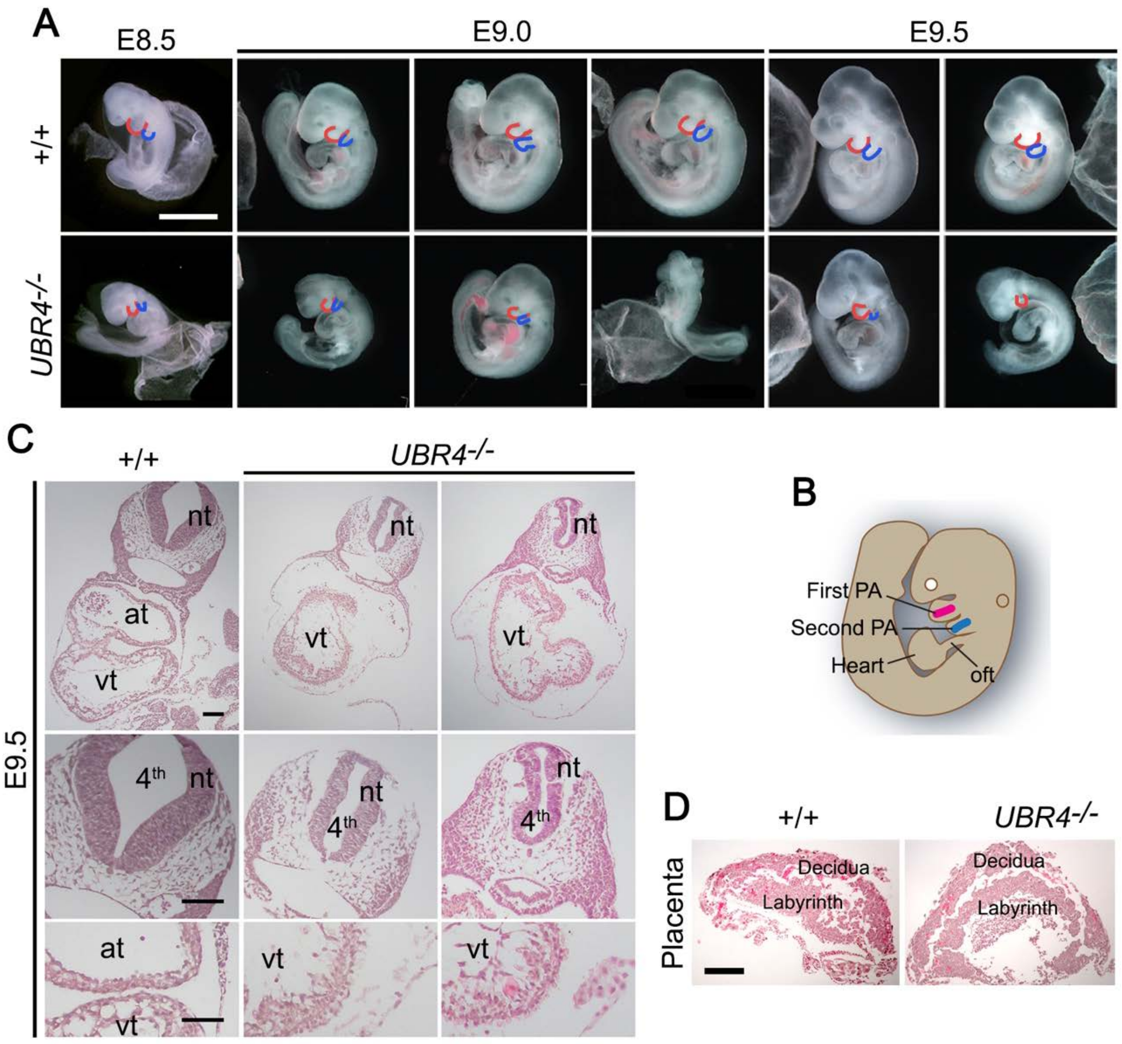

Figure 28: Mouse embryos lacking UBR4 die at midgestation associated with multiple developmental abnormalities.

(A) Gross morphology of +/+ and *UBR4*$^{-/-}$ mouse littermates at E8.5-E9.5. UBR4 mutants exhibit embryonic growth retardation and malformed pharyngeal arches. The red and blue lines represent the first pharyngeal arch and second pharyngeal arch, respectively (scale bar = 1 mm). (B) Anatomical illustration of the pharyngeal arch (PA) and heart of the mouse embryo at E9.0. First pharyngeal arch mesodermal cells (red) move to the developing heart tube for the right ventricular myocardium at E7.5-8.0, while second pharyngeal arches mesodermal cells (blue) migrate to the outflow tract (oft) of the myocardium at around E9.5-E10. (C) Hematoxylin and eosin (H&E) staining on cross sections of +/+ and *UBR4*$^{-/-}$ embryos at E9.5. nt, neural tube; at, atrium; vt, ventricles; 4th, fourth ventricle (scale bar = 100 μm). (D) H&E staining of the placenta of +/+ and *UBR4*$^{-/-}$ mouse littermates at E9.5 (scale bar = 500 μm). Panels C and D were conducted by Takafumi Tasaki.

28C). Despite such pleiotropic abnormalities, the placenta of *UBR4*$^{-/-}$ embryos at E9.5 did not show severe morphological and histological abnormalities in the spongiotrophoblast and labyrinthine layer (Figure 28D), indicating that these null phenotypes observed in *UBR4*$^{-/-}$ embryos are not secondary to the YS vascular defects. These results suggest that UBR4 is required for embryonic development at and beyond E8.0.

4.3.2 UBR4 is required for embryonic neurogenesis.

To further characterize the *in vivo* role of UBR4 in embryonic development, we histologically examined the cross sections of +/+ and *UBR4*$^{-/-}$ mouse embryos at E8.5 through E10.5. One prominent histological phenotype was noticed in neurogenesis (Figures 28C and 29A). The neural tube of *UBR4*$^{-/-}$ embryos at E9.5 was thinner and rough on the surface of the neuroepithelium as compared with littermate controls (Figures 28C and 29A). The fourth ventricle in *UBR4*$^{-/-}$ embryos was morphologically abnormal, shrunken, and almost closed as compared with control embryos (Figure 28C). The areas between mesencephalic ventricles and cephalic mesenchyme tissues were significantly reduced (Figure 29A). The cells located in cephalic mesenchyme tissues were sparsely found and did not show directionality (Figure 29A). These results suggest that UBR4 is required for neurogenesis.

We next determined whether the developmental defects are secondary to cell proliferation and death. TUNEL assays on cross sections of +/+ and *UBR4*$^{-/-}$ embryos showed that the severity of null phenotypes correlated to the degree of apoptotic induction (Figure 29B). However, the overall levels of apoptotic cells were not significantly influenced by UBR4 knockout. We therefore examined cellular senescence by monitoring the activity of β-galactosidase, an indicator of sene-

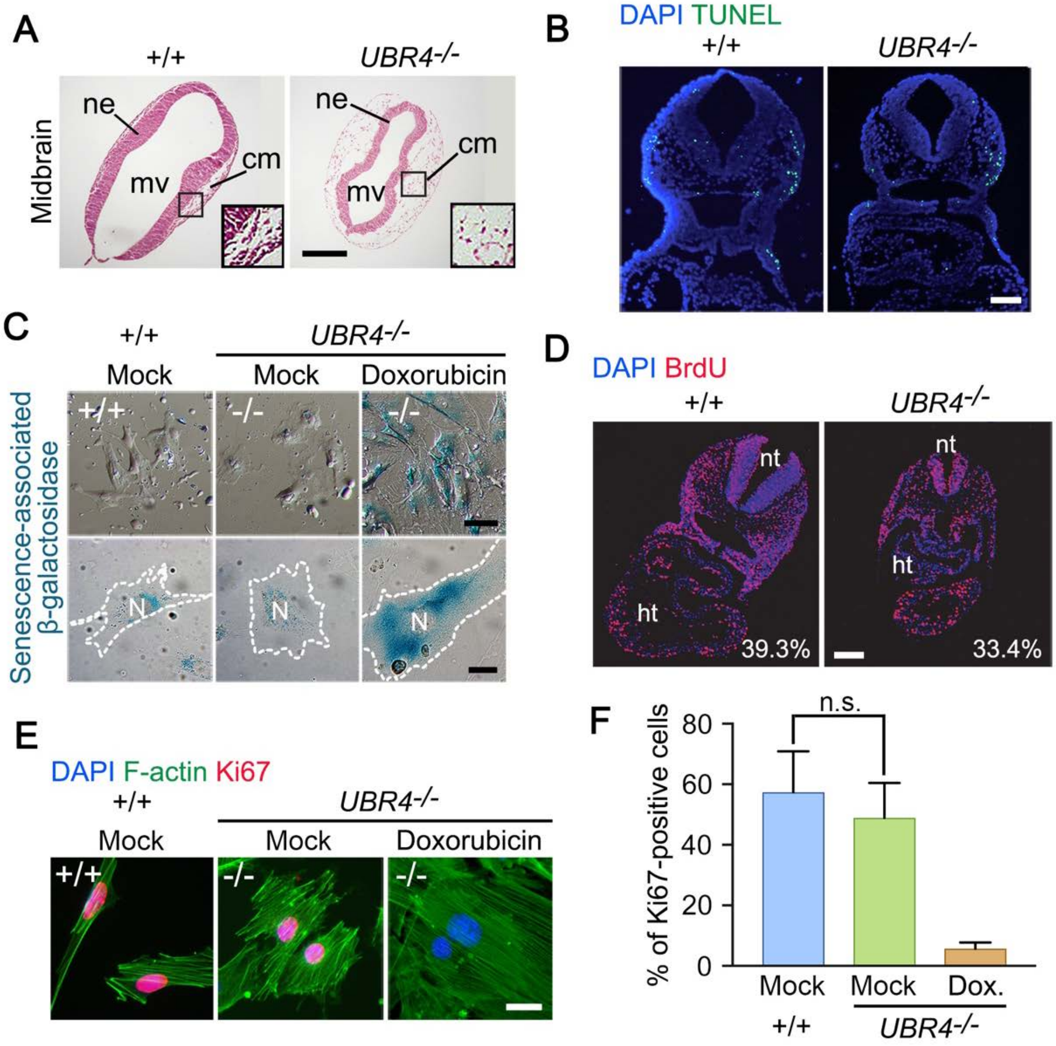

Figure 29: The null phenotypes of *UBR4*$^{-/-}$ embryos are not due to cell death or misregulation in cell cycle or proliferation.

(A) H&E staining of the midbrain of +/+ and *UBR4*$^{-/-}$ mouse embryos at E9.5. Insets: magnified image of area enclosed by lined boxes. cm, cephalic mesenchyme tissue; mv, mesencephalic vesicle; ne, neuroepithelium of midbrain region (scale bar = 200 μm). (B) TUNEL assay of +/+ and *UBR4*$^{-/-}$ embryos at E9.5 (scale bar = 150 μm). (C) Cytochemical staining of senescence-associated β-galactosidase (SA-βgal) activity in +/+ and *UBR4*$^{-/-}$ MEFs. For a positive control, *UBR4*$^{-/-}$ MEF were treated with 50 nM doxorubicin for 7 days. White dotted line delineates the cell boundary (scale bar = 30 and 15 μm, respectively). N, nucleus. (D) BrdU incorporation assay of +/+ and *UBR4*$^{-/-}$ embryos at E9.5. S-phase indices were determined to be 39.3% and 33.4% for +/+ and *UBR4*$^{-/-}$ embryos, respectively. nt, neural tube; ht, heart (scale bar = 150 μm). (E) Immunostaining of F-actin (filamentous actin) and Ki67 in +/+ and *UBR4*$^{-/-}$ MEFs. For a negative control (G_0 phage), *UBR4*$^{-/-}$ MEF were treated with 50 nM doxorubicin for 7 days. (scale bar = 15 μm). (F) Quantitative of Ki67-positive signals in +/+ and *UBR4*$^{-/-}$ MEFs. Statistically no significant difference was noted between +/+ and *UBR4*$^{-/-}$ MEFs (n.s., not significant; $p = 0.8591$). Data are presented as mean percentage ± SEM. Statistical significance was determined using one-way ANOVA and Tukey test as a post hoc comparison. Panels A, B, and D were conducted by Takafumi Tasaki.

scence (Figure 29C). *UBR4*$^{-/-}$ MEFs did not contain a comparable level of β-galactosidase activity and, thus, had the capacity to undergo cell cycle. To determine whether UBR4 loss affects cell proliferation, we measured the S-phase index of *UBR4*$^{-/-}$ embryos. We injected bromodeoxyuridine (BrdU) into pregnant females, harvested embryos, and examined the incorporation of BrdU into S-phase DNA. Anti-BrdU immunostaining analyses on the cross sections of +/+ and *UBR4*$^{-/-}$ embryos at E9.5 showed that the S-phase index of *UBR4*$^{-/-}$ embryos was largely comparable to that of +/+ embryos (Figure 29D). Consistently, immunostaining analyses of Ki67, a marker of proliferating cells, showed that *UBR4*$^{-/-}$ MEFs were mitotically active as compared to +/+ cells (Figure 29E and F). These results suggest that the developmental abnormalities of *UBR4*$^{-/-}$ embryos are not subsidiary to reduced cell proliferation or increased cell death.

To determine the cell-autonomous function of UBR4 in neuronal cells, human neuroblastoma-derived SH-SY5Y cells were differentiated into the neuronal lineage by treating retinoic acid for 5 days. Immunostaining analyses showed that UBR4 was expressed in neuronal cells as cytosolic puncta throughout the cell body as well as the axon (Figure 30A). Next, we silenced UBR4 in differentiated SH-SY5Y cells and examined their axonal growth. Immunostaining and immunoblotting analyses confirmed that UBR4 was properly knocked down (Figures 30A, B, and 32D). Microscopic inspection revealed that UBR4-knockdown acutely induced the recession of axons as determined by axonal length without any changes in neurite diameter (Figure 30C and D). These results suggest that UBR4 is required to maintain axonal integrity of neuronal cells.

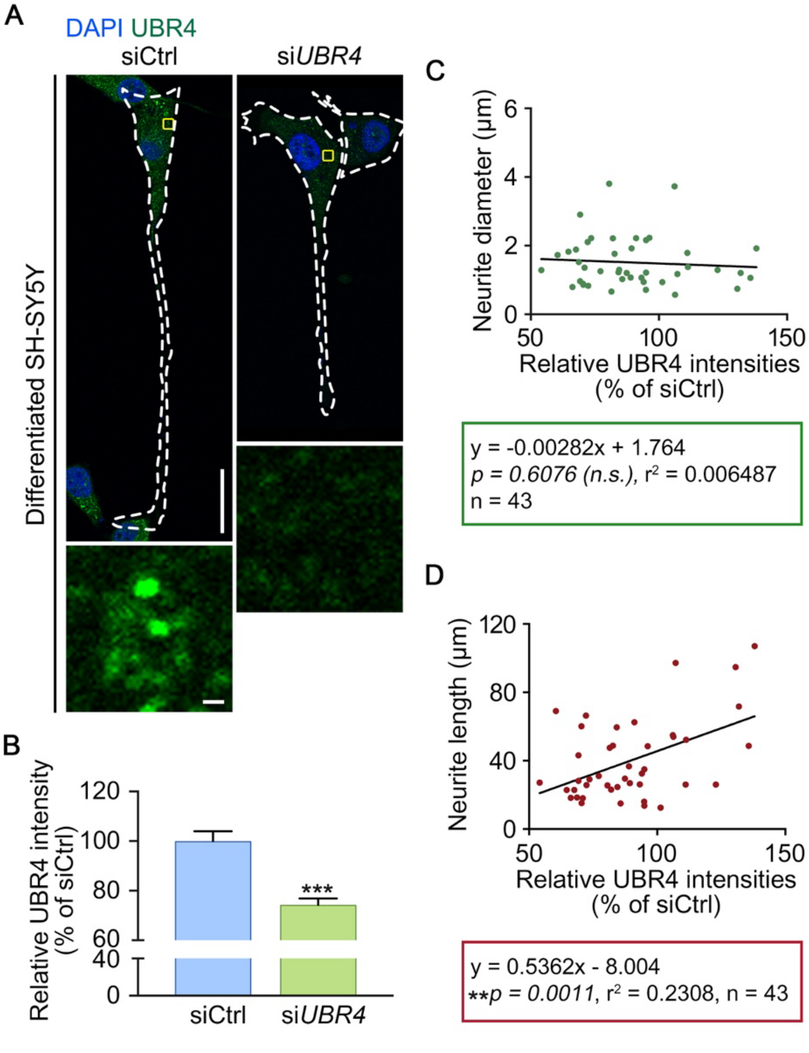

Figure 30: UBR4 depletion causes neurite shortening in differentiated SH-SY5Y cells.

(A) Immunostaining analyses of UBR4 in differentiated SH-SY5Y cells treated with siCtrl (siControl)- and si*UBR4*. SH-SY5Y cells were differentiated by retinoic acid treatment for 5 d, followed by siRNA treatment for 48 h. White dotted lines delineate the cell boundary. Enlarged views show the areas indicated by yellow rectangles (scale bar = 30 μm). (B) Quantification of A. Total 25 control and 18 UBR4 knockdown SH-SY5Y cells were observed. ***$p < 0.0001$. Data are presented as mean ± SEM. Statistical significance was determined using unpaired t-test. (C) Average neurite diameters (in μm) of control and UBR4 knockdown SH-SY5Y cells. Linear regression (solid line) was applied to this data. The slope indicates that the immunofluorescence intensity of UBR has no relationship with the neurite diameter. n.s., not significant. (D) Average neurite length (in μm) of control and UBR4 knockdown SH-SY5Y cells. Linear regression (solid line) was applied to this data. The slope indicates that the immunofluorescence intensity of UBR4 had a correlation with neurite length.

4.3.3 UBR4 plays a role in cell adhesion.

In *UBR4*$^{-/-}$ embryos at E9.5, migratory mesenchymal cells were more separated from each other as compared with +/+ embryos (Figure 29A). Although to a less degree, the extracellular space of various cells, including neuronal cells of the neural tube, was also invariably expanded than +/+ embryos (Figure 31A and B). Quantitative analyses showed that the extracellular space of neural tube in *UBR4*$^{-/-}$ embryos were about 1.5-fold ($**p = 0.004$) larger than that of +/+ embryos (Figure 31B). In addition, the cells in *UBR4*$^{-/-}$ embryos exhibited morphological abnormalities. Specifically, in +/+ embryos, mesenchymal cells were in a fibrillar shape toward the direction of migration and paracrine signaling. In sharp contrast, the same kinds of cells in *UBR4*$^{-/-}$ embryos lost fibrillar shapes and remained arrested as globular shapes (Figures 29A and 31A). These cellular defects were similarly observed in *UBR4*$^{-/-}$ MEFs which were morphologically different from +/+ fibroblasts, lacking elongated lamellipodia and filopodia (Figure 31C, arrowheads). Instead, the cytosolic surface areas of *UBR4*$^{-/-}$ MEFs were about 5-fold larger than +/+ MEFs (Figure 31D). Despite the increased surface area, *UBR4*$^{-/-}$ MEFs retained the cytoskeleton structures as determined by immunostaining analyses of actin filaments and microtubules (Figures 23A and 31E). Overall, these results suggest that UBR4 may be required for cell-to-cell adhesion.

We therefore asked whether UBR4 plays a role in cell adhesion by immunostaining N-cadherin, a type-1 transmembrane protein involved in adhesion [132, 133]. The cytoplasmic domain of N-cadherin linked to actin cytoskeleton filaments through interaction with delta-catenin, beta-catenin and gamma-catenin [122]. Immunostaining analyses of +/+ embryos revealed N-cadherin stainings as thin lines along the plasma membrane (Figure 31F). Such expression pattern was markedly downregulated and disorganized in *UBR4*$^{-/-}$ embryos (Figure 31F). Notably,

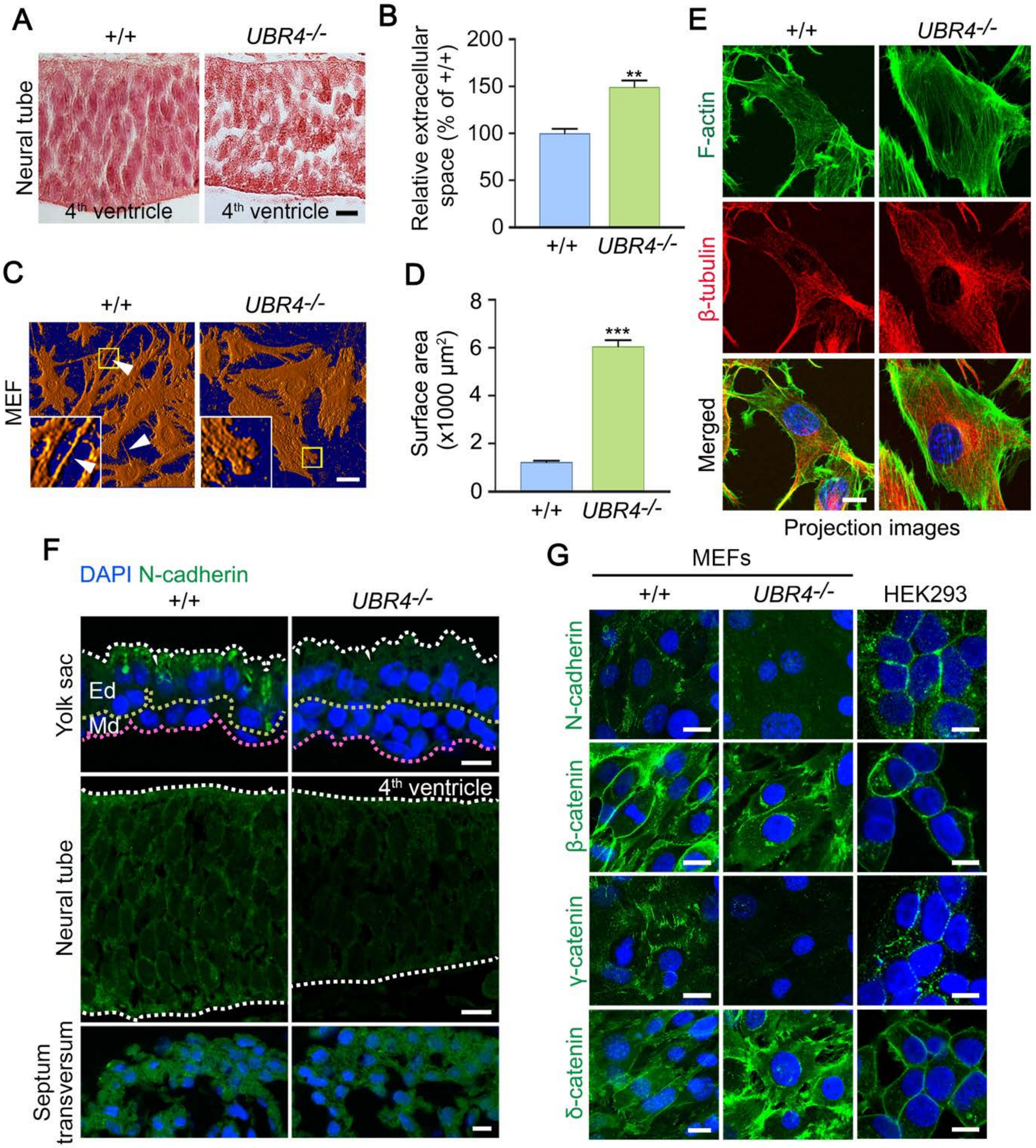

Figure 31: *UBR4$^{-/-}$* embryos are impaired in neurogenesis and cell adhesion.

(A) H&E staining images of the neural tube of +/+ and *UBR4$^{-/-}$* mouse embryos at E9.5 (scale bar = 10 μm). (B) Quantification of the extracellular space between neuronal cells in E9.5 +/+ and *UBR4$^{-/-}$* neural tubes (% of +/+). Extracellular space of *UBR4$^{-/-}$* is larger than that of +/+ (149 ± 7% of +/+, ***$p = 0.0040$* , n = 4 and n = 8 for +/+ and *UBR4$^{-/-}$* embryos, respectively). Data are presented as mean ± SEM. Statistical significance was determined using two-tailed Mann-Whitney test for non-parametric test. (C) The long-term deficiency of UBR4 caused morphological transformation in MEFs. *UBR4*$^{-/-}$ MEFs show an increased surface area and lack extended lamellipodia and filopodia. White arrowheads mark extended filopodia (scale bar = 20 µm). Insets: magnified image of area enclosed by yellow lined boxes. (D) Quantification of cellular surface (x1000 µm2). ***$p < 0.0001$ (n = 201 and n = 212 for +/+ and *UBR4*$^{-/-}$ MEF, respectively). Data are presented as mean area ± SEM. Statistical significance was determined using two-tailed Mann-Whitney test for non-parametric test. (E) Immunostaining analysis of F-actin and β-tubulin on +/+ and *UBR4*$^{-/-}$ MEFs. All images are displayed as z-stack maximum projections (scale bar = 10 µm). (F) Immunostaining of N-cadherin on cross-sections of +/+ and *UBR4*$^{-/-}$ YS and embryos at E9.5. Dotted line represents two distinct layers of the visceral YS. An outer layer derived from the visceral endoderm and an underlying layer derived from the mesoderm. Endodermal layer; Ed, mesodermal layer; Md. White dotted line on neural tube represents outlines of the neural tube (scale bar = 10 µm). (G) Immunostaining of cell-cell adjunction proteins on +/+ and *UBR4*$^{-/-}$ MEFs. HEK293 cell was used as a control cell and HEK293 cell (scale bar = 20 µm for MEFs and 10 µm for HEK293).

N-cadherin signals were more strongly disorganized in the YS and neural tubes that exhibited severe null phenotypes. By contrast, the staining appeared normal in tissues that exhibited relatively mild null phenotypes, such as mesenchymal cells of the septum transversum which gives rise to the thoracic diaphragm and the ventral mesentery of the foregut [134].

Given the results with N-cadherin, we next examined the expression of other cell adhesion proteins such as beta-catenin, delta-catenin, and gamma-catenin in +/+ and *UBR4*$^{-/-}$ MEFs. Immunostaining analyses showed that the expression patterns of all these plasma membrane-associated proteins were down-regulated or otherwise disorganized in *UBR4*$^{-/-}$ MEFs in a fashion similar to that of N-cadherin (Figure 31G). These results suggest that cell adhesion proteins are not properly presented in the plasma membrane, contributing to pleiotropic developmental defects observed in *UBR4*$^{-/-}$ embryos.

4.3.4 UBR4-loss leads to the depletion of plasma membrane proteins

Cell adhesion proteins assist growth factor receptors like EGFR (epidermal growth factor receptor) and PDGFR (platelet-derived growth factor receptor) and arrange receptor recycling and signaling

[135-137]. To assess the impact of UBR4 on the homeostasis of EGFR and PDGFR, we examined their levels in +/+ and *UBR4*$^{-/-}$ MEFs. Immunoblotting analysis showed that *UBR4*$^{-/-}$ MEFs contained a markedly reduced amout of EGFR (Figure 32A). UBR4 knockdown also acutely induced the depletion of EGFR in MEFs (Figure 32B). When visualized by immunostaining analyses, EGFR^{+} puncta in *UBR4*$^{-/-}$ MEFs appeared to be abnormal in size, morphology, and intracellular distribution as compared with those in +/+ MEFs (Figure 32C). Consistent with the results with EGFR, PDGFR-β was also depleted not only in *UBR4*$^{-/-}$ MEFs relative to +/+ MEFs (Figure 32A) but also by transient knockdown of UBR4 in MEFs (Figure 32B). These results suggest that UBR4 is required for the homeostasis of at least some plasma membrane-associated receptors, such as EGFR and PDGFR-β.

To validate these results in the neuronal lineage, we monitored EGFR and PDGFR-β in SH-SY5Y cells (Figure 32D). UBR4 knockdown induced a rapid depletion of EGFR and PDGFR-β in SH-SY5Y cells (Figure 32D). To further characterize the turnover of EGFR in differentiated neurons, we induced the axonal growth of SH-SY5Y cells by treating retinoic acid for 5 days. When visualized using immunostaining analyses, UBR4 knockdown significantly dampened EGFR stainings (Figure 32E). Finally, to extend these findings to animal tissues, we immunostained EGFR on the cross sections of +/+ and *UBR4*$^{-/-}$ mouse YS and embryos at E9.5 (Figure 32F and G). The EGFR staining was markedly diminished in *UBR4*$^{-/-}$ embryonic tissues, such as the neural tube, paraximal mesoderm, and YS (Figure 32F and G). These results suggest that UBR4 has a general role in the homeostasis of at least some plasma membrane-associated receptors.

To further characterize the role of UBR4 in the global turnover of plasma membrane-associated proteins, we labeled *in situ* plasma membrane proteins of +/+ and *UBR4*$^{-/-}$ MEFs with

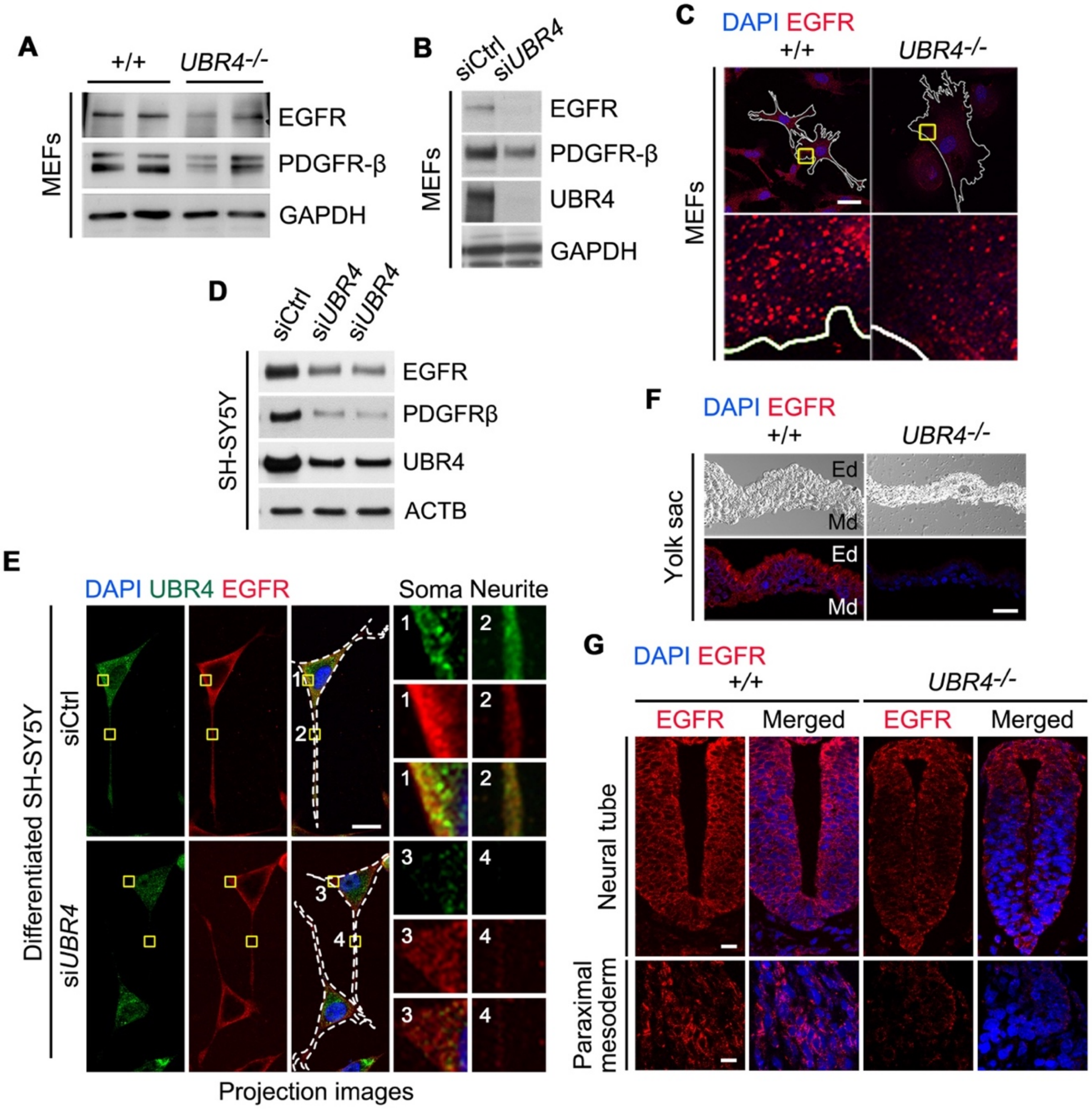

Figure 32: UBR4-loss induces the depletion of EGFR and PDGFR from the plasma membrane.

(A) Immunoblotting analysis of EGFR and PDGFR-β in +/+ and *UBR4*$^{-/-}$ MEFs. (B) Immunoblotting analysis of EGFR and PDGFR-β in siControl (siCtrl) and si*UBR4*-treated MEFs. (C) Immunostaining analysis of EGFR using +/+ and *UBR4*$^{-/-}$ MEFs. Solid white lines delineate the cell boundary (scale bar = 40 μm). Enlarged views show the areas indicated by yellow rectangles (scale bar = 3 μm). (D) Immunoblotting analysis of EGFR, PDGFR-β, and UBR4 in siControl (siCtrl) and si*UBR4*-treated SH-SY5Y cells. (E) Immunostaining of EGFR and UBR4 in siControl (siCtrl) and si*UBR4*-treated differentiated SH-SY5Y. Retinoic acid-derived differentiated SH-SY5Y cells were transiently transfected with siRNA for 48 h. Total 12 images were collected using the confocal microscope at 0.36 μm intervals to create a stack in the Z axis. The fluorescence intensity of EGFR was significantly down-regulated in UBR4 knockdown SH-SY5Y cells. White dotted lines delineate the cell boundary (scale bar = 20 μm). Enlarged views show the areas indicated by yellow rectangles and numbers. (F) Immunostaining analysis of EGFR on the cross sections of +/+ and *UBR4*$^{-/-}$ YSs at E9.5. EGFR was significantly down-regulated in the YS of *UBR4*$^{-/-}$ embryos at E9.5 (scale bar = 10 μm). Ed, endodermal layer; Md, mesodermal layer. (G) Immunostaining analysis of EGFR on the cross-sections of +/+ and *UBR4*$^{-/-}$ embryos at E9.5. EGFR was markedly down-regulated in various embryonic tissues, such as the neural tube, and paraximal mesoderm (scale bar = 5 μm). Panels A, B, and D were conducted by Yoon Jee Lee.

sulfo-NHS-SS-biotin and partially purified biotinylated proteins using streptavidin-Sepharose column. The purified proteins were separated using SDS-PAGE (Figure 33A), followed by in-gel trypsinization and LC-MS/MS analysis. The SEQUEST-SORCERER database search platform identified a total of 1,024 proteins, of which 253 were plasma membrane-associated proteins. Ingenuity Pathway Analysis and PANTHER classification system was used to annotate the function of these identified surface proteins (Figure 33B). Amongst the 253 proteins, 71 were significantly down-regulated in *UBR4*$^{-/-}$ MEFs compared to +/+ MEFs ($p \leq 0.01$) (Table 2; Figure 33C), and 22 were up-regulated (Table 3; Figure 33C). To validate the results from mass spectrometry, we performed immunostaining analyses of a few radomly selected hits, including VTI1A, SLC7A1, and VAT1 (Figure 33D). Consistent with the data from mass spectrometric analyses, *UBR4*$^{-/-}$ MEFs contained the reduced levels of VTI1A and SLC7A1 and the increased level of VAT1 (Figure 33D and E). Overall, these results suggest that UBR4 has a general role in the homeostasis of cell surface proteins.

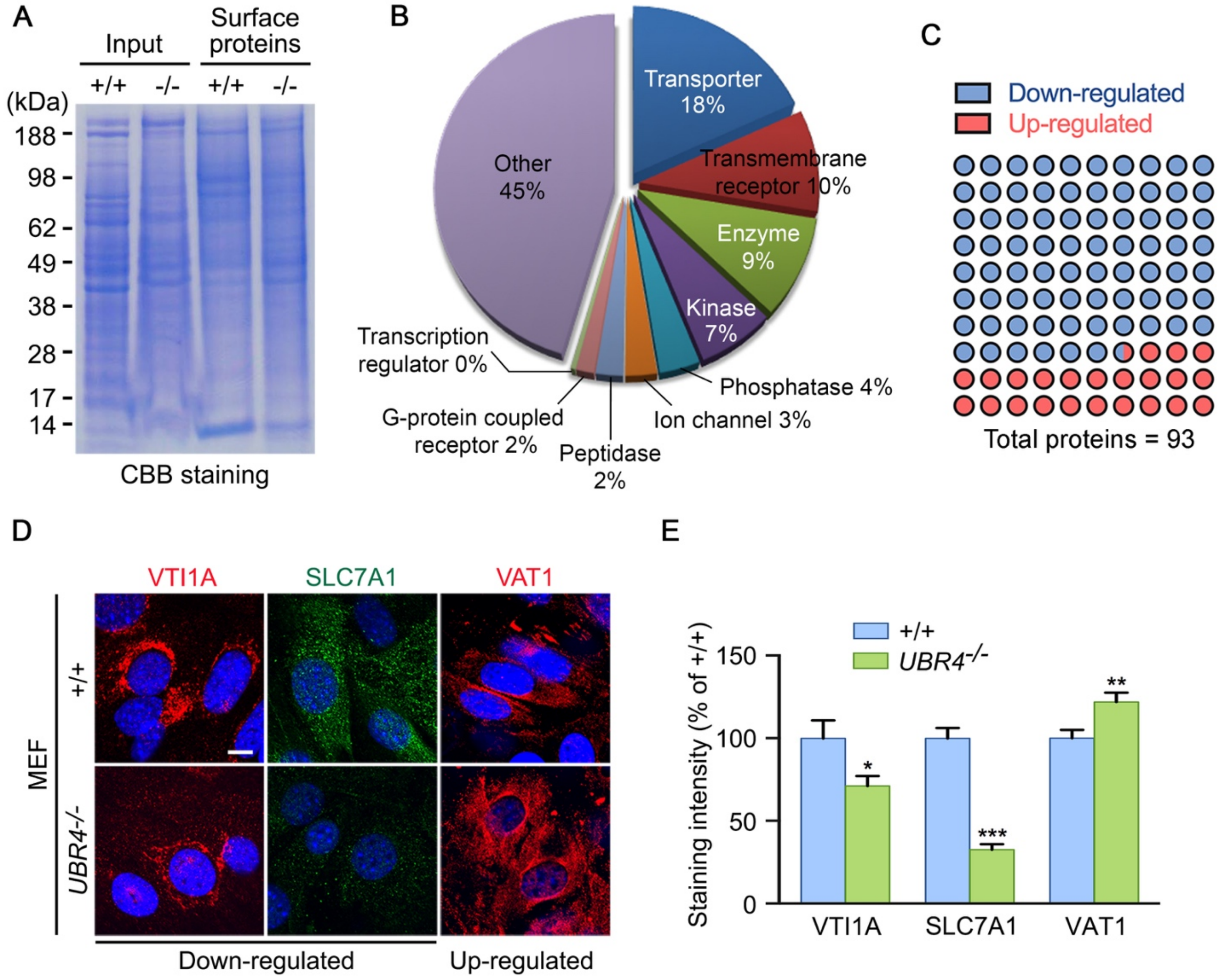

Figure 33: Proteomic analysis of cell surface proteins in MEF cells.

(A) Coomassie brilliant blue (CBB) staining of purified surface proteins separated using SDS-PAGE. (B) Molecular functions of identified cell surface proteins by the Ingenuity Pathway Analysis (IPA) tool. (C) Schematic illustration of mass spectrometric data of 93 membrane proteins whose abundance significantly altered in *UBR4*$^{-/-}$ MEFs as compared with +/+ MEFs. (D) Immunostaining analyses of VTI1A, SLC7A1 and VAT1 (scale bar = 10 μm). (E) Quantification of D, representing the relative fluorescence intensities for VTI1A, SLC7A1, and VAT1. $^{*}p = 0.0325$ vs VTI1A of +/+ (n = 13-14 in each group), $^{***}p < 0.0001$ vs SLC7A1 of +/+ (n = 13-23 in each group), and $^{**}p = 0.0070$ vs VAT1 of +/+ (n = 16-22 in each group). Data are presented as mean percentage ± SEM of +/+. Statistical significance was determined using unpaired t-test.

Table 2: The list of 71 membrane proteins down-regulated in *UBR4*$^{-/-}$ MEF cell compared with +/+ MEF.

Accession	Symbol	Entrez Gene Name	STN	*p*-value	Type(s)
IPI00468633	SLC6A9	solute carrier family 6 (neurotransmitter transporter, glycine), member 9	-1.626	0.010	transporter
IPI00115117	STOML2	stomatin (EPB72)-like 2	-1.626	0.010	other
IPI00331524	ERLIN1	ER lipid raft associated 1	-1.626	0.010	other
IPI00408489	DSCAML1	Down syndrome cell adhesion molecule like 1	-1.626	0.010	other
IPI00323822	RRAS2	related RAS viral (r-ras) oncogene homolog 2	-1.683	0.010	enzyme
IPI00122971	NCAM1	neural cell adhesion molecule 1	-1.694	0.010	other
IPI00110588	MSN	moesin	-1.727	0.009	other
IPI00648802	EPHB2	EPH receptor B2	-1.727	0.009	kinase
IPI00123040	PTPRK	protein tyrosine phosphatase, receptor type, K	-1.809	0.009	phosphatase
IPI00230395	ANXA1	annexin A1	-1.822	0.008	other
IPI00122273	DAG1	dystroglycan 1 (dystrophin-associated glycoprotein 1)	-1.827	0.008	transmembrane receptor
IPI00131540	VTI1A	vesicle transport through interaction with t-SNAREs homolog 1A (yeast)	-1.827	0.008	transporter
IPI00228617	GNAI2	guanine nucleotide binding protein (G protein), alpha inhibiting activity polypeptide 2	-1.852	0.008	enzyme
IPI00312509	AXL	AXL receptor tyrosine kinase	-1.987	0.007	kinase
IPI00129298	PALM	paralemmin	-1.987	0.007	other
IPI00129220	EPHA2	EPH receptor A2	-2.117	0.006	kinase
IPI00121827	PDGFRB	platelet-derived growth factor receptor, beta polypeptide	-2.190	0.006	kinase
IPI00664442	SLC4A7	solute carrier family 4, sodium bicarbonate cotransporter, member 7	-2.196	0.006	transporter
IPI00313884	PODXL	podocalyxin-like	-2.211	0.006	kinase
IPI00331175	SLC12A7	solute carrier family 12 (potassium/chloride transporters), member 7	-2.211	0.006	transporter
IPI00120930	PLSCR1	phospholipid scramblase 1	-2.211	0.006	enzyme
IPI00270376	CXADR	coxsackie virus and adenovirus receptor	-2.211	0.006	transmembrane receptor
IPI00123996	NRP1 (includes EG:18186)	neuropilin 1	-2.304	0.005	transmembrane receptor
IPI00123183	AQP1	aquaporin 1 (Colton blood group)	-2.304	0.005	transporter
IPI00124221	ATP1B3	ATPase, Na+/K+ transporting, beta 3 polypeptide	-2.366	0.005	transporter

Table 2 (continued).

Accession	Symbol	Entrez Gene Name	STN	*p*-value	Type(s)
IPI00416751	SLC29A1	solute carrier family 29 (nucleoside transporters), member 1	-2.413	0.005	transporter
IPI00137311	PLXNA1	plexin A1	-2.485	0.005	transmembrane receptor
IPI00405742	PLXNB2	plexin B2	-2.550	0.004	transmembrane receptor
IPI00132474	ITGB1	integrin, beta 1 (fibronectin receptor, beta polypeptide, antigen CD29 includes MDF2, MSK12)	-2.550	0.004	transmembrane receptor
IPI00121634	SLC7A1	solute carrier family 7 (cationic amino acid transporter, y+ system), member 1	-2.559	0.004	transporter
IPI00130648	VLDLR	very low density lipoprotein receptor	-2.575	0.004	transporter
IPI00117181	FLOT1	flotillin 1	-2.589	0.004	other
IPI00118569	GNA13	guanine nucleotide binding protein (G protein), alpha 13	-2.589	0.004	enzyme
IPI00308971	IGF2R	insulin-like growth factor 2 receptor	-2.608	0.004	transmembrane receptor
IPI00330539	KIRREL	kin of IRRE like (Drosophila)	-2.708	0.004	other
IPI00468236	ANO6	anoctamin 6	-2.708	0.004	ion channel
IPI00135130	SLC1A4	solute carrier family 1 (glutamate/neutral amino acid transporter), member 4	-2.725	0.004	transporter
IPI00124830	CD47	CD47 molecule	-2.728	0.004	other
IPI00465786	TLN1	talin 1	-2.756	0.004	other
IPI00754549	FLOT2	flotillin 2	-2.855	0.004	other
IPI00420589	IGSF3	immunoglobulin superfamily, member 3	-3.256	0.003	other
IPI00311682	ATP1A1	ATPase, Na+/K+ transporting, alpha 1 polypeptide	-3.359	0.003	transporter
IPI00129253	LY75	lymphocyte antigen 75	-3.406	0.003	other
IPI00117829	CAV1	caveolin 1, caveolae protein, 22kDa	-3.463	0.003	other
IPI00113798	SNAP23	synaptosomal-associated protein, 23kDa	-3.501	0.003	transporter
IPI00115976	ITGA5	integrin, alpha 5 (fibronectin receptor, alpha polypeptide)	-3.532	0.003	other
IPI00308691	SLC2A1	solute carrier family 2 (facilitated glucose transporter), member 1	-3.657	0.002	transporter
IPI00115546	GNAO1	guanine nucleotide binding protein (G protein), alpha activating activity polypeptide O	-3.657	0.002	enzyme
IPI00223769	CD44	CD44 molecule (Indian blood group)	-3.706	0.002	enzyme
IPI00113869	BSG	basigin (Ok blood group)	-3.720	0.002	transporter
IPI00125832	CAV2	caveolin 2	-3.720	0.002	other
IPI00128152	Abcb1b	ATP-binding cassette, sub-family B (MDR/TAP), member 1B	-3.735	0.002	transporter
IPI00138716	RAP2B	RAP2B, member of RAS oncogene family	-3.735	0.002	enzyme

Table 2 (continued).

Accession	Symbol	Entrez Gene Name	STN	*p*-value	Type(s)
IPI00875340	SLC1A5	solute carrier family 1 (neutral amino acid transporter), member 5	-4.118	0.002	transporter
IPI00321753	GPRC5A	G protein-coupled receptor, family C, group 5, member A	-4.118	0.002	G-protein coupled receptor
IPI00137194	SLC16A1	solute carrier family 16, member 1 (monocarboxylic acid transporter 1)	-4.434	0.002	transporter
IPI00137336	GPC1	glypican 1	-4.581	0.001	transmembrane receptor
IPI00653515	LDLR	low density lipoprotein receptor	-4.706	0.001	transporter
IPI00556827	ATP2B1	ATPase, Ca++ transporting, plasma membrane 1	-5.103	0.001	transporter
IPI00126090	ITGA3	integrin, alpha 3 (antigen CD49C, alpha 3 subunit of VLA-3 receptor)	-5.111	0.001	other
IPI00463589	ATP2B4	ATPase, Ca++ transporting, plasma membrane 4	-5.336	0.001	transporter
IPI00135324	SLC12A2	solute carrier family 12 (sodium/potassium/chloride transporters), member 2	-5.339	0.001	transporter
IPI00126834	VCAM1	vascular cell adhesion molecule 1	-5.630	0.001	other
IPI00129395	SLC7A5	solute carrier family 7 (amino acid transporter light chain, L system), member 5	-5.943	0.001	transporter
IPI00229703	VAMP2	vesicle-associated membrane protein 2 (synaptobrevin 2)	-6.411	0.001	other
IPI00114641	SLC3A2	solute carrier family 3 (activators of dibasic and neutral amino acid transport), member 2	-7.015	0.001	transporter
IPI00153809	CD109	CD109 molecule	-7.269	0.000	other
IPI00923039	ABCC4 (includes EG:10257)	ATP-binding cassette, sub-family C (CFTR/MRP), member 4	-7.505	0.000	transporter
IPI00129915	ABCC1	ATP-binding cassette, sub-family C (CFTR/MRP), member 1	-8.787	0.000	transporter
IPI00132276	VAMP3	vesicle-associated membrane protein 3 (cellubrevin)	-10.074	0.000	other
IPI00124700	TFRC	transferrin receptor (p90, CD71)	-12.33	0.000	transporter

Footnote: *STN, signal to noise ratio generated by PLGEM analysis ($p \leq 0.01$).

Table 3: The list of 22 membrane proteins up-regulated in *UBR4*$^{-/-}$ MEF cell compared with +/+ MEF.

Accession	Symbol	Entrez Gene Name	STN	*p*-value	Type(s)
IPI00831676	DYSF	dysferlin, limb girdle muscular dystrophy 2B (autosomal recessive)	8.224	0.000	other
IPI00775950	Cald1	caldesmon 1	7.194	0.001	other
IPI00323885	NPR3 (includes EG:18162)	natriuretic peptide receptor C/guanylate cyclase C (atrionatriuretic peptide receptor C)	6.709	0.001	G-protein coupled receptor
IPI00515360	HSPG2	heparan sulfate proteoglycan 2	5.239	0.001	enzyme
IPI00623114	FAT1	FAT tumor suppressor homolog 1 (Drosophila)	4.494	0.002	other
IPI00129304	COLEC12	collectin sub-family member 12	3.826	0.003	transmembrane receptor
IPI00227835	Tpm1	tropomyosin 1, alpha	3.258	0.003	other
IPI00118069	F3	coagulation factor III (thromboplastin, tissue factor)	3.195	0.003	transmembrane receptor
IPI00128915	CSPG4	chondroitin sulfate proteoglycan 4	3.006	0.004	other
IPI00109727	THY1	Thy-1 cell surface antigen	2.922	0.004	other
IPI00112963	CTNNA1	catenin (cadherin-associated protein), alpha 1, 102kDa	2.635	0.004	other
IPI00405227	VCL	vinculin	2.613	0.005	enzyme
IPI00466371	ITGA1	integrin, alpha 1	2.575	0.005	other
IPI00120716	GNB1	guanine nucleotide binding protein (G protein), beta polypeptide 1	2.213	0.006	enzyme
IPI00227838	GNG12	guanine nucleotide binding protein (G protein), gamma 12	2.211	0.006	enzyme
IPI00229534	MARCKS	myristoylated alanine-rich protein kinase C substrate	2.169	0.006	other
IPI00109108	STT3A	STT3, subunit of the oligosaccharyltransferase complex, homolog A (S. cerevisiae)	2.024	0.007	enzyme
IPI00762091	MRC2	mannose receptor, C type 2	1.925	0.008	transmembrane receptor
IPI00126072	VAT1	vesicle amine transport protein 1 homolog (T. californica)	1.925	0.008	transporter
IPI00405462	SORBS2	sorbin and SH3 domain containing 2	1.827	0.008	other
IPI00229475	JUP	junction plakoglobin	1.741	0.009	other
IPI00120245	ITGAV	integrin, alpha V	1.708	0.010	ion channel

Footnote: *STN, signal to noise ratio generated by PLGEM analysis ($p \leq 0.01$).

4.3.5 UBR4-deficient cells fail to generate MVBs.

A portion of cell surface proteins and various extracellular materials are endocytosed and degraded through the endosome-lysosome pathway [71]. During this process, cargoes carried in endosomes are deposited to MVBs, which in turn are fused with autophagosomes to form amphisomes, leading to lysosomal degradation [71, 90]. We therefore monitored the formation of MVBs in +/+ and *UBR4*$^{-/-}$ MEFs. Immunostaining analyses of the MVB marker CD63 showed that MVBs were enriched in peri-nuclear regions of +/+ MEFs (Figure 34A). By sharp contrast, *UBR4*$^{-/-}$ MEFs contained a drastically reduced level of CD63$^+$ MVBs. The down-regulation of MVBs was

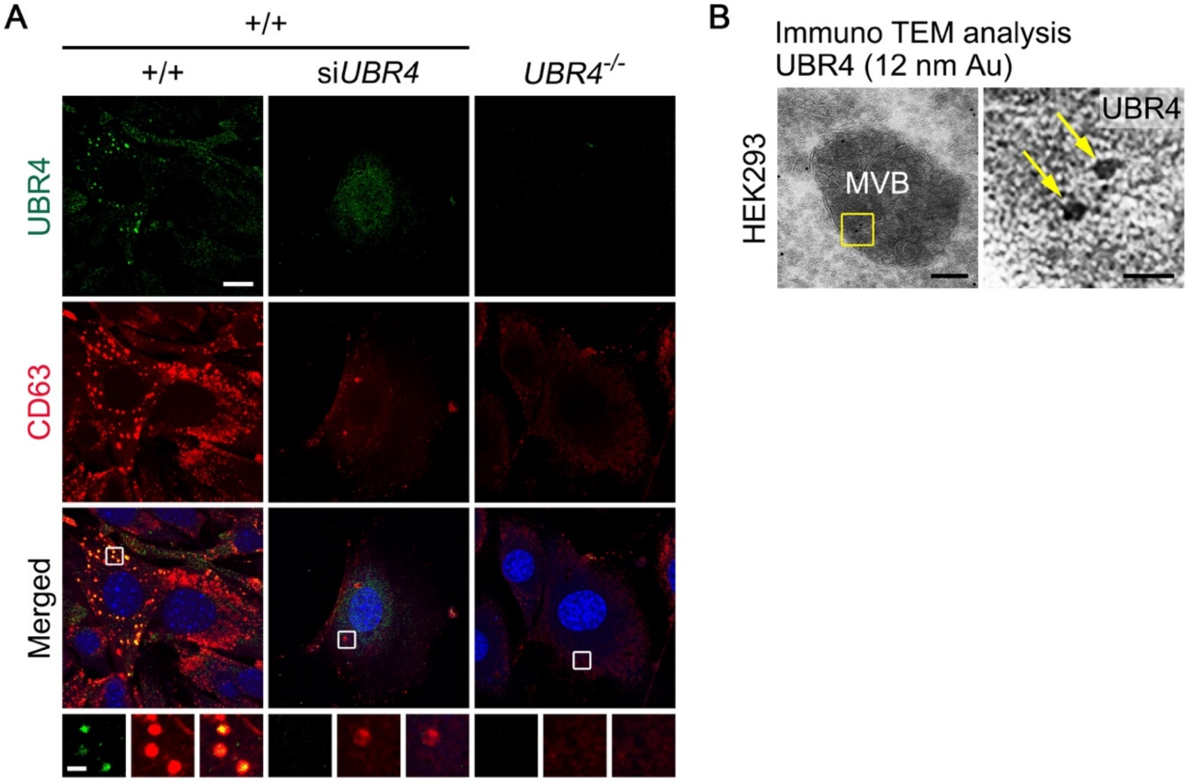

Figure 34: UBR4 is associated with MVBs and required for the formation of MVBs.

(A) Immunostaining of UBR4 and the MVB marker CD63 on siControl- and *siUBR4*-treated +/+ and *UBR4*$^{-/-}$ MEFs (scale bar = 15 μm and 300 nm, respectively). (B) Transmission electron microscopy (TEM) of HEK293 cells stably expressing UBR4V5. Fixed cells were incubated with primary antibody against V5 followed by secondary IgG antibody labelled with 12 nm gold beads. Arrows indicate UBR4V5 molecules located at an MVB (scale bar = 100 nm for left panel and 20 nm for right panel).

validated by transient silencing of UBR4 with siRNA. Consistent with a previous report [24], transmission electron microscopy showed that immunogold labeled UBR4 molecules were deposited to MVBs in HEK293 cells stably expressing UBR4V5 (Figure 34B), indicating that UBR4 was degraded along the endosome-lysosome pathway. These results suggest that UBR4 is required for the formation of MVBs and proteolysis therein, at least in part providing a mechanism underlying the depletion of cell surface proteins in the absence of UBR4.

4.4 DISCUSSION AND CONCLUSION

We have previously identified UBR4 as an N-recognin of the N-end rule pathway which binds type-1 and type-2 N-degrons of short-lived proteins to facilitate their ubiquitination and proteasomal degradation [8]. In this study, we characterized the null phenotypes of UBR4-deficient mice. Our results show that UBR4-deficient embryos die associated with developmental defects in various processes such as neurogenesis and cardiovascular development (Figure 28). The mutant cells in various tissues do not exhibit tissue-specific morphology as if they cannot receive properly external paracrine signals (Figures 29A and 31A). The mutant cells are more separated from each other, which is in part attributed to the inability to maintain cell surface proteins and, thus, cell adhesion and integrity (Figures 31 and 32). Although the mechanism underlying the role of UBR4 in the homeostasis of cell surface proteins should be further investigated, one such mechanism may be relevant to our observation that the MVBs are not properly generated in the absence of UBR4 (Figure 34).

Our results show that UBR4-deficient mouse embryos suffer from multiple abnormalities in neurogenesis and other developmental processes. Histological and cytological examinations suggest that the cells in mutant embryos fail to maintain their morphology and adhesion, leading to failure to communicate with each other and advance into more differentiated stages (Figures 28 and 31). Consistently, the expression pattern of cell adhesion markers such as N-cadherin is significantly disorganized (Figure 31F and G). Indeed, extensive studies have shown that neurogenesis in embryos is particularly sensitive to misregulation of intercellular adhesion molecules such as immunoglobulins, integrins, cadherins [138, 139].

Why are cell adhesion molecules down-regulated and disorganized in the absence of UBR4? We show that UBR4-loss results in the rapid depletion of other cells surface proteins as well, including EGFR and PDGFR (Figure 32). Moreover, mass spectrometric analyses of purified biotin-conjugated cell surface proteins indicate that a significant portion, although not all, of proteins are depleted from the plasma membrane (Figure 33; Tables 2 and 3). These results collectively suggest that UBR4 is required for the turnover of plasma membrane-associated proteins. It is known that cell surface proteins are under constitutive flux into the endosome-lysosome pathway, in which endocytosed membrane proteins are recycled or degraded through endosomal pathways toward lysosomes [71, 90]. As demonstrated in previous chapter, UBR4 is associated with early endosomes through its interaction with calmodulin and required for the turnover of cell surface proteins (Figures 21 and 27). It is therefore reasonable to speculate that the homeostasis of cell surface proteins in UBR4-deficient cells are in part caused by misregulation in their endosome-mediated turnover (Figures 15 and 17). We provide evidence that UBR4-

deficient cells fail to generate the MVBs in which endosome-cargo complexes are temporarily stored before degradation by lysosomes (Figure 34). Further mechanistic details are to be investigated.

5.0 THE FUNCTION OF ARGINYLATION BY ATE1 IN STING-DEPENDENT INNATE IMMUNE RESPONSE

5.1 RESEARCH BACKGROUND

In eukaryotes, *ATE1*-encoded Arg-tRNA transferases (R-transferases; EC 2.3.2) transfer L-arginine (L-Arg) of Arg-tRNA^{Arg} to the N-terminal Asp (Nt-Asp) and Glu (Nt-Glu) of substrates including misfolded proteins and endoplasmic reticulum (ER)-residing chaperones [14, 20, 21]. The resulting Nt-Arg residue is recognized by N-recognins like UBR box proteins (UBR1, UBR2, UBR4/p600, and UBR5/EDD) and the autophagy receptor p62, acting as a bimodal degradational signal to UPS or autophagy [8, 9, 20]. Additionally, the Nt-Arg can be generated by endoproteolytic cleavages or enzymatically through the modification of Nt-Asn, Nt-Gln, Nt-Cys, Nt-Asp, and Nt-Glu [12-15]. The Nt-arginylation of ER chaperones like binding-immunoglobulin protein (BiP/GRP78/HSPA5), calreticulin/CRT/CALR, and protein disulfide isomerase (PDI) is induced by cytosolic double-stranded DNA (dsDNA), a strong activator of the innate immune response [20]. The dsDNA-mediated immune response promotes the accumulation of Nt-arginylated of BiP (R-BiP) in the cytosol, which binds the selective autophagy receptor p62 through its binding of the ZZ domain of p62, resulting its self-oligomerization [20]. However, the physiological meanings of Nt-arginylation of BiP and the induced interaction of R-BiP with p62 in the innate immune system are poorly defined.

Autophagy is cytoprotective system that sequesters damaged cellular organelles, aggregated proteins, and foreign pathogens in double membrane vesicles (autophagosome), followed by lysosomal degradation [64]. During infection of host cells, the selective autophagy that eliminates invading pathogens and foreign particles is called as xenophagy [140]. E3 ubiquitin ligaseses contribute to xenophagy by recruitment of Ub to surface proteins of intracellular pathogens, which enables p62 to recognize poly-ubiquitinated bacterial proteins through its UBA (Ub associated) domain [141, 142]. p62 deliveries ubiquitinated foreign particles and pathogens as well as misfolded proteins to phagophores by binding LC3 using its LC3-interacting region (LIR) [20, 141]. During cytosolic foreign DNA-mediate innate immune responses, R-BiP is induced and associated with cytosolic misfolded proteins, targeted by p62. The inteaction between R-BiP and p62 facilitates p62 self-polymerization, autophagosome biogenesis, and lysosomal degradation of autophagic protein cargoes [20]. These suggest that co-induced Nt-arginylation and p62 can augment host defense system against foreign dsDNA, but its mechanism of regulation is not clearly understood.

Invading of variety pathogens is recognized by the innate immune system through the detection of viral nucleic acids (Figure 35) [143]. On the contrary, misregulated recognition of self-nucleic acids leads to autoimmune diseases like psoriasis and systemic lupus erythematosus [143]. Cytosolic DNA derived from pathogens or host cells activates innate immune response through many DNA sensors, which include AIM2 [144], DAI [145], DDX41 [146], IFI16 [147], LRRFIP1 [148], RNA polymerase III-RIG-I [149, 150], and cytosolic GMP-AMP (cGAMP) synthase (cGAS) [151]. Either these DNA sensors or DNA itself activate TMEM173/STING (stimulator of interferon genes), which is identified as a critical adaptor for cytosolic dsDNA-mediated interferons (IFNs) induction and is a transmembrane protein in the ER and/or mitochondria [152-154]. Recent studies showed that activated STING in response to cytoplasmic DNA is translocated from the ER to the Golgi compartment, on which it recruits TANK-binding kinase 1 (TBK1) and the transcription factor IFN regulatory factor 3 (IRF3), leading to NF-κB and type I IFN gene expression (Figure 36) [155, 156].

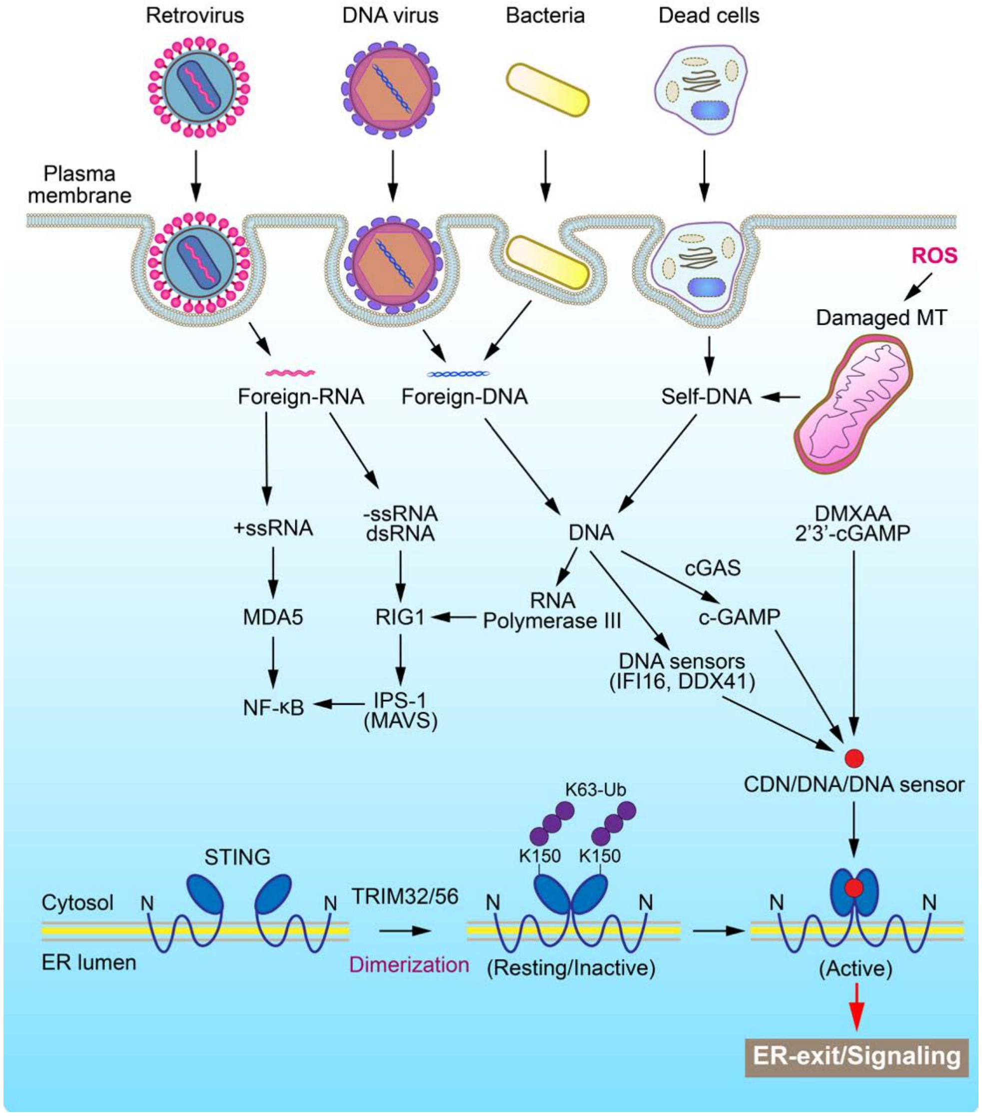

Figure 35: STING pathway of cytosolic DNA sensing.

Cytosolic DNA derived from invading pathogens or host cells activates innate immune response through many DNA sensors including DDX41, IFI16, RNA polymerase III-RIG-I, and cytosolic cGAS. These DNA sensors activate STING, which is a transmembrane protein in the ER. Activated STING in response to cytoplasmic DNA is translocated from the ER to the Golgi compartment, on which it recruits TBK1 and IRF3, leading to NF-κB and type I IFN gene expression.

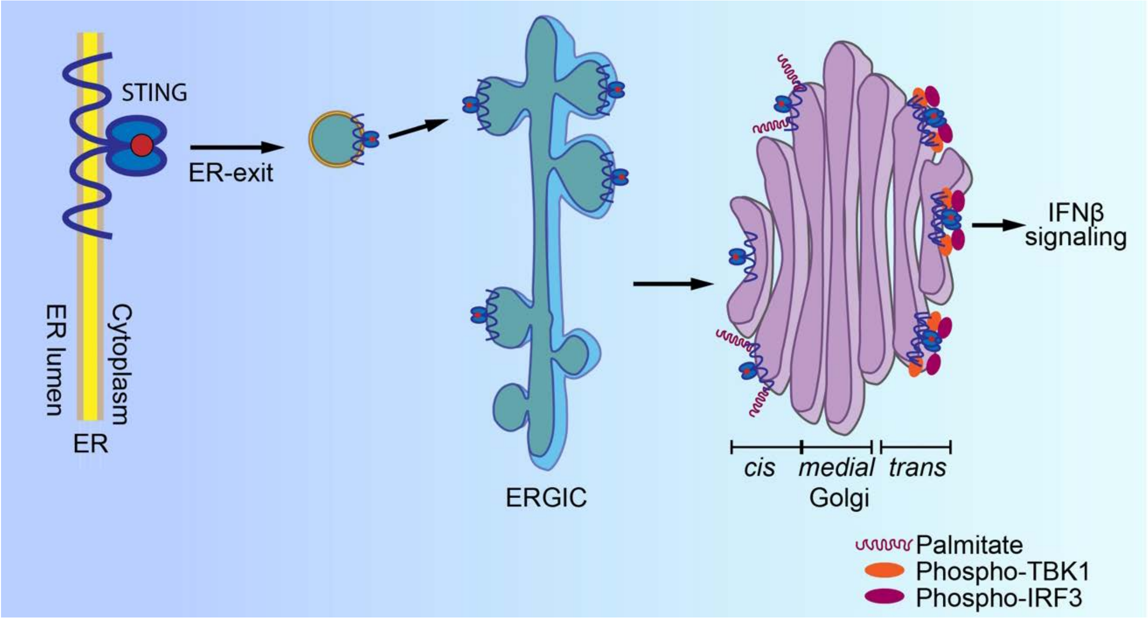

Figure 36: Translocation of STING.

Either DNA sensors or DNA itself can bind to STING, resulting its dimerization on the ER membrane. Dimerized STING in response to cytoplasmic DNA is translocated from the ER to the Golgi compartment, on which it recruits TBK1 and IRF3, leading to NF-κB and type I IFN gene expression.

Here, we show that cytosolic foreign DNA induces Nt-arginylation of ER chaperons, which is required for host defense system for IFN-β mediated gene induction and IRF3 phosphorylation. Cytosolic dsDNA facilitates relocation of ATE1 to the ER, on which ATE1 is colocalized with STING. Either transient deletion of ATE1 or its pharmaceutical inhibition with tannic acids impairs the trafficking of STING from the ER to the Golgi compartment. Activated STING complex on the Golgi compartment is eliminated by p62-mediated autophagy. Interference of Nt-arginylation that is important for host defense induces virion production. Our results suggest that Nt-arginylation is essential for cellular immune response against foreign DNA and viral infections.

5.2 MATERIALS AND METHODS

5.2.1 Chemicals and antibodies

Rabbit polyclonal antibodies specific for the arginylated forms of BiP, CRT and PDI were raised using the peptide sequences REEEDKKEDVGC, REPAVYFKEQ and RDAPEEEDHVL, corresponding to the N-terminal region of the arginylated mature proteins through a custom service at AbFrontier Inc. (Seoul, South Korea), as described previously [20]. Rabbit polyclonal mATE1 antibody was raised by expressing a 22-kDa fragment corresponding to residues 313 to 516 through a custom service in AbFrontier Inc. (Seoul, South Korea). The antibodies were purchased: rabbit monoclonal anti-BiP (Cell Signaling, 3177), rabbit polyclonal anti-BiP (Abcam, ab21685), mouse monoclonal anti-calreticulin/CRT (BD Biosciences, 6121360), rabbit polyclonal anti-PDI (Cell Signaling, 2446S), mouse monoclonal anti-ATE1 (Santa Cruz, sc-271220), rabbit polyclonal anti-ATE1 (Sigma, HPA038444), mouse monoclonal anti-STING (Abcam, ab131604), rabbit monoclonal anti-IRF-3 (Cell Signaling, 11904P), rabbit polyclonal anti-IRF-3 (Santa Cruz, sc9082), rabbit monoclonal anti-phospho-IRF-3 (Ser396) (Cell Signaling, 4947S), rabbit polyclonal anti-KDEL (Santa Cruz, sc33806), mouse monoclonal anti-KDEL (Abcam, ab12223), mouse monoclonal anti-p62 (Santa Cruz, SC-28359), mouse monoclonal anti-CHOP (Cell Signaling, 2895), mouse monoclonal anti-Flag (Sigma, f1804), mouse monoclonal anti-CMV IE1 (Virusys corporation, CH443), mouse monoclonal anti-HSV-1 anti-ICP0 (Virusys corporation, H1A027-100), mouse monoclonal anti-HSV-1 gC-1 (Virusys corporation, H1A022-100), mouse monoclonal anti-HSV-1 UL42 (Santa Cruz, sc53331), and rabbit polyclonal anti-GAPDH (Santa

Cruz, sc25778). The following secondary antibodies were purchased: Rhodamine Red donkey anti-rabbit IgG (Jackson lab, 711-295-152), FITC goat anti-rabbit IgG (Novex, A24532), FITC goat anti-mouse IgG (Novex, A24513), anti-rabbit IgG–HRP (Cell Signaling, 7074), and anti-mouse IgG–HRP (Cell Signaling, 7076). The following secondary antibodies were obtained from Invitrogen: Alexa Fluor 488 goat anti-rabbit IgG (A11034, 1:200), and Alexa Fluor 555 goat anti-mouse IgG (A21424, 1:200). Normal goat serum (ab7481) was obtained from Abcam. Hoechst 33342 (H21492) was obtained from Invitrogen. 4′,6-Diamidino-2-phenylindole dihydrochloride (DAPI; D8417) was obtained from Sigma. Vectashield antifade mounting medium (H1000) was from Vector lab. All other chemicals were reagent grades from Sigma or Merck.

5.2.2 Plasmids and other reagents

The plasmids encoding ATE1^{1A7A} were generated as previously described [20]**.** pCMV-Sport6-hSTING (Thermo scientific, 5762441), human STING-Myc-Flag-tagged plasmid (OriGene, RC208418), and pRL-SV40-*Renilla*-luciferase control vector (Promega, E2231) were purchased. IgK–IFN-Luciferase reporter vector was a gift from David Baltimore (Addgene, #14886) [157]. The mammalian expression plasmids for N-terminal HA-tagged or untagged IE1 (wild-type or mutant) were described previously [158]. The wild-type and mutant IE1 DNAs (Towne strain) were cloned into pENTR vectors (Invitrogen). Retroviral vectors encoding wild-type or mutant IE1 were produced by transferring the IE1 DNAs from pENTR vectors to pMIN-based destination vector using LR Clonase (Invitrogen). Other reagents were purchased as follow: poly(dA:dT) (InvivoGen, #tlrl-patn), tannic acid (Sigma, 403040), RNAiMax (Invitrogen, 13778), Lipofectamine LTX (Invitrogen, 15338), Lipofectamine 2000 (Invitrogen, 11668), protein A/G plus agarose beads (Santa Cruz, sc2003), Pierce IP lysis buffer (Thermo Scientific, 87788), and dual-luciferase reporter assay system (Promega, E1910).

5.2.3 Cell culture

HEK293 and CCL2 HeLa cells were purchased from the American Type Culture Collection (ATCC). HEK293, HeLa, and MEFs cells were cultured in Dulbecco's Modified Eagle's Medium (DMEM; Gibco,10566016) supplemented with 10% FBS (HyClone) and 100 U/ml penicillin/streptomycin (Gibco, 15140-148). Cells were transfected with the plasmids and poly(dA:dT) using Lipofectamine LTX (Invitrogen, 15338). Tannic acid was treated for each time indicated in the figure legends. All the cell lines were determined to be negative in a mycoplasma test using a MycoAlert detection kit (Lonza, LT07-118). All the culture plates and the cell lines were maintained at 37°C and 5% CO_2 in a humidified incubator.

The HCMV Towne virus stocks were prepared as previously described [159]. For comparative analysis, the stocks of wild-type virus, IE1-deledeted CR208 virus, and other IE1 mutant viruses encoding IE1(Δ290–032) or IE1(Δ421–475) were prepared in IE1-expressing HeLa cells and the titers of virus stocks were determined as infectious units (IFU) after performing infectious center assays in normal HeLa cells (see below). To produce UV-inactivated HCMV (UV-HCMV), the virus stock was irradiated with UV light three times at 0.72 J/cm2 using a CL-1000 cross-linker (UVP).

5.2.4 Infectious center assays

The infectious center assays were prepared as previously described [158]. Briefly, the diluted samples were used to inoculate a monolayer of HeLa cells (1 x 10^5) in a 24-well plate. At 24 h post-infection, cells were fixed with 500 µl of cold methanol for 10 min. Cells were then washed three times in PBS, incubated with anti-IE1 antibody in PBS at 37°C for 1 h, followed by incubation with secondary antibody. Finally, the samples were washed in PBS and treated with 200 µl of nitro blue tetrazolium/5-bromo-4-chloro-3-indolylphosphate (KPL) for 1 h, according to the manufacturer's instructions. The IE1-positive cells were counted in at least three to five separate fields per well under a light microscope (200X magnification).

5.2.5 Immunoblotting and co-immunoprecipitation

For immunoblotting, cells were lysed in NETN buffer (0.5% Nonidet P-40, 20 mM Tris pH 8.0, 50 mM NaCl, 50 mM NaF, 100 µM Na_3VO_4, 1 mM EDTA, and 50 µg/ml PMSF). Cell lysates were subjected to SDS-PAGE. Immunoblotting was performed using the antibodies indicated in the figure legends. For Co-immunoprecipitation, cells were washed with ice-cold PBS and then lysed in Pierce IP lysis buffer (Thermo Scientific, 87787) with cOmplete protease and phosSTOP phosphatase inhibitor cocktail tablets (Roche) at 4°C for 10 min. Crude lysates were cleared by centrifugation at 14,000 rpm at 4°C for 5 min, and supernatants were incubated with protein A/G plus agarose beads with primary antibodies. The immune-complexes were washed three times with NETN buffer and subjected to SDS-PAGE. Western blotting was performed using the antibodies indicated in the figure legends.

5.2.6 Immunocytochemistry of cultured cells

Cells were cultured in chamber slides (Thermo Fisher, 154461PK) or poly-L-lysine coated slides, as described previously [24]. Cells were fixed in 4% PFA in PBS, for 30 min at room temperature. After washing twice with PBS, the cells were incubated for 1 h in blocking solution (5% normal goat serum and 0.2% Triton X-100 in 0.1 M PBS). After blocking, cells were incubated with primary antibodies and subsequently secondary antibodies. Confocal images were taken with a Zeiss LSM 700 laser scanning confocal microscope equipped with Zeiss C-Apochromat 60 × (1.2 NA) and 40 × (1.2 NA) water immersion lens and analyzed using ZEN (black edition) 2012 SP5 software (Zeiss). Image processing and annotation was done with Adobe Photoshop, Adobe Illustrator and Fiji software [103]. ImageJ plugin, interactive 3D surface plot (by Kai Uwe Barthel), was used to evaluate localization and expression of fluorescent images.

5.2.7 Luciferase reporter assays

Cells were plated on 12-well plates (5×10^5 cells/well) were transiently transfected with 100 ng IgK–IFN β-Luc with or without poly(dA:dT) with Lipofectamine 2000. At 24 h after transfection, luciferase activities were measured using Dual-luciferase reporter assay system and Wallac VICTOR 2 (Perkin Elmer). A *Renilla* luciferase reporter plasmid (50 ng) was used as an internal control.

5.2.8 RNA interference assay

Cells in a 6-well plate (1×10^6 cells/well) were transfected with 100 pmol of siRNA using the RNAiMax reagent. Pre-designed Silencer Select siRNAs (Invitrogen) were used to knock down *ATE1* and *BiP* using the following sequences (Table 4). A negative control oligo (#4390843) was purchased from Invitrogen. Approximately 48 h after siRNA silencing, cells were harvested for immunoblotting and immunocytochemical analyses.

Table 4: siRNA nucleotide sequences

Target mRNA	Hairpin siRNA sequences
ATE1 (HSS117-202)	Sense: 5’-GAUUCCUUUGCAGUUCACCCUUGGA-3’
	Antisense: 5’-UCCAAGGGUGAACUGCAAAGGAAUC-3’
ATE1 (HSS117-203)	Sense: 5’-GAGAGCCAUGCCUUACGGUGUU-3’
	Antisense: 5’-AACACCGUAAGGCAUGAUGGCUCUC-3’
ATE1 (HSS117-204)	Sense: 5’-ACCCACCAUCUUUGUUUCCACCAAA-3’
	Antisense: 5’-UUUGGUGGAAACAAAGAUGGUGGGU-3’
BiP	Sense: 5’-CAGAUGAAGCUGUAGCGUATT-3’
	Antisense: 5’-UACGCUACAGCUUCAUCUGGG-3’

5.2.9 Statistical analysis

All numerical data are presented as means ± SEM or mean percentages ± SEM. Western blots shown are representative of three or more independent experiments. Comparisons among treatment groups were performed with one-way ANOVA and Tukey test or Dunnett’s multiple comparison as a post hoc comparison. Instances involving only two comparisons were evaluated with unpaired t-test or two-tailed Mann-Whitney test for non-parametric test. Statistical significance was accepted if the null hypothesis was rejected with $p < 0.05$. All statistical analyses were determined using Prism 7.0c software (GraphPad, La Jolla, CA).

5.3 EXPERIMENTAL RESULTS

5.3.1 ATE1 is essential for cytosolic dsDNA-mediated immune response.

A previous our study reported that cytosolic foreign dsDNA induces arginylation of ER chaperones like BiP, CRT, and PDI [20]. Here, we also confirmed that the ATE1-depedent Nt-Arg was induced by cytosolic dsDNA. Arginylated forms of BiP (R-BiP), CRT (R-CRT), and PDI (R-PDI) were induced by cytoplasmic foreign dsDNA exposure, time- and dose-dependently (Figure 37A and B). We further validated whether the transfected poly(dA:dT) leads to cellular immune response through the detection of phosphorylated IRF-3 on Ser396. Immunoblotting assay showed that cytoplasmic foreign dsDNA exposure facilitated phosphorylation of IRF-3 in a time-dependent manner (Figure 37B).

Cytosolic dsDNA causes innate immune response through interaction of cytosolic dsDNA sensors and induces production of type I interferon [143, 154]. To characterize a potential link between ATE1 and innate immune response, we performed the interferon beta (IFN-β) reporter assay. The IFN-β reporter assay revealed that transiently downregulated ATE1 restrained the poly(dA:dT)-induced activation of the IFN-β promoter (Figure 37C). Furthermore, the reduced IFN-β activation was rescued by overexpression of ATE1^{1A7A}, an ATE1 isoform (Figure 37D). Consistently, transfection of poly(dA:dT) induced IFN-β-mediated reporter gene activity in +/+ MEF cells, but not in *ATE1*$^{-/-}$ MEFs (Figure 37E). These results suggest that ATE1 is involved in cytoplasmic dsDNA-triggered induction of downstream innate immune genes.

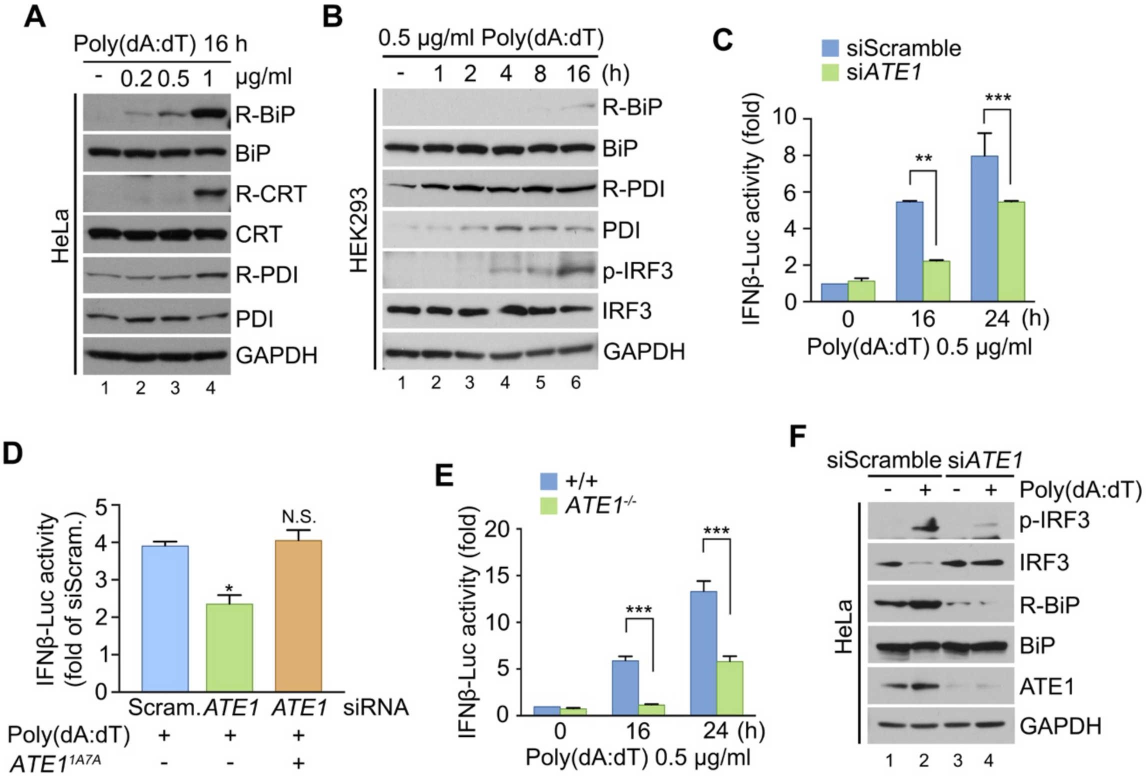

Figure 37: ATE1 is essential for cytosolic dsDNA-mediated immune response.

(A) Immunoblotting analysis of R-BiP, R-CRT, and R-PDI in poly(dA:dT)-treated HeLa cells. The Nt-Arg of BiP, CRT, and PDI is induced by cytosolic dsDNA in a dose-dependent manner. GAPDH is probed for loading control. (B) Immunoblotting analysis of R-BiP, R-CRT, R-PDI, pho-IRF, and IRF in poly(dA:dT)-treated HEK293 cells. The Nt-Arg of BiP, CRT, and PDI caused by cytosolic dsDNA is promoted in a time-dependent manner. Cytosolic dsDNA facilitates phosphorylation of IRF3 on Ser396. (C) IFN-β reporter assays for untreated or si*ATE1*-treated HeLa cells and then transfected with poly(dA:dT) for indicated times. (D) IFN-β reporter assays for siScramble- or si*ATE1*-treated HeLa cells and then transfected with poly(dA:dT) or ATE1^{1A7A}. (E) IFN-β reporter assays for +/+ and *ATE1*$^{-/-}$ MEF cells transfected with 0.5 μg/ml poly(dA:dT) for indicated times. (F) Immunoblotting analysis of pho-IRF3, IRF3, R-BiP, BiP, and ATE1 in siScramble- or si*ATE1*-treated HeLa cells followed by transfection with or without poly(dA:dT) for 16 h. GAPDH is probed for loading control. Conducted by Kisa Sung.

To determine whether ATE1 is required for cytoplasmic dsDNA-triggered immune signaling, we examined phosphorylation of IRF3 that is an upstream of IFN-β signlaing induced by poly(dA:dT) transfection. RNA interference assays revealed that phosphorylation of IRF3 induced by poly(dA:dT) transfection was markedly inhibited by transient deletion of ATE1 in HeLa cells (Figure 37F, lanes 2 versus 4). Collectively, these suggest that ATE1 can be indispensible for efficient indection of genes by cytosolic DNA in cellular immune system.

5.3.2 Cytosolic dsDNA facilitates relocation of ATE1 to the ER.

To determine the function of ATE1 on cellular immune response caused by cytosolic DNA, we examined the intracellular localization of ATE1. Immunostaining assay showed that transfection of poly(dA:dT) induced ATE1 and caused ATE1$^+$ puncta structures, which were accumulated on KDEL$^+$ ER in HeLa cells (Figure 38). Additionally, 3D surface plot analysis markedly revealed that ATE1$^+$ puncta were translocated to KDEL$^+$ ER by poly(dA:dT) treatment (Figure 38C). Tannic acid treatment for 24 h, an ATE1 inhibitor, caused dislocalization of ATE1 puncta from the ER (Figure 38B-D). It suggests that the inhibitor did not induce a degradation of ATE1, but it may caused conformational changes preventing its attachment to target substrate. Transient deletion of ATE1 by RNA interference assay reduced a basal level of ATE1 and its puncta (Figure 38B). These results suggest that cellular immune response caused by poly(dA:dT) induced the translocation of ATE1 to the ER.

5.3.3 Tannic acid, an ATE1 inhibitor, suppresses the trafficking of STING.

STING, an ER-associated protein, is a critical signaling molecule in the innate response to cyto-

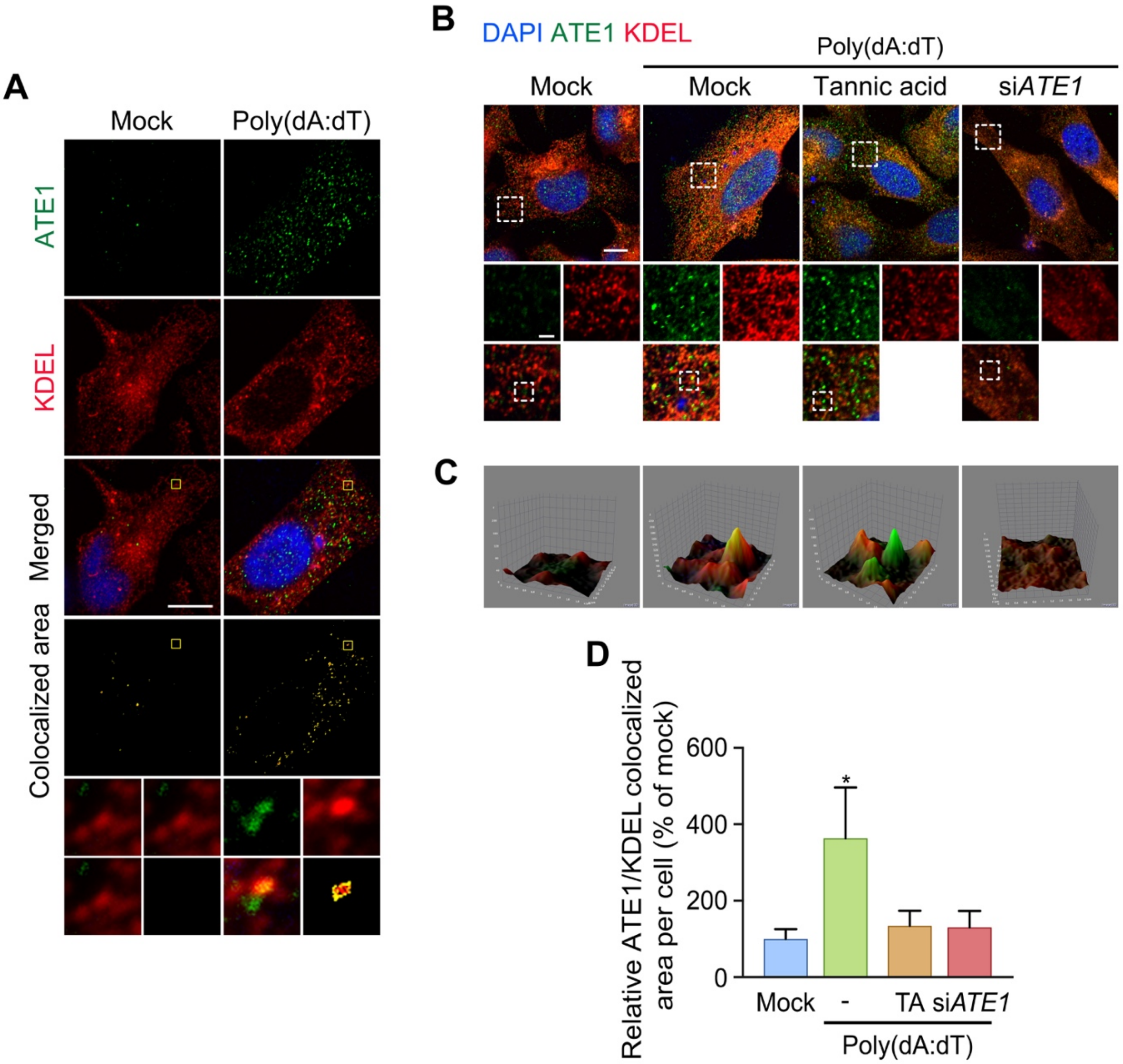

Figure 38: Cytosolic dsDNA facilitates relocation of ATE1 to the ER.

(A) Immunostaining analysis of ATE1 and KDEL (ER marker) in HeLa cells transfected with or without 1 μg/ml poly(dA:dT) for 18 h (scale bar = 10 μm). Enlarged views of areas indicated by rectangles. Colocalized area were shown as a central red area, surrounded by yellow ring. (B) Immunostaining analysis of ATE1 and KDEL in tannic acid (TA)- and si*ATE1*-treated HeLa cells, follwed by transfection with or without 1 μg/ml poly(dA:dT) for 18 h (scale bar = 10 μm). (C) Interactive 3D surface plot assay of B to evaluate the localization of ATE1^{+} puncta. (D) Quantification of B, representing the relative colocalized area between ATE1 and KDEL per cell (**p = 0.0317,* n = 6-16 in each group). Data are presented as mean percentage ± SEM of mock. Statistical significance was determined using one-way ANOVA and Tukey test as a post hoc comparison.

solic nucleic acids like dsDNA [155]. Because STING trafficking from the ER to Golgi apparatus via ERGIC (ER-Golgi intermediate compartment) is essential for its activation mechanism [156], we thus determined whether the relocalization of ATE1 from the cytosol to the ER is involved in the STING trafficking during the cytoplasmic dsDNA-induced immune response. We transiently transfected STING-Myc-Flag plamid in HEK293T cell and performed immunostaining with various primary antiobodies against STING, Myc, and Flag respectively. Consistently, all these antibodies showed that STING was constituitively located on the ER in HEK293T cells stably expressing ER-DsRFP (ER marker) (Figure 39A). Upon poly(dA:dT)-mediated immune response, immunostaining assay showed that dsDNA-induced ATE1 were aggregated and colocalized with STING, which was located on the ER membrane (Figure 39B).

Next, we investigated whether the pharmaceutical inhibition of ATE1 using tannic acid suppresses the trafficking of STING. Immunostaining assay showed that most of STING were aggregated and strongly colocalized with ERGIC53 (ERGIC marker), indicating translocation of STING within 8 h from poly(dA:dT) transfection (Figure 40A). We also observed that the translocation of STING to Golgi using GM130 antibody, which is a Golgi marker, in a timely manner (Figure 40B). Notably, tannic acid treatment inhibited the trafficking of STING to either of the ERGIC or the Golgi. These results indicate that the ATE1 can mediate dsDNA-induced translocation of STING, which plays a key role in cellular immune reponse against pathegens.

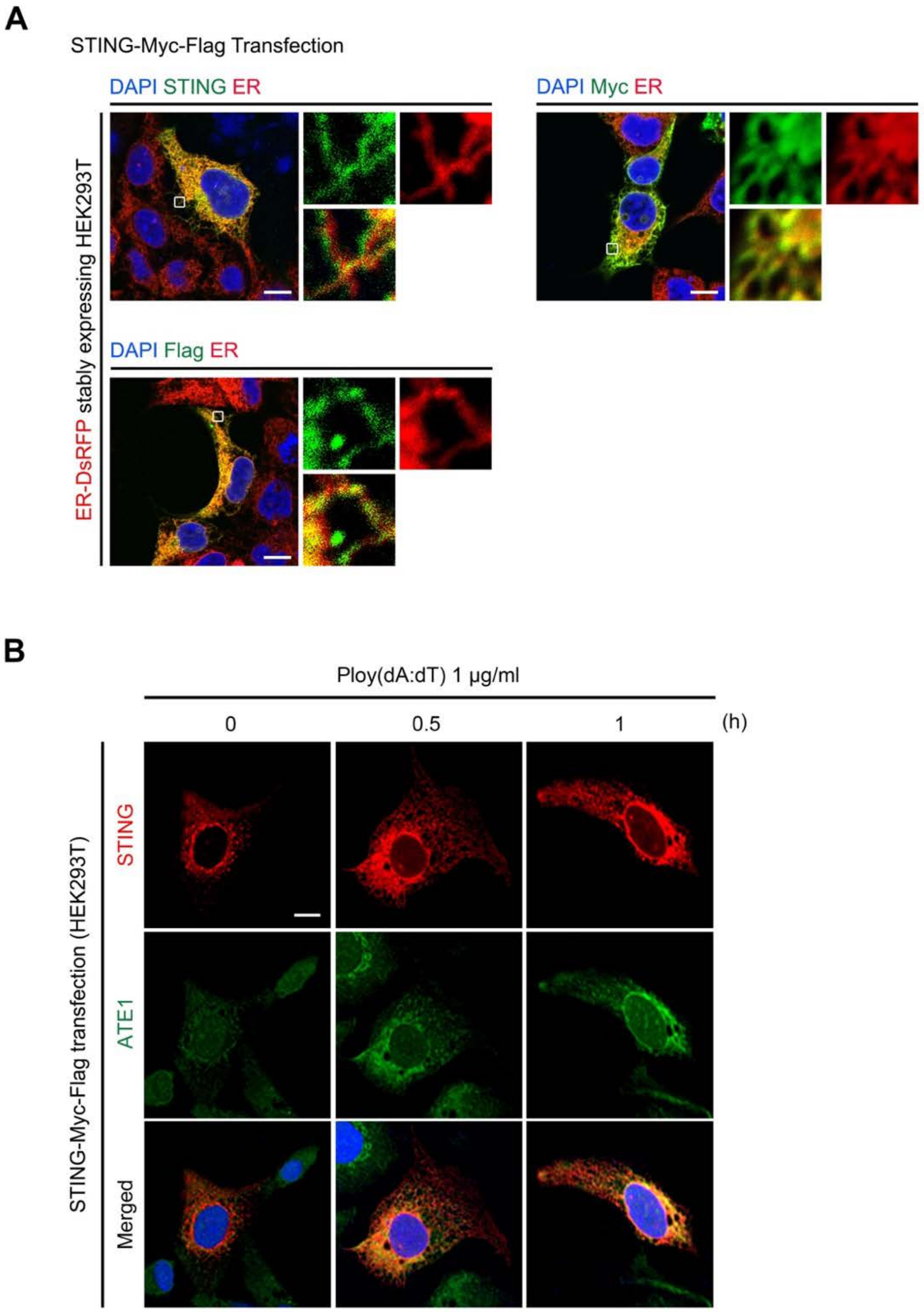

Figure 39: ATE1 is co-localized with STING on the ER.

(A) Immunostaining analysis of STING, Myc, and Flag in transiently STING-Myc-Flag transfected HEK293T cells stably expressing ER-DsRFP (ER marker). STING is constitutively located on the ER. Enlarged views show the areas indicated by white rectangles (scale bar = 10 μm). (B) Immunostaining analysis of STING and ATE1 in transiently STING-Myc-Flag transfected HEK293T cells, follwed by transfection with or without 1 μg/ml poly(dA:dT) for indicated times (scale bar = 10 μm).

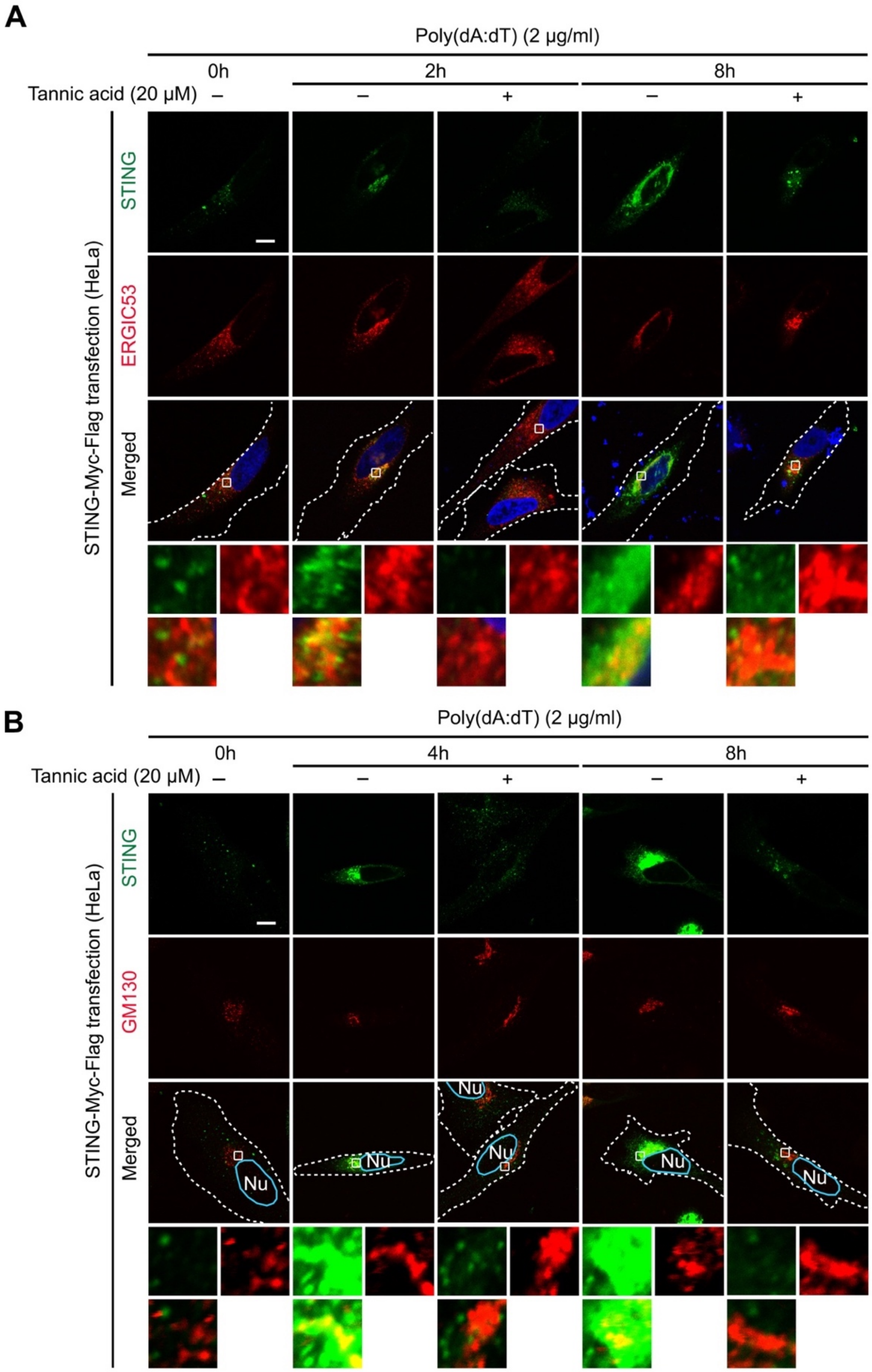
A
Poly(dA:dT) (2 µg/ml)
0h
2h
8h
Tannic acid (20 µM)
–
–
+
–
+
STING-Myc-Flag transfection (HeLa)
STING
ERGIC53
Merged
B
Poly(dA:dT) (2 µg/ml)
0h
4h
8h
Tannic acid (20 µM)
–
–
+
–
+
STING-Myc-Flag transfection (HeLa)
STING
GM130
Merged
Nu
Nu
Nu
Nu
Nu
Nu

Figure 40: ATE1 is reqired for the STING trafficking.

(A) Immunostaining analysis of STING and ERGIC53 (ERGIC marker) in untreated or 20 μM tannic acid-treated transiently STING-Myc-Flag transfected HeLa cells, follwed by transfection with 2 μg/ml poly(dA:dT) for indicated times. White dotted lines delineate the cell boundary. Enlarged views show the areas indicated by white rectangles (scale bar = 10 μm). (B) Immunostaining analysis of STING and GM130 (Golgi marker) in untreated or 20 μM tannic acid-treated transiently STING-Myc-Flag transfected HeLa cells, follwed by transfection with 2 μg/ml poly(dA:dT) for indicated times. White dotted lines delineate the cell boundary. Cyan lines delineate the nucleus. Nu, nucleus. Enlarged views show the areas indicated by white rectangles (scale bar = 10 μm).

5.3.4 Nt-arginylation of BiP is needed for STING-mediated immune response.

Cytoplasmic dsDNA facilitates Nt-arginylation of BiP, a major substrate of ATE1 (Figure 37A). To understand the correlation between induced R-BiP and STING-IRF3 signaling, we perfomed a co-immunoprecipitation (co-IP) assay in HeLa cells. The IP of STING co-precipitated BiP (Figure 41A, lanes 4 versus 5), but the interaction of STING with BiP was not enhanced when the cells were transfected with poly(dA:dT) for 16 h (Figure 41A, lanes 5 versus 6). To check whether BiP mediates STING-IRF3 immune signaling, we transiently silenced BiP using siRNA. Poly(dA:dT) transfection induced pho-IRF3, which was downstream of STING signaling (Figure 41B; lanes 1 vs. 2), but si*BiP* transfection interrupted the phosphorylation of IRF3 (Figure 41B; lanes 2 vs. 4).

We further determined whether R-BiP is a deteminant of STING signaling. Immunostaining assay showed that STING was induced at first within a hour and significantly colocalized with cytosolic puncta for R-BiP later, which were markedly detected at 8 h from poly(dA:dT) transfection (Figure 41C and D). Whereas the colocalization was maximized at 8 h, accumulated STING$^+$ puncta were disappreared at 16 h from the dsDNA-induced stress (Figure 41D). The ATE1 inhibitor tannic acid treatment prevented the co-induction and colocalization of STING$^+$ and R-BIP$^+$ puncta (Figure 41C and D). These suggest that ATE1 and R-BiP may be necessary for STING translocation in cytoplasmic DNA-mediated response.

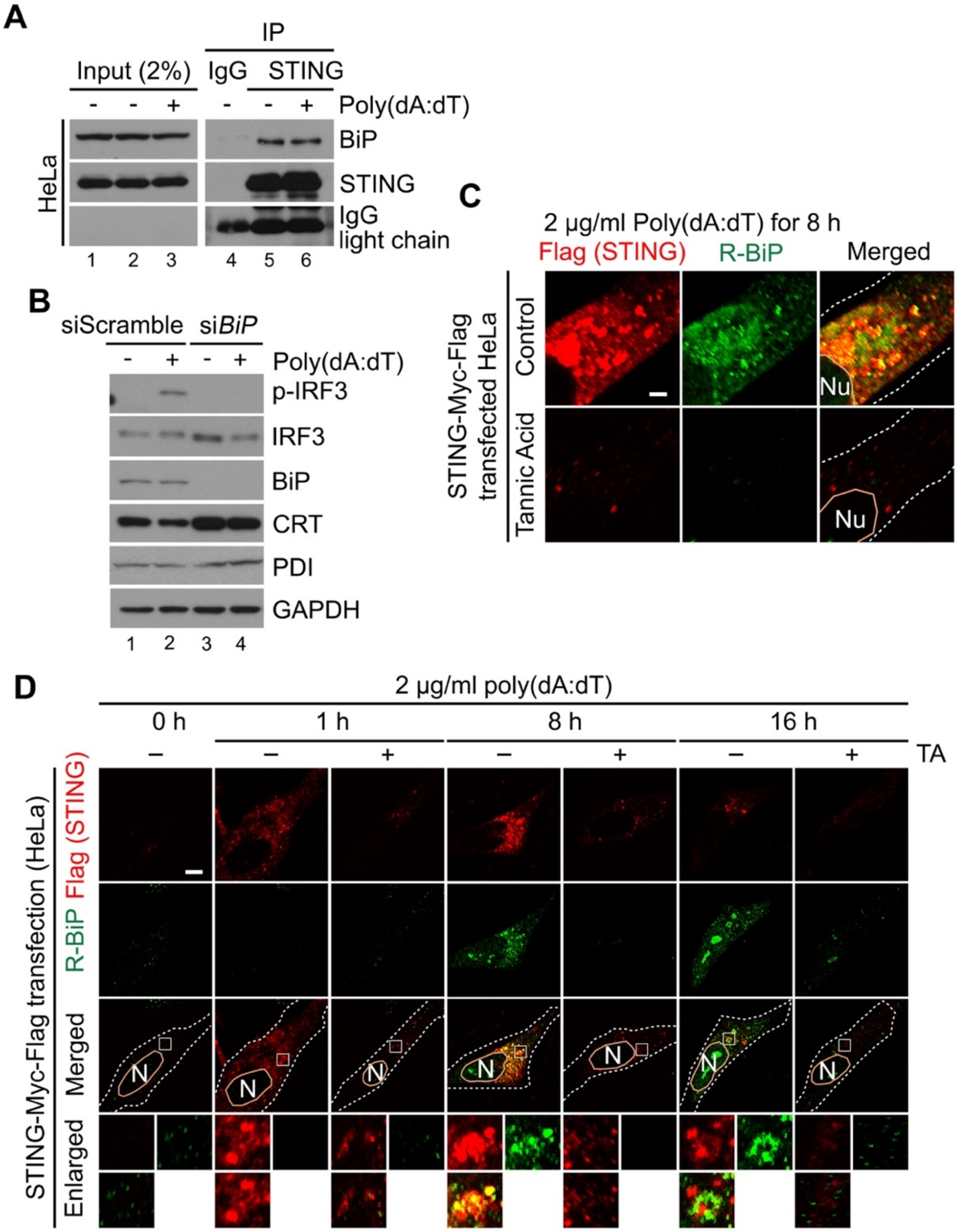

Figure 41: BiP binds STING and its Nt-arginylation is essential for STING trafficking.

(A) Co-immunoprecipitation assay in HeLa cells. Cell lysates were immunoprecipitated with anti-STING antibody and then immunoblotted with indicated antibodies. (B) Immunoblotting analysis of pho-IRF3, IRF, BiP, CRT, and PDI in HeLa cells transfected with the indicated siRNAs. (C) Immunostaining analysis of STING and R-BiP in untreated or 20 μM tannic acid-treated transiently STING-Myc-Flag transfected HeLa cells, followed by transfection with 2 μg/ml poly(dA:dT) for 8 h. White dotted lines delineate the cell boundary. Orange lines delineate the nucleus.

Nu, nucleus (scale bar = 1 μm). (D) Immunostaining analysis of STING and R-BiP in untreated or 20 μM tannic acid-treated transiently STING-Myc-Flag transfected HeLa cells, followed by transfection with 2 μg/ml poly(dA:dT) for indicated times. White dotted lines delineate the cell boundary. Orange lines delineate the nucleus. N, nucleus. Enlarged views show the areas indicated by white rectangles (scale bar = 4 μm). Panels A and B were conducted by Kisa Sung.

5.3.5 ATE1 is essential for anti-viral response.

Collectively, these data imply that ATE1-dependent Nt-arginylation can play a important role in host defense system against pathogens. Among various pathogens, we speculated that ATE1 is critical for sensing DNA virus beacuase Nt-arginylation was not induced by cytoplasmic ssRNA and dsRNA [20]. Therefore, we infected HeLa cells with human cytomegalovirus (HCMV), a DNA virus. ATE1-deficient HeLa cells using sh*ATE1* produced 110-fold-more infectious virus, compared with that of shScramble transfected cells (Figure 42A and B). Because the infectivity of the virions produced by ATE1 knockdown was hugely increased, we examined the viral protein constituents of +/+ and *ATE1*$^{-/-}$ MEFs cells infected with herpes simplex virus-1 (HSV-1). Immunoblotting assay showed that ICP0, gC-1, and UL42 were highly expressed in *ATE1*$^{-/-}$ MEFs (Figure 42C). These data suggest that ATE1 is essential for host defense against virus-infection in cultured cell lines.

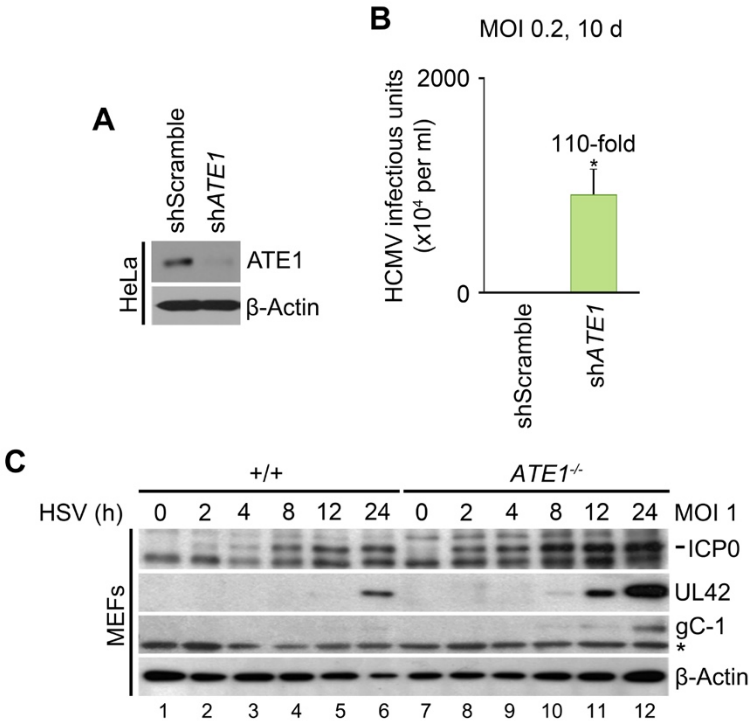

Figure 42: ATE1 is essential for host defense system against DNA virus.

(A) Immunoblotting analysis of ATE1 in HeLa cells transfected with the indicated shRNAs. (B) Infectious center assay of measuring virus titers in shScramble or sh*ATE1*-transfected HeLa cells, followed with HCMV infection at a multiplicity of infection (MOI) of 0.2 for 10 d. ATE1-deletion in HeLa cells produces 110-fold-more infectious progeny than shScramble transfected cells. (C) Immunoblotting analysis of ICP0, gC-1, and UL42 in +/+ and *ATE1*$^{-/-}$ MEFs infected with HSV-1 at a MOI of 1 for the indicated times. Panels A and B were conducted by Jin-Hyun Ahn and panel C was conducted by Daeho Kim.

5.3.6 STING is targeted to p62 for autophagy-lysosomal degradation.

Because sustained activation of STING can cause autoinflammatory diseases [160, 161], clearing of activated STING is necessary for cellular homeostasis, even though it's beneficial functions to detect and promote immune response against pathogens and viral DNA. In addition, we recently reported that various Nt-arginylated proteins including ER-residing and cytoplasmic proteins bind p62 and induce its self-oligomerization through their binding to ZZ domain of p62, which promotes cargo deliveries for autophagy-lysosomal degradation [9, 20]. According to the co-induction and colocalization of STING and R-BiP upon dsDNA-induced stress (Figure 41A and B), STING/R-BiP complex may enhance autophagy activity and be targeted to p62-LC3-mediated autophagic degradation via binding to ZZ domain of p62. We thus determined whether Nt-arginylation facilitates the interaction of STING with p62 in transiently STING-Myc-Flag transfected HeLa cells. The immunostaining analysis showed that most of STING$^+$ puncta colocalized with cytosolic puncta postive for p62 as well as LC3 at 16 h from cytoplasmic dsDNA exposure (Figure 43A). However, tannic acid treatment impaired co-localization of STING with p62 (Figure 43A). Consistent with the previous results, STING was highly co-induced and colocalized with the LC3 and p62 at 8 h after poly(dA:dT) transfection, and these STING$^+$-LC3$^+$-p62$^+$ puncta were disappeared in a time-dependent manner, from 8 to 16 hour (Figure 43B). Thus, it suggests that a portion of acivated STING was targeted to p62 for autophagic degradation during dsDNA immune response.

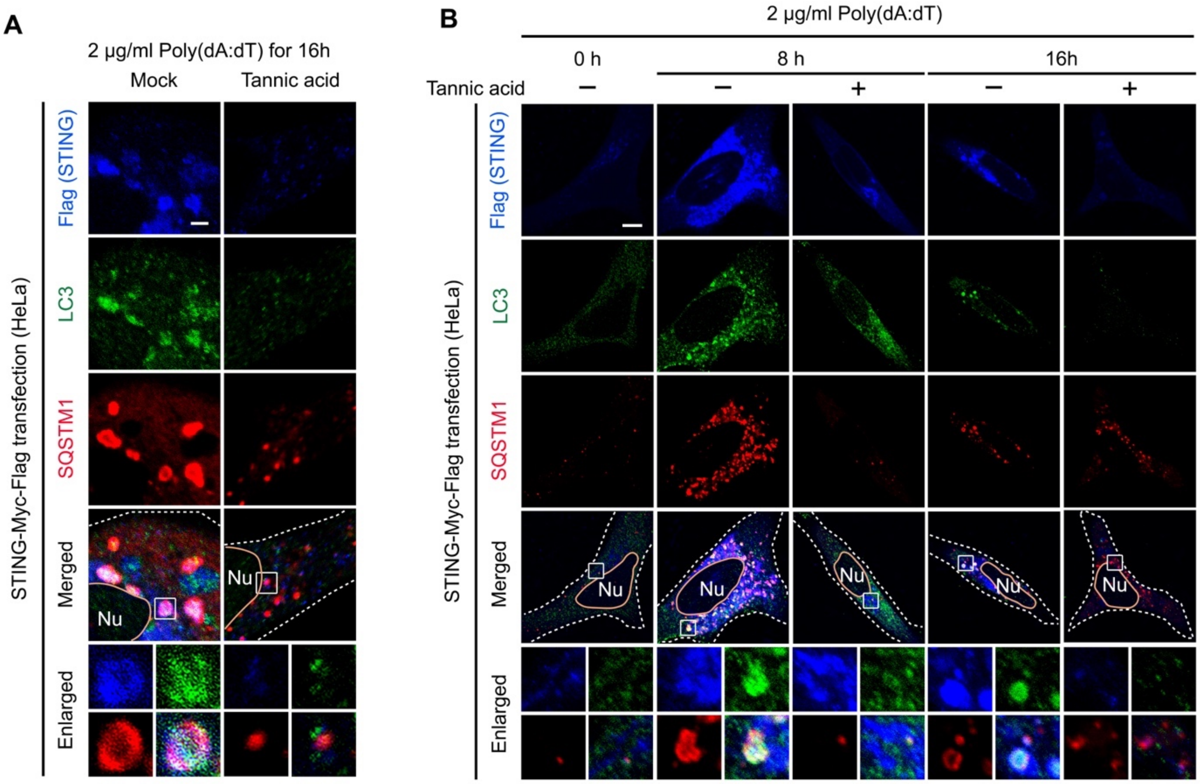

Figure 43: STING is targeted to p62 for autophagy-lysosomal degradation.

(a) Immunostaining analysis of STING, LC3, and p62 in untreated or 20 μM tannic acid-treated transiently STING-Myc-Flag transfected HeLa cells, follwed by transfection with 2 μg/ml poly(dA:dT) for 16 h. White dotted lines delineate the cell boundary. Orange lines delineate the nucleus. Nu, nucleus. Enlarged views show the areas indicated by white rectangles (scale bar = 1 μm). (b) Immunostaining analysis of STING, LC3, and p62 in untreated or 20 μM tannic acid-treated transiently STING-Myc-Flag transfected HeLa cells, follwed by transfection with 2 μg/ml poly(dA:dT) for indicated times. White dotted lines delineate the cell boundary. Orange lines delineate the nucleus. Nu, nucleus. Enlarged views show the areas indicated by white rectangles (scale bar = 4 μm).

5.4 DISCUSSION AND CONCLUSION

N-terminal Arg (Nt-Arg) is one of the principal degrons that it can be generated through post-translational conjugation of L-Arg from Arg-tRNA^{Arg} to N-terminal Asp or Glu, which is mediated by *ATE1*-encoded Arg-tRNA transferases. Additionally, the Nt-Arg can be generated by endoproteolytic cleavages or enzymatically through the modification of Nt-Asn, Nt-Gln, Nt-Cys, Nt-Asp, and Nt-Glu [12-15]. The resulting Nt-Arg residue is recognized by N-recognins like UBR box proteins (UBR1, UBR2, UBR4/p600, and UBR5/EDD), resulting induced substrate ubiquitination and its proteasomal degradation via the N-end rule pathway of the UPS. Recently we reported that Nt-Arg residues can modulate proteolytic flux via macroautophagy when misfolded proteins accumulate beyond the UPS's capacity [20]. The Nt-Arg binds and activate the autophagic receptor p62, promoting cargo delivery to phagophore/autophagosome [8, 9, 20]. Even though it is a universal posttranslational modification in eukaryotes, yet its functions remain poorly understood.

In this chapter, we show that cytosolic foreign DNA induces Nt-arginylation of ER chaperons. ATE1-dependent Nt-arginylation is required for STING-mediated cellular immune response, which leads to IRF3 phosphorylation and IFN-β mediated gene induction. In addition, Cytosolic dsDNA facilitates relocation of ATE1 to the ER, on which ATE1 is colocalized with STING. Either transient deletion of ATE1 or its pharmaceutical inhibition with tannic acids hinders the trafficking of STING from the ER to the Golgi compartment on which STING makes a complex with TBK1 and IRF3. To prevent retained STING activity to cause autoimmune response, activated STING complex on the Golgi compartment can be targeted and eliminated by p62-mediated autophagy. Interference of Nt-arginylation that is important for host defense induces virion production. Collectively, our results suggest that Nt-arginylation is essential for cellular immune response against foreign DNA and viral infections.

STING can directly recognize cytoplasmic foreign DNA or indirectly through various DNA sensors including, cytosolic GMP-AMP (cGAMP) synthase (cGAS) [151]. Recent studies showed that activated STING in response to cytoplasmic DNA is translocated from the ER to the Golgi compartment, on which it recruits TANK-binding kinase 1 (TBK1) and the transcription factor IFN regulatory factor 3 (IRF3), leading to NF-κB and type I IFN gene expression (Figure 44) [155, 156]. We found that ATE1-dependent Nt-arginylation is essential for translocation of STING from the ER and its downstream signaling (Figures 37 and 40). In other way, cytoplasmic DNA infection facilitates translocation of the ER-residing chaperone BiP and its Nt-arginylation at 8 h from the infection (Figure 41C and D). At that time, most of activated STING already aggregated on the Golgi on which STING activates the transcription factor IRF3 for IFN signaling (Figure 40). Given that R-BiP still maintains binding affinity to STING as BiP does (Figure 41A), R-BiP can bind and accumulate with activated STING complex on the Golgi. R-BiP additionally binds the ZZ domain of p62 and induces a conformational change of p62, resulting self-oligomerization and aggregation of p62. The autophagy receptor p62 interacts with LC3 embedded on the phagophore or autophagosome. This can bring the whole complex including STING-R-BiP-p62 into the phagophore and/or autophagosome, destined to be degraded by lysosomal fusion. Through the autophagic degradation of activated STING, it can prevent sustained STING activation which can lead to autoimmune diseases.

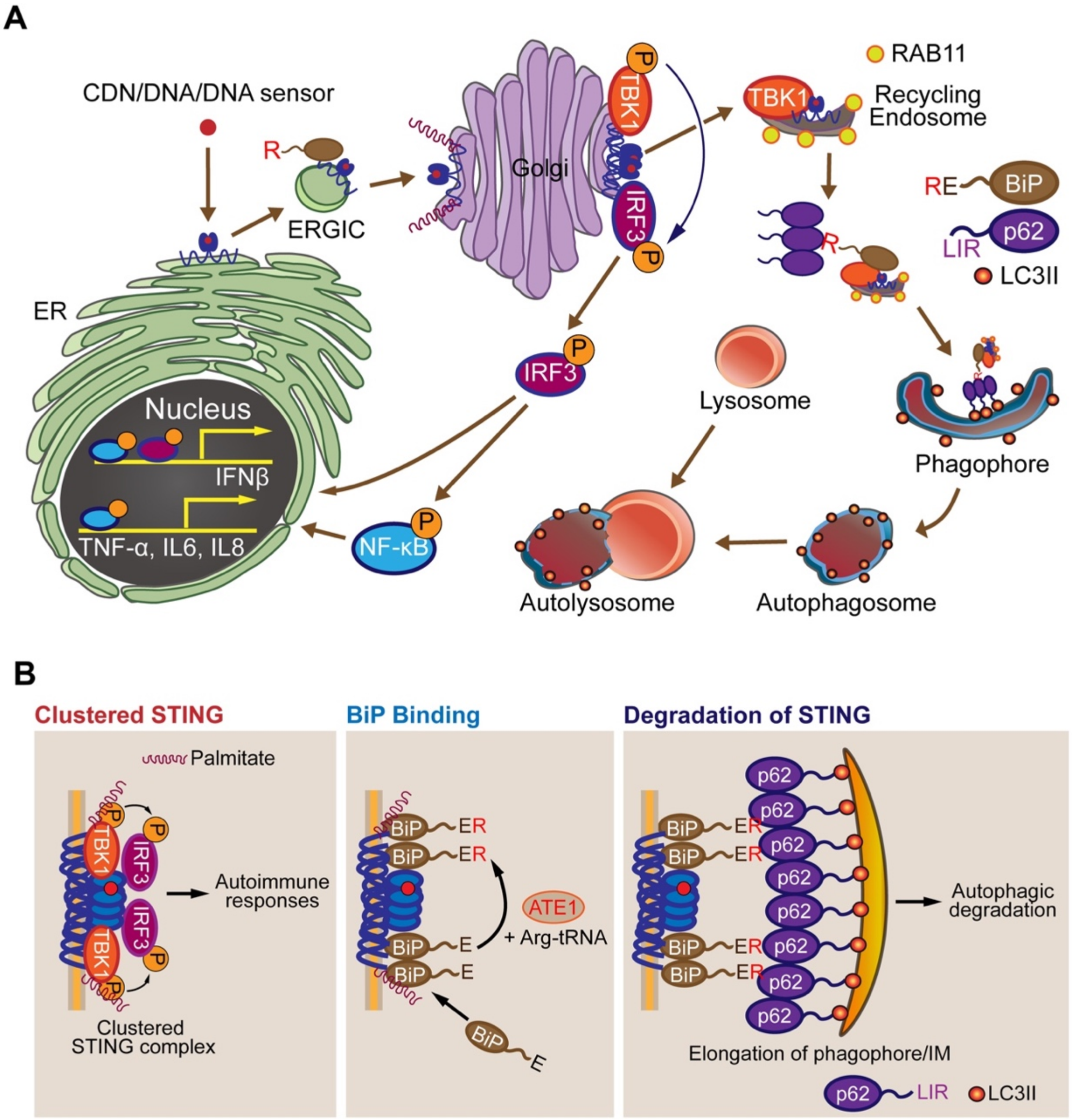

Figure 44: Schematic illustration of the N-end rule pathway in modulation of cytoplasmic DNA-mediated STING pathway.

(A) STING recognizes cytoplasmic foreign DNA and moves from the ER to the Golgi in which activated STING recruits TBK1 and IRF3 and activates downstream type I IFN signaling. Because constitutively activated STING leads to autoimmune response, p62-mediated autophagic degradation of the complex is needed to maintain cellular homeostasis. (B) A model for autophagic degradation of activated STING complex in the N-end rule pathway. Palmitation of activated STING complex on the Golgi can lead to its conformational changes and exposure of hydrophobic domains of STING, which can be bound by chaperone BiP. As an innate immune reaction, Nt-arginylation can be facilitated and add Arg to N-termini of BiP. The resulting Nt-Arg of BiP binds to the autophagy receptor p62, which promotes autophagic cargo deliveries to phagophore and the formation of autophagosome, destined to auto-lysosomal degradation.

6.0 CONCLUSION AND FUTURE DIRECTIONS

6.1 THE ROLE OF UBR4 IN AUTOPHAGIC MODULATION IN THE YOLK SAC

We have previously identified UBR4 as an N-recognin of the N-end rule pathway, which can bind the N-terminal residues of proteins to facilitate proteolysis via the ubiquitin-proteasome system or autophagy. In the current study, we addressed the physiological function of a poorly characterized N-recognin, 570-kDa UBR4, in mammalian development. UBR4-deficient mice show severe embryonic lethality associated with pleiotropic abnormalities in the YS. In the YS, UBR4 is highly enriched in endoderm-derived cell layer that supplies autophagy-generated amino acids during early embryogenesis. UBR4 of the YS endoderm is associated with a tissue-specific autophagic pathway that mediates autophagy-lysosomal proteolysis of endocytosed maternal proteins into amino acids. In cultured cells, UBR4 subpopulation is degraded by autophagy through its starvation-induced association with cellular cargoes destined to autophagic double membrane structures. UBR4 loss results in multiple misregulations in autophagic induction and flux, including synthesis and lipidation of LC3. Our results suggest that UBR4 plays an important role in mammalian development, in part through regulation of bulk degradation by lysosomal hydrolases in the YS.

The YS endoderm is a specialized digestive organ wherein maternal proteins from the YS cavity are endocytosed and digested into amino acids through the MVB-autophagosome-lysosome pathway [57]. The N-end rule pathway has been characterized as a proteolytic system that controls the half-lives of cytosolic short-lived proteins through selective proteolysis by the 26S proteasome. N-recognin, known to bind to substrates of selective proteasomal degradation, is also associated with substrates of bulk lysosomal degradation. Further investigation is needed to understand the mechanism by which UBR4 plays a dual role in selective degradation of short-lived proteins *via* the proteasome and bulk degradation of cellular materials *via* autophagy-lysosome degradation pathway.

6.2 THE ROLE OF THE N-RECOGNIN UBR4 IN THE BIOGENESIS OF THE EARLY ENDOSOME

Here, we show that the 570 kDa N-recognin UBR4 modulates endosome maturation and the trafficking and proteolysis of internalized cargoes. UBR4 is associated with endocytic vesicles through the interaction with Ca^{2+}-bound calmodulin. The endosomal recruitment of UBR4 is essential for the biogenesis of early endosomes and endosome-related processes such as the trafficking of endocytosed protein cargoes. In mouse embryos, UBR4 marks and plays a role in the endosome-lysosome pathway that mediates the heterophagic proteolysis of endocytosed maternal proteins into amino acids. Our results suggest that UBR4 is an essential modulator in the endosome-lysosome system.

Studies have implicated UBR4 in various biological processes, including neurodegeneration [8, 28], auxin transport, trafficking via microvesicles and ectosomes [51], synaptic transmission [47, 48], the interaction with various viral proteins across diverse strains [36], proteasomal degradation of short-lived regulators [43, 44] and E7-mediated cellular immortalization and transformation activities [39-42]. Despite rather extensive studies, however, little is known about the cellular functions of UBR4 that explain these seemingly unrelated observations. Given our findings that UBR4 is a key modulator in the biogenesis of early endosomes and endosomal proteolysis, the functions of UBR4 in various biological systems may need to be re-evaluated in the light of endosomal processes.

We have previously identified UBR4 as an N-recognin of the N-end rule pathway, which can bind the N-terminal residues of proteins to facilitate proteolysis via the ubiquitin-proteasome system or autophagy. Our current finding that UBR4 is associated with maturing endosomes through its binding to Ca^{2+}-calmodulin provides a model in which UBR4 modulates its function in the biogenesis of early endosomes. In this model, *ATE1* R-transferase conjugates L-arginine (L-Arg) of Arg-$tRNA^{Arg}$ to the N-termini of proteins. The resulting N-terminal Arg (Nt-Arg) residue acts as a ligand that binds the UBR box of UBR4, enabling UBR4 to bind Ca^{2+}-calmodulin and to be associated with $EEA1^{+}$ early endosomes. We will further investigate the model to verify that Nt-arginylation can be a determinant of biogenesis of early endosomes.

In addition, by screening 11,679 drugs through the DrugBank database, we identify picolinic acid as a putative ligand to UBR4, which inhibits the biogenesis of early endosomes. We want to further characterize its mechanisms in the endosome-lysosome system.

6.3 THE FUNCTION OF UBR4 IN NEUROGENESIS AND HOMEOSTASIS OF CELL SURFACE PROTEINS

The N-end rule pathway is a proteolytic system in which single N-terminal amino acids of proteins act as a class of degrons (N-degrons) that determine the half-lives of proteins. We have previously identified a family of mammals N-recognins (termed UBR1, UBR2, UBR4/p600, and UBR5/EDD) whose conserved UBR boxes bind N-degrons to facilitate substrate ubiquitination and proteasomal degradation via the UPS. Amongst these N-recognins, UBR1 and UBR2 mediate ubiquitination and proteolysis of short-lived regulators and misfolded proteins.

Here, we characterized the null phenotypes of UBR4-deficient mice in which the UBR box of *UBR4* was deleted. We show that the mutant mice die around embryonic days 9.5-10.5 (E9.5-E10.5) associated with abnormalities in various developmental processes such as neurogenesis and cardiovascular development. These developmental defects are significantly attributed to the inability to maintain cell integrity and adhesion, which significantly correlates to the severity of null phenotypes. UBR4-loss induces the depletion of many, but not all, proteins from the plasma membrane, suggesting that UBR4 is involved in proteome-wide turnover of cell surface proteins. Indeed, UBR4 is associated with and required to generate the MVBs which transiently store endocytosed cell surface proteins before their targeting to autophagosomes and subsequently lysosomes. Our results suggest that the N-recognin UBR4 plays a role in the homeostasis of cell surface proteins and, thus, cell adhesion and integrity.

As demonstrated in chapter 3.0, UBR4 is associated with early endosomes through its interaction with calmodulin and required for the turnover of cell surface. It is therefore reasonable to speculate that the homeostasis of cell surface proteins in UBR4-deficient cells are in part caused by misregulation in their endosome-mediated turnover. We provide evidence that UBR4-deficient cells fail to generate the MVBs in which endosome-cargo complexes are temporarily stored before degradation by lysosomes. Further mechanistic details explaining the correlation between early endosomes and cellular surface proteins are to be investigated.

6.4 THE FUNCTION OF N-TERMINAL ARGINYLATION BY ATE1 IN INNATE IMMUNITY

The N-end rule pathway has been implicated in Ub-dependent proteolysis of cytosolic short-lived proteins in various processes. We recently found that a set of ER-residing proteins, such as BiP, calreticulin, and PDI, are re-located to cytoplasm and Nt-arginylated under specific cellular stresses including cytoplasmic foreign DNA exposure and proteasomal inhibition [20]. The dsDNA-mediated immune response promotes the accumulation of R-BiP in the cytosol, which binds the selective autophagy receptor p62 through its binding of the ZZ domain of p62, resulting its self-oligomerization [20]. However, the physiological meanings of Nt-arginylation of BiP and the induced interaction of R-BiP with p62 in the innate immune system are poorly defined.

Cytoplasmic DNA derived from pathogens or host cells is recognized by the innate immune system through many DNA sensors, which activate STING-mediated innate immune respoonse. The activated STING in response to cytoplasmic DNA is translocated from the ER to the Golgi compartment, on which it recruits TANK-binding kinase 1 (TBK1) and the transcription factor IFN regulatory factor 3 (IRF3), leading to NF-κB and type I IFN gene expression [155, 156].

Here, we show that cytosolic foreign DNA, a strong inducer of innate immune response, facilitates Nt-arginylation of ER chaperons. ATE1-dependent Nt-arginylation is required for host defense system for IFN-β mediated gene induction and IRF3 phosphorylation. Cytosolic dsDNA induces relocation of ATE1 to the ER, on which ATE1 is colocalized with STING. ATE1 is essential for STING-mediated innate immune signaling because either transient deletion of ATE1 or its pharmaceutical inhibition impairs the trafficking of STING from the ER to the Golgi compartment. Nt-arginylation is essential for maintaining host defense system, thus its interference induces virion production. Our results suggest that Nt-arginylation is essential for sustain innate immunity against foreign DNA and viral infections.

We also observed that Nt-arginylation BiP that colocalized with aggregated STING on the Golgi compartment is eliminated by p62-mediated autophagy. During infection of host cells, the selective autophagy that eliminates invading pathogens and foreign particles is called as xenophagy [140]. The autophagic adapter p62 is an N-recognin that binds type-1 and type-2 N-terminal degrons (N-degrons), including arginine (Nt-Arg). We recently reported that our synthetic ZZ ligands targeting Zinc finger of p62 facilitated the self-oligomerization of p62 and induced autophagic biogenesis [11, 20]. Through these results, we can expect that ZZ ligands can activate p62 and induce selective autophagy for invading pathogens and cytoplasmic foreign DNA. Therefore we want to further investigate whether our ZZ ligands efficently induces the clearing of cytoplasmic dsDNA or pathogens via p62-mediated selective autophagy system later.

APPENDIX A

BIBLIOGRAPHY

1. Goldberg, A.L., Protein degradation and protection against misfolded or damaged proteins. Nature, 2003. **426**(6968): p. 895-9.

2. Puente, X.S., et al., Human and mouse proteases: a comparative genomic approach. Nat Rev Genet, 2003. **4**(7): p. 544-58.

3. Bachmair, A., D. Finley, and A. Varshavsky, In vivo half-life of a protein is a function of its amino-terminal residue. Science, 1986. **234**(4773): p. 179-86.

4. Tasaki, T., et al., The N-end rule pathway. Annu Rev Biochem, 2012. **81**: p. 261-89.

5. Kwon, Y.T., et al., The mouse and human genes encoding the recognition component of the N-end rule pathway. Proc Natl Acad Sci U S A, 1998. **95**(14): p. 7898-903.

6. Kwon, Y.T., et al., Female lethality and apoptosis of spermatocytes in mice lacking the UBR2 ubiquitin ligase of the N-end rule pathway. Mol Cell Biol, 2003. **23**(22): p. 8255-71.

7. Kwon, Y.T., et al., Construction and analysis of mouse strains lacking the ubiquitin ligase UBR1 (E3a) of the N-end rule pathway. Mol Cell Biol, 2001. **21**(23): p. 8007-21.

8. Tasaki, T., et al., A family of mammalian E3 ubiquitin ligases that contain the UBR box motif and recognize N-degrons. Mol Cell Biol, 2005. **25**(16): p. 7120-36.

9. Yoo, Y.D., et al., N-terminal arginylation generates a bimodal degron that modulates autophagic proteolysis. Proc Natl Acad Sci U S A, 2018. **115**(12): p. E2716-E2724.

10. Sriram, S.M., B.Y. Kim, and Y.T. Kwon, The N-end rule pathway: emerging functions and molecular principles of substrate recognition. Nat Rev Mol Cell Biol, 2011. **12**(11): p. 735-47.

11. Cha-Molstad, H., et al., Modulation of SQSTM1/p62 activity by N-terminal arginylation of the endoplasmic reticulum chaperone HSPA5/GRP78/BiP. Autophagy, 2016. **12**(2): p. 426-8.

12. Hu, R.G., et al., The N-end rule pathway as a nitric oxide sensor controlling the levels of multiple regulators. Nature, 2005. **437**(7061): p. 981-86.

13. Kwon, Y.T., et al., An essential role of N-terminal arginylation in cardiovascular development. Science, 2002. **297**(5578): p. 96-9.

14. Kwon, Y.T., A.S. Kashina, and A. Varshavsky, Alternative splicing results in differential expression, activity, and localization of the two forms of arginyl-tRNA-protein transferase, a component of the N-end rule pathway. Mol Cell Biol, 1999. **19**(1): p. 182-93.

15. Lee, M.J., et al., RGS4 and RGS5 are in vivo substrates of the N-end rule pathway. Proc Natl Acad Sci U S A, 2005. **102**(42): p. 15030-5.

16. Kwon, Y.T., et al., Altered activity, social behavior, and spatial memory in mice lacking the NTAN1p amidase and the asparagine branch of the N-end rule pathway. Mol Cell Biol, 2000. **20**(11): p. 4135-48.

17. Hwang, C.S., A. Shemorry, and A. Varshavsky, N-terminal acetylation of cellular proteins creates specific degradation signals. Science, 2010. **327**(5968): p. 973-77.

18. Kim, H.K., et al., The N-terminal methionine of cellular proteins as a degradation signal. Cell, 2014. **156**(1-2): p. 158-69.

19. Tasaki, T. and Y.T. Kwon, The mammalian N-end rule pathway: new insights into its components and physiological roles. Trends Biochem Sci, 2007. **32**(11): p. 520-8.

20. Cha-Molstad, H., et al., Amino-terminal arginylation targets endoplasmic reticulum chaperone BiP for autophagy through p62 binding. Nature Cell Biology, 2015. **17**(7): p. 917-929.

21. Ciechanover, A. and Y.T. Kwon, Protein Quality Control by Molecular Chaperones in Neurodegeneration. Front Neurosci, 2017. **11**: p. 185.

22. Deng, Z., et al., Autophagy Receptors and Neurodegenerative Diseases. Trends Cell Biol, 2017. **27**(7): p. 491-504.

23. Tasaki, T., et al., The substrate recognition domains of the N-end rule pathway. J Biol Chem, 2009. **284**(3): p. 1884-95.

24. Tasaki, T., et al., UBR box N-recognin-4 (UBR4), an N-recognin of the N-end rule pathway, and its role in yolk sac vascular development and autophagy. Proc Natl Acad Sci U S A, 2013. **110**(10): p. 3800-5.

25. Shim, S.Y., et al., Protein 600 is a microtubule/endoplasmic reticulum-associated protein in CNS neurons. Journal of Neuroscience, 2008. **28**(14): p. 3604-3614.

26. Kim, S.T., et al., The N-end rule proteolytic system in autophagy. Autophagy, 2013. **9**(7): p. 1100-3.

27. Wang, M., et al., PaxDb, a database of protein abundance averages across all three domains of life. Mol Cell Proteomics, 2012. **11**(8): p. 492-500.

28. Parsons, K., Y. Nakatani, and M.D. Nguyen, p600/UBR4 in the central nervous system. Cell Mol Life Sci, 2015. **72**(6): p. 1149-60.

29. Keerthikumar, S., et al., Proteogenomic analysis reveals exosomes are more oncogenic than ectosomes. Oncotarget, 2015. **6**(17): p. 15375-96.

30. Basso, M. and V. Bonetto, Extracellular Vesicles and a Novel Form of Communication in the Brain. Front Neurosci, 2016. **10**: p. 127.

31. Lin, R., et al., Acetylation stabilizes ATP-citrate lyase to promote lipid biosynthesis and tumor growth. Mol Cell, 2013. **51**(4): p. 506-518.

32. Wishart, T.M., et al., Combining comparative proteomics and molecular genetics uncovers regulators of synaptic and axonal stability and degeneration in vivo. PLoS Genet, 2012. **8**(8): p. e1002936.

33. Amorim, I.S., et al., Molecular neuropathology of the synapse in sheep with CLN5 Batten disease. Brain Behav, 2015. **5**(11): p. e00401.

34. Monies, D., et al., The landscape of genetic diseases in Saudi Arabia based on the first 1000 diagnostic panels and exomes. Hum Genet, 2017. **136**(8): p. 921-939.

35. Yau, R.G., et al., Assembly and Function of Heterotypic Ubiquitin Chains in Cell-Cycle and Protein Quality Control. Cell, 2017. **171**(4): p. 918-933 e20.

36. Tripathi, S., et al., Meta- and Orthogonal Integration of Influenza "OMICs" Data Defines a Role for UBR4 in Virus Budding. Cell Host Microbe, 2015. **18**(6): p. 723-35.

37. Morrison, J., et al., Dengue virus co-opts UBR4 to degrade STAT2 and antagonize type I interferon signaling. PLoS Pathog, 2013. **9**(3): p. e1003265.

38. Grant, A., et al., Zika Virus Targets Human STAT2 to Inhibit Type I Interferon Signaling. Cell Host Microbe, 2016. **19**(6): p. 882-90.

39. Huh, K.W., et al., Association of the human papillomavirus type 16 E7 oncoprotein with the 600-kDa retinoblastoma protein-associated factor, p600. Proc Natl Acad Sci U S A, 2005. **102**(32): p. 11492-7.

40. DeMasi, J., et al., Bovine papillomavirus E7 transformation function correlates with cellular p600 protein binding. Proc Natl Acad Sci U S A, 2005. **102**(32): p. 11486-91.

41. DeMasi, J., et al., Bovine papillomavirus E7 oncoprotein inhibits anoikis. J Virol, 2007. **81**(17): p. 9419-25.

42. White, E.A., et al., Systematic identification of interactions between host cell proteins and E7 oncoproteins from diverse human papillomaviruses. Proc Natl Acad Sci U S A, 2012. **109**(5): p. E260-7.

43. Szalmas, A., et al., The PTPN14 Tumor Suppressor Is a Degradation Target of Human Papillomavirus E7. J Virol, 2017. **91**(7).

44. White, E.A., K. Munger, and P.M. Howley, High-Risk Human Papillomavirus E7 Proteins Target PTPN14 for Degradation. MBio, 2016. **7**(5).

45. Rinschen, M.M., et al., The ubiquitin ligase Ubr4 controls stability of podocin/MEC-2 supercomplexes. Hum Mol Genet, 2016. **25**(7): p. 1328-44.

46. Hong, J.H., et al., KCMF1 (potassium channel modulatory factor 1) Links RAD6 to UBR4 (ubiquitin N-recognin domain-containing E3 ligase 4) and lysosome-mediated degradation. Mol Cell Proteomics, 2015. **14**(3): p. 674-85.

47. Sekelsky, J.J., et al., Identification of novel Drosophila meiotic genes recovered in a P-element screen. Genetics, 1999. **152**(2): p. 529-42.

48. Yager, R.R., Determining equivalent values for possibilistic variables. IEEE Trans Syst Man Cybern B Cybern, 2001. **31**(1): p. 19-31.

49. Ashton-Beaucage, D., et al., The Deubiquitinase USP47 Stabilizes MAPK by Counteracting the Function of the N-end Rule ligase POE/UBR4 in Drosophila. PLoS Biol, 2016. **14**(8): p. e1002539.

50. Nakatani, Y., et al., p600, a unique protein required for membrane morphogenesis and cell survival. Proc Natl Acad Sci U S A, 2005. **102**(42): p. 15093-8.

51. Gil, P., et al., BIG: a calossin-like protein required for polar auxin transport in Arabidopsis. Genes Dev, 2001. **15**(15): p. 1985-97.

52. Fuertes, G., et al., Changes in the proteolytic activities of proteasomes and lysosomes in human fibroblasts produced by serum withdrawal, amino-acid deprivation and confluent conditions. Biochem J, 2003. **375**(Pt 1): p. 75-86.

53. Burman, C. and N.T. Ktistakis, Autophagosome formation in mammalian cells. Semin Immunopathol, 2010. **32**(4): p. 397-413.

54. Tanida, I., Autophagosome formation and molecular mechanism of autophagy. Antioxid Redox Signal, 2011. **14**(11): p. 2201-14.

55. Freeman, S.J. and J.B. Lloyd, Evidence that protein ingested by the rat visceral yolk sac yields amino acids for synthesis of embryonic protein. J Embryol Exp Morphol, 1983. **73**: p. 307-15.

56. New, D.A., Whole-embryo culture and the study of mammalian embryos during organogenesis. Biol Rev Camb Philos Soc, 1978. **53**(1): p. 81-122.

57. Fader, C.M. and M.I. Colombo, Autophagy and multivesicular bodies: two closely related partners. Cell Death Differ, 2009. **16**(1): p. 70-8.

58. Mombaerts, P., et al., Visualizing an olfactory sensory map. Cell, 1996. **87**(4): p. 675-86.

59. Bunting, M., et al., Targeting genes for self-excision in the germ line. Genes Dev, 1999. **13**(12): p. 1524-8.

60. Liu, P., N.A. Jenkins, and N.G. Copeland, A highly efficient recombineering-based method for generating conditional knockout mutations. Genome Res, 2003. **13**(3): p. 476-84.

61. Warming, S., et al., Simple and highly efficient BAC recombineering using galK selection. Nucleic Acids Res, 2005. **33**(4): p. e36.

62. Shim, S.Y., et al., Protein 600 is a microtubule/endoplasmic reticulum-associated protein in CNS neurons. J Neurosci, 2008. **28**(14): p. 3604-14.

63. Jacomin, A.C., et al., iLIR database: A web resource for LIR motif-containing proteins in eukaryotes. Autophagy, 2016. **12**(10): p. 1945-1953.

64. Ciechanover, A. and Y.T. Kwon, Degradation of misfolded proteins in neurodegenerative diseases: therapeutic targets and strategies. Exp Mol Med, 2015. **47**(3): p. e147.

65. Ji, C.H. and Y.T. Kwon, Crosstalk and Interplay between the Ubiquitin-Proteasome System and Autophagy. Mol Cells, 2017. **40**(7): p. 441-449.

66. Braten, O., et al., Numerous proteins with unique characteristics are degraded by the 26S proteasome following monoubiquitination. Proc Natl Acad Sci U S A, 2016. **113**(32): p. E4639-47.

67. Mizushima, N. and M. Komatsu, Autophagy: renovation of cells and tissues. Cell, 2011. **147**(4): p. 728-41.

68. Authier, F., et al., Proteolysis of glucagon within hepatic endosomes by membrane-associated cathepsins B and D. J Biol Chem, 1995. **270**(26): p. 15798-807.

69. Blum, J.S., M.L. Fiani, and P.D. Stahl, Proteolytic cleavage of ricin A chain in endosomal vesicles. Evidence for the action of endosomal proteases at both neutral and acidic pH. J Biol Chem, 1991. **266**(33): p. 22091-5.

70. Tjelle, T.E., et al., Isolation and characterization of early endosomes, late endosomes and terminal lysosomes: their role in protein degradation. J Cell Sci, 1996. **109 (Pt 12)**: p. 2905-14.

71. Pillay, C.S., E. Elliott, and C. Dennison, Endolysosomal proteolysis and its regulation. Biochem J, 2002. **363**(Pt 3): p. 417-29.

72. Huotari, J. and A. Helenius, Endosome maturation. EMBO J, 2011. **30**(17): p. 3481-500.

73. Steinman, R.M., et al., Endocytosis and the recycling of plasma membrane. J Cell Biol, 1983. **96**(1): p. 1-27.

74. Maxfield, F.R., Role of endosomes and lysosomes in human disease. Cold Spring Harb Perspect Biol, 2014. **6**(5): p. a016931.

75. Berg, T., T. Gjoen, and O. Bakke, Physiological functions of endosomal proteolysis. Biochem J, 1995. **307 (Pt 2)**: p. 313-26.

76. Authier, F., B.I. Posner, and J.J. Bergeron, Endosomal proteolysis of internalized proteins. FEBS Lett, 1996. **389**(1): p. 55-60.

77. Ciechanover, A., et al., Kinetics of internalization and recycling of transferrin and the transferrin receptor in a human hepatoma cell line. Effect of lysosomotropic agents. J Biol Chem, 1983. **258**(16): p. 9681-9.

78. Ciechanover, A., A.L. Schwartz, and H.F. Lodish, The asialoglycoprotein receptor internalizes and recycles independently of the transferrin and insulin receptors. Cell, 1983. **32**(1): p. 267-75.

79. Conner, S.D. and S.L. Schmid, Regulated portals of entry into the cell. Nature, 2003. **422**(6927): p. 37-44.

80. Cabrera, M., et al., Functional separation of endosomal fusion factors and the class C core vacuole/endosome tethering (CORVET) complex in endosome biogenesis. J Biol Chem, 2013. **288**(7): p. 5166-75.

81. Abrahamson, D.R. and R. Rodewald, Evidence for the sorting of endocytic vesicle contents during the receptor-mediated transport of IgG across the newborn rat intestine. J Cell Biol, 1981. **91**(1): p. 270-80.

82. Besterman, J.M. and R.B. Low, Endocytosis: a review of mechanisms and plasma membrane dynamics. Biochem J, 1983. **210**(1): p. 1-13.

83. Appelqvist, H., et al., The lysosome: from waste bag to potential therapeutic target. J Mol Cell Biol, 2013. **5**(4): p. 214-26.

84. Casey, J.R., S. Grinstein, and J. Orlowski, Sensors and regulators of intracellular pH. Nat Rev Mol Cell Biol, 2010. **11**(1): p. 50-61.

85. Jaworska, A., et al., SERS-based monitoring of the intracellular pH in endothelial cells: the influence of the extracellular environment and tumour necrosis factor-alpha. Analyst, 2015. **140**(7): p. 2321-9.

86. Goh, L.K. and A. Sorkin, Endocytosis of receptor tyrosine kinases. Cold Spring Harb Perspect Biol, 2013. **5**(5): p. a017459.

87. Dasgupta, S., et al., Proteasome inhibitors alter levels of intracellular peptides in HEK293T and SH-SY5Y cells. PLoS One, 2014. **9**(7): p. e103604.

88. Repnik, U., M.H. Cesen, and B. Turk, The endolysosomal system in cell death and survival. Cold Spring Harb Perspect Biol, 2013. **5**(1): p. a008755.

89. Berg, T.O., et al., Isolation and characterization of rat liver amphisomes. Evidence for fusion of autophagosomes with both early and late endosomes. J Biol Chem, 1998. **273**(34): p. 21883-92.

90. Fengsrud, M., et al., Ultrastructural characterization of the delimiting membranes of isolated autophagosomes and amphisomes by freeze-fracture electron microscopy. Eur J Cell Biol, 2000. **79**(12): p. 871-82.

91. Simonsen, A., et al., EEA1 links PI(3)K function to Rab5 regulation of endosome fusion. Nature, 1998. **394**(6692): p. 494-8.

92. Simonsen, A., et al., The Rab5 effector EEA1 interacts directly with syntaxin-6. J Biol Chem, 1999. **274**(41): p. 28857-60.

93. Colombo, M.I., W. Beron, and P.D. Stahl, Calmodulin regulates endosome fusion. J Biol Chem, 1997. **272**(12): p. 7707-12.

94. Lawe, D.C., et al., Essential role of Ca2+/calmodulin in Early Endosome Antigen-1 localization. Mol Biol Cell, 2003. **14**(7): p. 2935-45.

95. Zerial, M.a.M.H., Rab proteins as membrane organizers. Nature Reviews Molecular Cell Biology, 2001. **2**(2): p. 107--117.

96. Poteryaev, D., et al., Identification of the switch in early-to-late endosome transition. Cell, 2010. **141**(3): p. 497-508.

97. Kwon, Y.T., F. Levy, and A. Varshavsky, Bivalent inhibitor of the N-end rule pathway. J Biol Chem, 1999. **274**(25): p. 18135-9.

98. Lee, M.J., et al., Synthetic heterovalent inhibitors targeting recognition E3 components of the N-end rule pathway. Proc Natl Acad Sci U S A, 2008. **105**(1): p. 100-5.

99. Sriram, S.M. and Y.T. Kwon, The molecular principles of N-end rule recognition. Nat Struct Mol Biol, 2010. **17**(10): p. 1164-5.

100. Cha-Molstad, H., et al., p62/SQSTM1/Sequestosome-1 is an N-recognin of the N-end rule pathway which modulates autophagosome biogenesis. Nat Commun, 2017. **8**(1): p. 102.

101. Kwon, Y.T., et al., Construction and analysis of mouse strains lacking the ubiquitin ligase UBR1 (E3α) of the N-end rule pathway. Molecular and Cellular Biology, 2001. **21**(23): p. 8007--8021.

102. Nakaya, T., et al., p600 Plays Essential Roles in Fetal Development. PLoS One, 2013. **8**(6): p. e66269.

103. Schindelin, J., et al., Fiji: an open-source platform for biological-image analysis. Nat Methods, 2012. **9**(7): p. 676-82.

104. Vives, E., P. Brodin, and B. Lebleu, A truncated HIV-1 Tat protein basic domain rapidly translocates through the plasma membrane and accumulates in the cell nucleus. J Biol Chem, 1997. **272**(25): p. 16010-7.

105. Li, G., et al., Evidence for phosphatidylinositol 3-kinase as a regulator of endocytosis via activation of Rab5. Proc Natl Acad Sci U S A, 1995. **92**(22): p. 10207-11.

106. Li, G. and P.D. Stahl, Structure-function relationship of the small GTPase rab5. J Biol Chem, 1993. **268**(32): p. 24475-80.

107. Stoorvogel, W., Analysis of the endocytic system by using horseradish peroxidase. Trends Cell Biol, 1998. **8**(12): p. 503-5.

108. Mesaki, K., et al., Fission of tubular endosomes triggers endosomal acidification and movement. PLoS One, 2011. **6**(5): p. e19764.

109. Kawamura, N., et al., Delivery of endosomes to lysosomes via microautophagy in the visceral endoderm of mouse embryos. Nat Commun, 2012. **3**: p. 1071.

110. Zohn, I.E. and A.A. Sarkar, The visceral yolk sac endoderm provides for absorption of nutrients to the embryo during neurulation. Birth Defects Res A Clin Mol Teratol, 2010. **88**(8): p. 593-600.

111. Yezid, H., et al., Mechanism for HIV-1 Tat insertion into the endosome membrane. J Biol Chem, 2009. **284**(34): p. 22736-46.

112. Lonn, P., et al., Enhancing Endosomal Escape for Intracellular Delivery of Macromolecular Biologic Therapeutics. Sci Rep, 2016. **6**: p. 32301.

113. Jovic, M., et al., The early endosome: a busy sorting station for proteins at the crossroads. Histol Histopathol, 2010. **25**(1): p. 99-112.

114. Rink, J., et al., Rab conversion as a mechanism of progression from early to late endosomes. Cell, 2005. **122**(5): p. 735-749.

115. Lawe, D.C., et al., The FYVE domain of early endosome antigen 1 is required for both phosphatidylinositol 3-phosphate and Rab5 binding - Critical role of this dual interaction for endosomal localization. Journal of Biological Chemistry, 2000. **275**(5): p. 3699-3705.

116. Dumas, J.J., et al., Multivalent endosome targeting by homodimeric EEA1. Mol Cell, 2001. **8**(5): p. 947-58.

117. Marwaha, R., et al., The Rab7 effector PLEKHM1 binds Arl8b to promote cargo traffic to lysosomes. J Cell Biol, 2017. **216**(4): p. 1051-1070.

118. Law, V., et al., DrugBank 4.0: shedding new light on drug metabolism. Nucleic Acids Res, 2014. **42**(Database issue): p. D1091-7.

119. Eisele, F. and D.H. Wolf, Degradation of misfolded protein in the cytoplasm is mediated by the ubiquitin ligase Ubr1. FEBS Lett, 2008. **582**(30): p. 4143-6.

120. Bian, S., Cell Adhesion Molecules in Neural Stem Cell and Stem Cell-Based Therapy for Neural Disorders, in Neural Stem Cells, L. Bonfanti, Editor. 2013, IntechOpen.

121. Takeichi, M., The cadherin superfamily in neuronal connections and interactions. Nat Rev Neurosci, 2007. **8**(1): p. 11-20.

122. Navarro, P., L. Ruco, and E. Dejana, Differential localization of VE- and N-cadherins in human endothelial cells: VE-cadherin competes with N-cadherin for junctional localization. J Cell Biol, 1998. **140**(6): p. 1475-84.

123. Radice, G.L., et al., Developmental defects in mouse embryos lacking N-cadherin. Dev Biol, 1997. **181**(1): p. 64-78.

124. Scheurer, S.B., et al., Identification and relative quantification of membrane proteins by surface biotinylation and two-dimensional peptide mapping. Proteomics, 2005. **5**(11): p. 2718-28.

125. Kischel, P., et al., Cell membrane proteomic analysis identifies proteins differentially expressed in osteotropic human breast cancer cells. Neoplasia, 2008. **10**(9): p. 1014-20.

126. Rybak, J.-N., et al., Purification of biotinylated proteins on streptavidin resin: A protocol for quantitative elution. Proteomics, 2004. **4**(8): p. 2296-2299.

127. Rosenfeld, J., et al., In-gel digestion of proteins for internal sequence analysis after one-or two-dimensional gel electrophoresis. Analytical biochemistry, 1992. **203**(1): p. 173-179.

128. Keller, A., et al., Empirical statistical model to estimate the accuracy of peptide identifications made by MS/MS and database search. Analytical chemistry, 2002. **74**(20): p. 5383-5392.

129. Nesvizhskii, A.I., et al., A statistical model for identifying proteins by tandem mass spectrometry. Analytical chemistry, 2003. **75**(17): p. 4646-4658.

130. Pavelka, N., et al., Statistical similarities between transcriptomics and quantitative shotgun proteomics data. Molecular & Cellular Proteomics, 2008. **7**(4): p. 631-644.

131. Lescroart, F., et al., Clonal analysis reveals common lineage relationships between head muscles and second heart field derivatives in the mouse embryo. Development, 2010. **137**(19): p. 3269-3279.

132. Paik, J.H., et al., Sphingosine 1-phosphate receptor regulation of N-cadherin mediates vascular stabilization. Genes Dev, 2004. **18**(19): p. 2392-403.

133. Luo, Y. and G.L. Radice, N-cadherin acts upstream of VE-cadherin in controlling vascular morphogenesis. J Cell Biol, 2005. **169**(1): p. 29-34.

134. Zaret, K.S., Regulatory phases of early liver development: paradigms of organogenesis. Nat Rev Genet, 2002. **3**(7): p. 499-512.

135. Ivaska, J. and J. Heino, Interplay between cell adhesion and growth factor receptors: from the plasma membrane to the endosomes. Cell Tissue Res, 2010. **339**(1): p. 111-20.

136. Grossier, J.P., et al., Cell adhesion defines the topology of endocytosis and signaling. EMBO J, 2014. **33**(1): p. 35-45.

137. Zemskov, E.A., et al., Regulation of platelet-derived growth factor receptor function by integrin-associated cell surface transglutaminase. J Biol Chem, 2009. **284**(24): p. 16693-703.

138. Enriquez-Barreto, L., et al., Neural cell adhesion molecule, NCAM, regulates thalamocortical axon pathfinding and the organization of the cortical somatosensory representation in mouse. Front Mol Neurosci, 2012. **5**: p. 76.

139. Takeichi, M., et al., Cadherin-mediated cell-cell adhesion and neurogenesis. Neurosci Res Suppl, 1990. **13**: p. S92-6.

140. Mao, K. and D.J. Klionsky, Xenophagy: A battlefield between host and microbe, and a possible avenue for cancer treatment. Autophagy, 2017. **13**(2): p. 223-224.

141. Grumati, P. and I. Dikic, Ubiquitin signaling and autophagy. J Biol Chem, 2018. **293**(15): p. 5404-5413.

142. Zheng, Y.T., et al., The adaptor protein p62/SQSTM1 targets invading bacteria to the autophagy pathway. J Immunol, 2009. **183**(9): p. 5909-16.

143. Barrat, F.J., K.B. Elkon, and K.A. Fitzgerald, Importance of Nucleic Acid Recognition in Inflammation and Autoimmunity. Annu Rev Med, 2016. **67**: p. 323-36.

144. Hornung, V., et al., AIM2 recognizes cytosolic dsDNA and forms a caspase-1-activating inflammasome with ASC. Nature, 2009. **458**(7237): p. 514-8.

145. Takaoka, A., et al., DAI (DLM-1/ZBP1) is a cytosolic DNA sensor and an activator of innate immune response. Nature, 2007. **448**(7152): p. 501-5.

146. Zhang, Z., et al., The helicase DDX41 senses intracellular DNA mediated by the adaptor STING in dendritic cells. Nat Immunol, 2011. **12**(10): p. 959-65.

147. Unterholzner, L., et al., IFI16 is an innate immune sensor for intracellular DNA. Nature Immunology, 2010. **11**(11): p. 997-U42.

148. Yang, P., et al., The cytosolic nucleic acid sensor LRRFIP1 mediates the production of type I interferon via a beta-catenin-dependent pathway. Nat Immunol, 2010. **11**(6): p. 487-94.

149. Ablasser, A., et al., RIG-I-dependent sensing of poly(dA:dT) through the induction of an RNA polymerase III-transcribed RNA intermediate. Nat Immunol, 2009. **10**(10): p. 1065-72.

150. Chiu, Y.H., J.B. Macmillan, and Z.J. Chen, RNA polymerase III detects cytosolic DNA and induces type I interferons through the RIG-I pathway. Cell, 2009. **138**(3): p. 576-91.

151. Sun, L., et al., Cyclic GMP-AMP synthase is a cytosolic DNA sensor that activates the type I interferon pathway. Science, 2013. **339**(6121): p. 786-91.

152. Ishikawa, H. and G.N. Barber, STING is an endoplasmic reticulum adaptor that facilitates innate immune signalling. Nature, 2008. **455**(7213): p. 674-8.

153. Zhong, B., et al., The adaptor protein MITA links virus-sensing receptors to IRF3 transcription factor activation. Immunity, 2008. **29**(4): p. 538-50.

154. Abe, T., et al., STING recognition of cytoplasmic DNA instigates cellular defense. Mol Cell, 2013. **50**(1): p. 5-15.

155. Burdette, D.L. and R.E. Vance, STING and the innate immune response to nucleic acids in the cytosol. Nat Immunol, 2013. **14**(1): p. 19-26.

156. Hiller, B. and V. Hornung, STING Signaling the enERGIC Way. Cell Host Microbe, 2015. **18**(2): p. 137-9.

157. Pomerantz, J.L., E.M. Denny, and D. Baltimore, CARD11 mediates factor-specific activation of NF-kappaB by the T cell receptor complex. EMBO J, 2002. **21**(19): p. 5184-94.

158. Kim, Y.E. and J.H. Ahn, Positive role of promyelocytic leukemia protein in type I interferon response and its regulation by human cytomegalovirus. PLoS Pathog, 2015. **11**(3): p. e1004785.

159. Lee, H.R., et al., Ability of the human cytomegalovirus IE1 protein to modulate sumoylation of PML correlates with its functional activities in transcriptional regulation and infectivity in cultured fibroblast cells. J Virol, 2004. **78**(12): p. 6527-42.

160. Pawaria, S., et al., Taking the STING out of TLR-driven autoimmune diseases: good, bad, or indifferent? J Leukoc Biol, 2017. **101**(1): p. 121-126.

161. McCaffary, D., STING signalling: an emerging common pathway in autoimmunity and cancer. Immunopharmacol Immunotoxicol, 2017. **39**(5): p. 253-258.